

**Development of Frequency Domain Multidimensional Spectroscopy  
with Applications in Semiconductor Photophysics**

By  
Blaise Jonathan Thompson

A dissertation submitted in partial fulfillment of  
the requirements for the degree of

Doctor of Philosophy  
(Chemistry)

at the  
UNIVERSITY OF WISCONSIN - MADISON  
2018

Date of final oral examination: April 23, 2018

This dissertation is approved by the following members of the Final Oral Committee:

John C. Wright, Professor, Analytical Chemistry  
Randall Goldsmith, Professor, Analytical Chemistry  
Tim Bertram, Professor, Analytical Chemistry  
Kyoung-Shin Choi, Professor, Materials Chemistry



# Contents

<b>List of Figures</b>	<b>v</b>
<b>List of Tables</b>	<b>vii</b>
<b>Acknowledgments</b>	<b>ix</b>
<b>Abstract</b>	<b>1</b>
<b>1 Introduction</b>	<b>3</b>
1.1 Coherent Multidimensional Spectroscopy . . . . .	3
1.2 The CMDS Instrument . . . . .	3
1.3 Scientific Software . . . . .	4
<b>I Background</b>	<b>5</b>
<b>2 Spectroscopy</b>	<b>7</b>
2.1 Light . . . . .	8
2.2 Light-Matter Interaction . . . . .	8
2.2.1 Representations . . . . .	8
2.3 Linear Spectroscopy . . . . .	9
2.3.1 Reflectivity . . . . .	9
2.4 Coherent Multidimensional Spectroscopy . . . . .	9
2.4.1 Three Wave . . . . .	10
2.4.2 Four Wave . . . . .	10
2.4.3 Five Wave . . . . .	10
2.4.4 Six Wave . . . . .	10
2.5 Strategies for CMDS . . . . .	10
2.5.1 Homodyne vs. Heterodyne Detection . . . . .	10
2.5.2 Frequency vs. Time Domain . . . . .	10
2.5.3 Triply Electronically Enhanced Spectroscopy . . . . .	11
2.5.4 Transient Absorbance Spectroscopy . . . . .	11
2.5.5 Cross Polarized TrEE . . . . .	15
2.5.6 Pump-TrEE-Probe . . . . .	15
2.6 Instrumental Response Function . . . . .	15

2.6.1	Time Domain . . . . .	15
2.6.2	Frequency Domain . . . . .	16
2.6.3	Time-Bandwidth Product . . . . .	17
<b>3</b>	<b>Materials</b>	<b>19</b>
<b>4</b>	<b>Software</b>	<b>21</b>
<b>II</b>	<b>Development</b>	<b>23</b>
<b>5</b>	<b>Processing</b>	<b>25</b>
5.1	Data object model . . . . .	25
5.2	Artists . . . . .	27
5.3	Fitting . . . . .	27
5.4	Distribution and licensing . . . . .	27
5.5	Future directions . . . . .	27
<b>6</b>	<b>Acquisition</b>	<b>29</b>
6.1	Overview . . . . .	30
6.2	Future directions . . . . .	30
6.2.1	Ideal Axis Positions . . . . .	30
6.2.2	Exponential . . . . .	32
<b>7</b>	<b>Active Correction in MR-CMDS</b>	<b>37</b>
7.1	Hardware . . . . .	37
7.1.1	Delay Stages . . . . .	37
7.2	Signal Acquisition . . . . .	37
7.2.1	Digital Signal Processing . . . . .	37
7.3	Artifacts and Noise . . . . .	37
7.3.1	Scatter . . . . .	37
7.3.2	Normalization of dual-chopped self-heterodyned signal . . . . .	46
7.4	Light Generation . . . . .	47
7.4.1	Automated OPA Tuning . . . . .	47
7.5	Optomechanics . . . . .	47
7.5.1	Automated Neutral Density Wheels . . . . .	47
<b>8</b>	<b>A robust, fully automated algorithm to collect high quality OPA tuning curves</b>	<b>49</b>
<b>9</b>	<b>Disentangling material and instrument response</b>	<b>51</b>
9.1	Introduction . . . . .	52
9.2	Theory . . . . .	55
9.2.1	Inhomogeneity . . . . .	62
9.3	Methods . . . . .	62
9.3.1	Characteristics of Driven and Impulsive Response . . . . .	62
9.3.2	Convolution Technique for Inhomogeneous Broadening . . . . .	65

9.4	Results . . . . .	68
9.4.1	Evolution of single coherence . . . . .	69
9.4.2	Evolution of single Liouville pathway . . . . .	74
9.4.3	Temporal pathway discrimination . . . . .	79
9.4.4	Multidimensional line shape dependence on pulse delay time . . . . .	82
9.4.5	Inhomogeneous broadening . . . . .	87
9.5	Discussion . . . . .	92
9.5.1	An intuitive picture of pulse effects . . . . .	92
9.5.2	Conditional validity of the driven limit . . . . .	93
9.5.3	Extracting true material correlation . . . . .	96
9.6	Conclusion . . . . .	99
<b>III Applications</b>		<b>101</b>
<b>10 PbSe</b>		<b>103</b>
<b>11 Transition metal dichalcogenide thin films</b>		<b>105</b>
11.1	Introduction . . . . .	106
11.2	Methods . . . . .	109
11.3	Results and discussion . . . . .	117
11.4	Conclusions . . . . .	131
<b>12 PEDOT:PSS</b>		<b>133</b>
12.1	Introduction . . . . .	133
12.2	Background . . . . .	133
12.3	Methods . . . . .	134
12.4	Transmittance and reflectance . . . . .	135
12.5	Three-pulse echo spectroscopy . . . . .	137
12.5.1	Assignment of zero delay . . . . .	141
12.6	Frequency-domain transient grating spectroscopy . . . . .	152
<b>13 Pyrite</b>		<b>153</b>
<b>14 BiVO<sub>4</sub></b>		<b>155</b>
<b>IV Appendix</b>		<b>157</b>
<b>A Public</b>		<b>159</b>
A.1	Chemical systems . . . . .	159
A.1.1	Concentration . . . . .	160
A.1.2	Timescale . . . . .	160
A.1.3	Lengthscale . . . . .	160
A.2	Analytical chemistry . . . . .	160

A.3	Spectroscopy . . . . .	160
A.3.1	Nonlinear spectroscopy . . . . .	161
A.4	Instrumentation . . . . .	161
A.4.1	LASER . . . . .	161
A.4.2	OPA . . . . .	162
<b>B</b>	<b>Procedures</b>	<b>163</b>
B.1	“Six-month” maintenance . . . . .	164
B.2	Lytron Kodiak RC006 . . . . .	166
B.3	PolyScience 6000 Series . . . . .	167
B.4	NesLab Merlin M33 . . . . .	168
B.5	Calibrating the 407A . . . . .	169
B.6	Millenia . . . . .	170
B.6.1	Startup . . . . .	170
B.6.2	Toggling service mode . . . . .	170
B.7	Spitfire Pro . . . . .	171
B.7.1	Startup . . . . .	171
B.7.2	Common alignment . . . . .	171
B.7.3	Stretcher alignment . . . . .	174
B.7.4	Compressor alignment . . . . .	174
B.8	TOPAS-C . . . . .	175
B.8.1	Common alignment . . . . .	175
B.8.2	Full alignment . . . . .	176
B.9	MicroHR Monochromator . . . . .	180
<b>C</b>	<b>Hardware</b>	<b>181</b>
C.1	Adjustable periscopes . . . . .	181
C.1.1	Wedge polarization preference . . . . .	183
C.2	Automated transmissive filters . . . . .	183
C.3	Electronics . . . . .	184
<b>D</b>	<b>Errata</b>	<b>185</b>
D.1	Czech 2015 . . . . .	185
<b>E</b>	<b>Colophon</b>	<b>187</b>

# List of Figures

2.1	CAPTION TODO . . . . .	12
6.1	TODO . . . . .	34
7.1	Simulated interference patterns in old delay parameterization. . . . .	39
7.2	Simulated interference patterns in current delay parameterization. . . . .	41
7.3	Comparison of single, dual chopping. . . . .	45
9.1	Sixteen triply-resonant Liouville pathways. . . . .	56
9.2	Overview of the MR-CMDS simulation. . . . .	59
9.3	Convolution overview. . . . .	66
9.4	Relative importance of FID and driven response for a single quantum coherence. . . . .	70
9.5	Pulsed excitation of a single quantum coherence and its dependance on pulse detuning. . . . .	72
9.6	2D frequency response of a single Liouville pathway at different delay values. . . . .	75
9.7	2D delay response for different relative dephasing rates. . . . .	80
9.8	Evolution of the 2D frequency response. . . . .	83
9.9	Wigners. . . . .	86
9.10	2D delay response with inhomogeneity. . . . .	88
9.11	Spectral evolution of an inhomogenous system. . . . .	91
9.12	Conditional validity of the driven limit. . . . .	95
9.13	Metrics of correlation. . . . .	97

11.1	CMD5 tutorial . . . . .	108
11.2	Schematic of the synthetic setup used for Mo thin film sulfidation reactions. . . . .	110
11.3	Mask and epi vs transmissive. . . . .	112
11.4	OPA outputs at each color explored. . . . .	113
11.5	Spectral delay correction. . . . .	115
11.6	MoS <sub>2</sub> post processing. . . . .	116
11.7	Few-layer MoS <sub>2</sub> thin film characterization. . . . .	118
11.8	MoS <sub>2</sub> absorbance. . . . .	119
11.9	MoS <sub>2</sub> frequency-frequency slices. . . . .	121
11.10	MoS <sub>2</sub> $\omega_1$ Wigner progression. . . . .	122
11.11	MoS <sub>2</sub> $\omega_2$ Wigner progression. . . . .	123
11.12	Pathway V, VI liouville pathways. . . . .	125
11.13	MoS <sub>2</sub> transients. . . . .	128
11.14	MoS <sub>2</sub> frequency-frequency slices near pulse overlap. . . . .	129
11.15	Pathways I, III Liouville pathways. . . . .	130
12.1	PEDOT:PSS transmission and reflectance spectra. . . . .	136
12.2	PEDOT:PSS 3PE phase matching mask. . . . .	138
12.3	PEDOT:PSS 3PE raw data. . . . .	140
12.4	PEDOT:PSS 3PE delay space. . . . .	142
12.5	PEDOT:PSS 3PE processed data. . . . .	143
12.6	PEDOT:PSS 3PE traces. . . . .	144
12.7	PEDOT:PSS 3PE traces. . . . .	145
12.8	PEDOT:PSS 3PE traces. . . . .	148
12.9	PEDOT:PSS 3PE traces. . . . .	151
C.1	CAPTION TODO . . . . .	182



# List of Tables

7.1	Shot-types in phase shifted parallel modulation. . . . .	43
9.1	Conditions for peak intensity at different pulse delays for pathway $I\gamma$ . . . . .	77
12.1	. . . . .	150



# Acknowledgments

To John...

To my colleagues...

To Tyler....

To Claire...

To Sam...

To my parents...

Finally, thank you to all humans who have and continue to undertake the ongoing free and responsible search for truth and meaning. Thanks to free software / free culture / open science advocates who have worked to create and share foundational tools and ideas, often at great personal opportunity cost. Thanks to thought leaders who have shown me what it means to have a good life without fully abandoning moral principles. And thank you to those who bravely speak truth to power. This universe is stranger, more terrible, and more fantastic than we want to believe. We must find ways to describe it's complexity without falling victim to the sometimes-overwhelming power of simple, "useful" narratives.

*The explanatory stories that people find compelling are simple; are concrete rather than abstract; assign a larger role to talent, stupidity and intentions than to luck; and focus on a few striking events that happened rather than on the countless events that failed to happen.*

*The ultimate test of an explanation is whether it would have made the event predictable in advance.*

*Paradoxically, it is easier to construct a coherent story when you know little, when there are fewer pieces to fit into the puzzle. Our comforting conviction that the world makes sense rests on a secure foundation: our almost unlimited ability to ignore our ignorance.*

– Daniel Kahneman [1]



# Abstract



# Chapter 1

## Introduction

### 1.1 Coherent Multidimensional Spectroscopy

CMDS, coherent multidimensional spectroscopy

### 1.2 The CMDS Instrument

From an instrumental perspective, MR-CMDS is a problem of calibration and coordination. Within the Wright Group, each of our two main instruments are composed of roughly ten actively moving component hardwares. Many of these components are purchased directly from vendors such as SpectraPhysics, National Instruments, Horiba, Thorlabs, and Newport. Others are created or heavily modified by graduate students. The Wright Group has always maintained custom acquisition software packages which control the complex, many-stepped dance that these components must perform to acquire MR-CMDS spectra.

## 1.3 Scientific Software

When I joined the Wright Group, I saw that acquisition software was a real barrier to experimental progress and flexibility. Graduate students had ideas for instrumental enhancements that were infeasible because of the challenge of incorporating the new components into the existing software ecosystem. At the same time, students were spending much of their time in lab repeatedly calibrating optical parametric amplifiers by hand, a process that sometimes took days. I chose to spend a significant portion of my graduate career focusing on solving these problems through software development. At first, I focused on improving the existing LabVIEW code. Eventually, I developed a vision for a deeply modular acquisition software that could not be practically created with LabVIEW. Using Python and Qt, I created a brand new acquisition software PyCMDS: built from the ground up to fundamentally solve historical challenges in the Group. PyCMDS offers a modular hardware model that can “re-configure” itself to flexibly control a variety of component hardware configurations. This has enabled graduate students to add and remove hardware whenever necessary, without worrying about a heavy additional programming burden. PyCMDS is now used to drive both MR-CMDS instruments in the Group, allowing for easy sharing of component hardware and lessening the total amount of software that the Group needs to maintain. Besides being more flexible, PyCMDS solves a number of other problems. It offers fully automated strategies for calibrating component hardware, making calibration less arduous and more reproducible. It offers more fine-grained control of data acquisition and timing, enabling more complex algorithms to quickly acquire artifact-free results. In conjunction with other algorithmic and hardware improvements that I have made, PyCMDS has decreased acquisition times by up to two orders of magnitude. A companion software, WrightTools (which I also created), solves some of the processing and representation challenges of multidimensional data.



## **Part I**

# **Background**



## Chapter 2

# Spectroscopy

*A hundred years ago, Auguste Comte, . . . a great philosopher, said that humans will never be able to visit the stars, that we will never know what stars are made out of, that that's the one thing that science will never ever understand, because they're so far away. And then, just a few years later, scientists took starlight, ran it through a prism, looked at the rainbow coming from the starlight, and said: "Hydrogen!" Just a few years after this very rational, very reasonable, very scientific prediction was made, that we'll never know what stars are made of.*

– Michio Kaku

In this chapter I lay out the foundations of spectroscopy.

## 2.1 Light

## 2.2 Light-Matter Interaction

Spectroscopic experiments all derive from the interaction of light and matter. Many material properties can be deduced by measuring the nature of this interaction.

Nonlinear spectroscopy relies upon higher-order terms in the light-matter interaction. In a generic system, each term is roughly ten times smaller than the last.

### 2.2.1 Representations

Many strategies have been introduced for diagrammatically representing the interaction of multiple electric fields in an experiment.

#### Circle Diagrams

#### Double-sided Feynman Diagrams

#### WMEL Diagrams

So-called wave mixing energy level (WMEL) diagrams are the most familiar way of representing spectroscopy for Wright group members. WMEL diagrams were first proposed by Lee and Albrecht in an appendix to their seminal work *A Unified View of Raman, Resonance Raman, and Fluorescence Spectroscopy* [LeeDuckhwan1985a]. WMEL diagrams are drawn using the following rules.

1. The energy ladder is represented with horizontal lines - solid for real states and dashed for virtual states.

2. Individual electric field interactions are represented as vertical arrows. The arrows span the distance between the initial and final state in the energy ladder.
3. The time ordering of the interactions is represented by the ordering of arrows, from left to right.
4. Ket-side interactions are represented with solid arrows.
5. Bra-side interactions are represented with dashed arrows.
6. Output is represented as a solid wavy line.

## Mukamel Diagrams

## 2.3 Linear Spectroscopy

### 2.3.1 Reflectivity

This derivation adapted from *Optical Processes in Semiconductors* by Jacques I. Pankove [**PankoveJacques1975a**].

For normal incidence, the reflection coefficient is

$$R = \frac{(n - 1)^2 + k^2}{(n + 1)^2 + k^2} \quad (2.1)$$

Further derivation adapted from [**KumarNardeep2013a**]. To extend reflectivity to a differential measurement

## 2.4 Coherent Multidimensional Spectroscopy

multiresonant coherent multidimensional spectroscopy

### 2.4.1 Three Wave

### 2.4.2 Four Wave

Fluorescence

Raman

### 2.4.3 Five Wave

### 2.4.4 Six Wave

multiple population-period transient spectroscopy (MUPPETS)

## 2.5 Strategies for CMDS

### 2.5.1 Homodyne vs. Heterodyne Detection

Two kinds of spectroscopies: 1) heterodyne 2) homodyne. Heterodyne techniques may be self heterodyne or explicitly heterodyned with a local oscillator.

In all heterodyne spectroscopies, signal goes as  $N$ . In all homodyne spectroscopies, signal goes as  $N^2$ . This literally means that homodyne signals go as the square of heterodyne signals, which is what we mean when we say that homodyne signals are intensity level and heterodyne signals are amplitude level.

Transient absorption, TA

### 2.5.2 Frequency vs. Time Domain

Time domain techniques become more and more difficult when large frequency bandwidths are needed.

With very short, broad pulses:

- Non-resonant signal becomes brighter relative to resonant signal
- Pulse distortions become important.

This epi-CARS paper might have some useful discussion of non-resonant vs resonant for shorter and shorter pulses [**ChengJixin2001a**].

An excellent discussion of pulse distortion phenomena in broadband time-domain experiments was published by **SpencerAustinP2015a**.

Another idea in defense of frequency domain is for the case of power studies. Since time-domain pulses in-fact possess all colors in them they cannot be trusted as much at perturbative fluence. See that paper that Natalia presented...

### **2.5.3 Triply Electronically Enhanced Spectroscopy**

Triply Electronically Enhanced (TrEE) spectroscopy has become the workhorse homodyne-detected 4WM experiment in the Wright Group.

### **2.5.4 Transient Absorbance Spectroscopy**

Transient absorption (TA)

#### **Quantitative TA**

Transient absorbance (TA) spectroscopy is a self-heterodyned technique. Through chopping you can measure nonlinearities quantitatively much easier than with homodyne detected (or explicitly heterodyned) experiments.

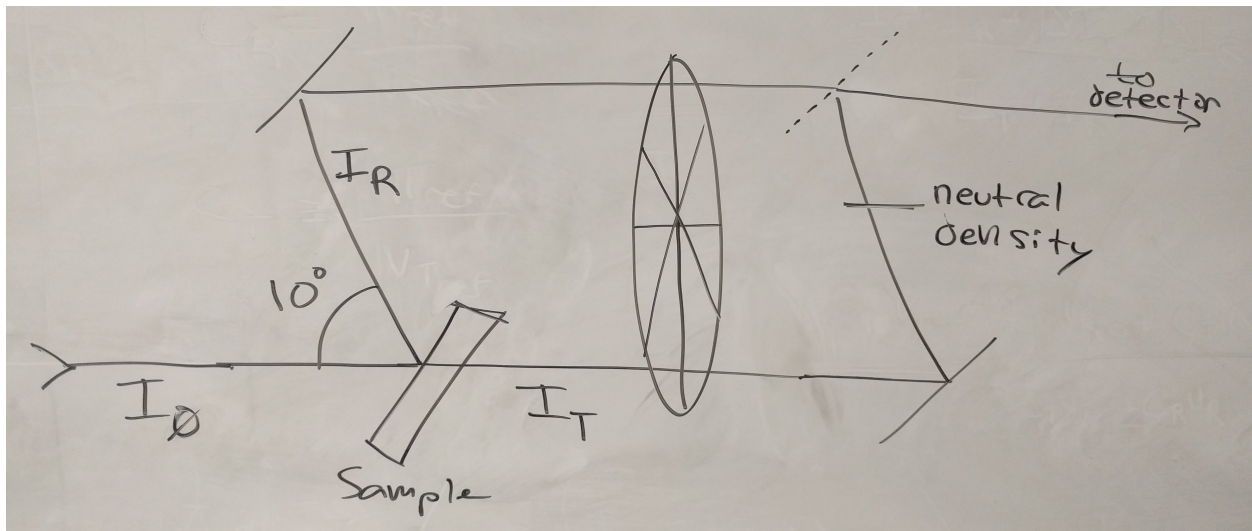


Figure 2.1: CAPTION TODO



Figure 2.1 diagrams the TA measurement for a generic sample. Here I show measurement of both the reflected and transmitted probe beam ... not important in opaque (pyrite) or non-reflective (quantum dot) samples ...

Typically one attempts to calculate the change in absorbance  $\Delta A$  ...

$$\Delta A = A_{\text{on}} - A_{\text{off}} \quad (2.2)$$

$$= -\log_{10} \left( \frac{I_T + I_R + I_{\Delta T} + I_{\Delta R}}{I_0} \right) + \log \left( \frac{I_T + I_R}{I_0} \right) \quad (2.3)$$

$$= -(\log_{10}(I_T + I_R + I_{\Delta T} + I_{\Delta R}) - \log_{10}(I_0)) + (\log_{10}(I_T + I_R) - \log_{10}(I_0)) \quad (2.4)$$

$$= -(\log_{10}(I_T + I_R + I_{\Delta T} + I_{\Delta R}) - \log_{10}(I_T + I_R)) \quad (2.5)$$

$$= -\log_{10} \left( \frac{I_T + I_R + I_{\Delta T} + I_{\Delta R}}{I_T + I_R} \right) \quad (2.6)$$

Equation 2.6 simplifies beautifully if reflectivity is negligible ...

Now I define a variable for each experimental measurable:

$V_T$	voltage recorded from transmitted beam, without pump
$V_R$	voltage recorded from reflected beam, without pump
$V_{\Delta T}$	change in voltage recorded from transmitted beam due to pump
$V_{\Delta R}$	change in voltage recorded from reflected beam due to pump

We will need to calibrate using a sample with a known transmissivity and reflectivity constant:

$V_{T, \text{ref}}$	voltage recorded from transmitted beam, without pump
$V_{R, \text{ref}}$	voltage recorded from reflected beam, without pump
$\mathcal{T}_{\text{ref}}$	transmissivity
$\mathcal{R}_{\text{ref}}$	reflectivity

Define two new proportionality constants...

$$C_T \equiv \frac{\mathcal{T}}{V_T} \quad (2.7)$$

$$C_R \equiv \frac{\mathcal{R}}{V_R} \quad (2.8)$$

These are explicitly calibrated (as a function of probe color) prior to the experiment using the calibration sample.

Given the eight experimental measurables ( $V_T$ ,  $V_R$ ,  $V_{\Delta T}$ ,  $V_{\Delta R}$ ,  $V_{T, \text{ref}}$ ,  $V_{R, \text{ref}}$ ,  $\mathcal{T}_{\text{ref}}$ ,  $\mathcal{R}_{\text{ref}}$ ) I can express all of the intensities in Equation 2.6 in terms of  $I_0$ .

$$C_T = \frac{\mathcal{T}_{\text{ref}}}{V_{T, \text{ref}}} \quad (2.9)$$

$$C_R = \frac{\mathcal{R}_{\text{ref}}}{V_{R, \text{ref}}} \quad (2.10)$$

$$I_T = I_0 C_T V_T \quad (2.11)$$

$$I_R = I_0 C_R V_R \quad (2.12)$$

$$I_{\Delta T} = I_0 C_T V_{\Delta T} \quad (2.13)$$

$$I_{\Delta R} = I_0 C_R V_{\Delta R} \quad (2.14)$$

Wonderfully, the  $I_0$  cancels when plugged back in to Equation 2.6, leaving a final expression for  $\Delta A$  that only depends on my eight measurables.

$$\Delta A = -\log_{10} \left( \frac{C_T(V_T + V_{\Delta T}) + C_R(V_R + V_{\Delta R})}{C_T V_T + C_R V_R} \right) \quad (2.15)$$

### 2.5.5 Cross Polarized TrEE

### 2.5.6 Pump-TrEE-Probe

Pump TrEE probe (PTP).

## 2.6 Instrumental Response Function

The instrumental response function (IRF) is a classic concept in analytical science. Defining IRF becomes complex with instruments as complex as these, but it is still useful to attempt.

It is particularly useful to define bandwidth.

### 2.6.1 Time Domain

I will use four wave mixing to extract the time-domain pulse-width. I use a driven signal *e.g.* near infrared carbon tetrachloride response. I'll homodyne-detect the output. In my experiment I'm moving pulse 1 against pulses 2 and 3 (which are coincident).

The driven polarization,  $P$ , goes as the product of my input pulse *intensities*:

$$P(T) = I_1(t - T) \times I_2(t) \times I_3(t) \quad (2.16)$$

In our experiment we are convolving  $I_1$  with  $I_2 \times I_3$ . Each pulse has an *intensity-level* width,  $\sigma_1$ ,  $\sigma_2$ , and  $\sigma_3$ .  $I_2 \times I_3$  is itself a Gaussian, and

$$\sigma_{I_2 I_3} = \dots \quad (2.17)$$

$$= \sqrt{\frac{\sigma_2^2 \sigma_3^2}{\sigma_2^2 + \sigma_3^2}}. \quad (2.18)$$

The width of the polarization (across  $T$ ) is therefore

$$\sigma_P = \sqrt{\sigma_1^2 + \sigma_2^2 l_3} \quad (2.19)$$

$$= \dots \quad (2.20)$$

$$= \sqrt{\frac{\sigma_1^2 + \sigma_2^2 \sigma_3^2}{\sigma_1^2 + \sigma_2^2}}. \quad (2.21)$$

I assume that all of the pulses have the same width.  $l_1$ ,  $l_2$ , and  $l_3$  are identical Gaussian functions with FWHM  $\sigma$ . In this case, Equation 2.21 simplifies to

$$\sigma_P = \sqrt{\frac{\sigma^2 + \sigma^2 \sigma^2}{\sigma^2 + \sigma^2}} \quad (2.22)$$

$$= \dots \quad (2.23)$$

$$= \sigma \sqrt{\frac{3}{2}} \quad (2.24)$$

Finally, since we measure  $\sigma_P$  and wish to extract  $\sigma$ :

$$\sigma = \sigma_P \sqrt{\frac{2}{3}} \quad (2.25)$$

Again, all of these widths are on the *intensity* level.

## 2.6.2 Frequency Domain

We can directly measure  $\sigma$  (the width on the intensity-level) in the frequency domain using a spectrometer. A tune test contains this information.

### 2.6.3 Time-Bandwidth Product

For a Gaussian, approximately 0.441



## Chapter 3

# Materials

"Kroemer's Lemma of Proven Ignorance": If, in discussing a semiconductor problem, you cannot draw an Energy Band Diagram, this shows that you don't know what you are talking about, If you can draw one, but don't, then your audience won't know what you are talking about.





## Chapter 4

# Software

*The following guidelines are to be used in the documentation of all software developed in the Wright group for the IBM 9000 computer. These rules have arisen as a necessary consequence of the group's programming philosophy of writing software in the form of units which can be readily shared among a number of programmers. The approach outlined here should help to avoid some of the confusion otherwise produced by several persons simultaneously developing and modifying shared software.*

– Roger Carlson, "Software Development Guidelines" (1988) [**CarlsonRogerJ1988a**]

Cutting-edge science increasingly relies on custom software. In their 2008 survey, Hannay et al. [2] demonstrated just how important software is to the modern scientist.

1. 84.3% of surveyed scientists state that developing scientific software is important or very important for their own research.
2. 91.2% of surveyed scientists state that using scientific software is important or very important for their own research.
3. On average, scientists spend approximately 40% of their work time using scientific software.
4. On average, scientists spend approximately 30% of their work time developing scientific software.

Despite the importance of software to science and scientists, most scientists are not familiar with basic software engineering concepts. This is in part due to their general lack of formal training in programming and software development. Hannay et al. [2] found that over 90% of scientists learn software development through 'informal self study'. Indeed, I myself have never been formally trained in software development.

Software development in a scientific context poses unique challenges. Many traditional software development paradigms demand an upfront articulation of goals and requirements. This allows the developers to carefully design their software, even before a single line of code is written. In her seminal 2005 case study Segal [3] describes a collaboration between a team of researchers and a contracted team of software engineers. Ultimately

## **Part II**

# **Development**



## Chapter 5

# Processing

From a data science perspective, CMDS has several unique challenges:

1. Dimensionality of datasets can typically be greater than two, complicating **representation**.
2. Shape and dimensionality change...
3. Data can be large (over one million points).

I have designed a software package that directly addresses these issues.

WrightTools is a software package at the heart of all work in the Wright Group.

### 5.1 Data object model

WrightTools uses a programming strategy called object oriented programming (OOP).

It contains a central data “container” that is capable of storing all of the information about each multidimensional (or one-dimensional) spectra.

## Python interface

WrightTools is written in Python, and endeavors to have a “pythonic”, explicit and “natural” application programming interface (API). To use WrightTools, simply import:

---

```
import numpy as np

def incmatrix(genl1,genl2):
    m = len(genl1)
    n = len(genl2)
    M = None #to become the incidence matrix
    VT = np.zeros((n*m,1), int) #dummy variable

    #compute the bitwise xor matrix
    M1 = bitxormatrix(genl1)
    M2 = np.triu(bitxormatrix(genl2),1)

    for i in range(m-1):
        for j in range(i+1, m):
            [r,c] = np.where(M2 == M1[i,j])
            for k in range(len(r)):
                VT[(i)*n + r[k]] = 1;
                VT[(i)*n + c[k]] = 1;
                VT[(j)*n + r[k]] = 1;
                VT[(j)*n + c[k]] = 1;

            if M is None:
                M = np.copy(VT)
            else:
                M = np.concatenate((M, VT), 1)

        VT = np.zeros((n*m,1), int)

    return M
```

---

wt5 file format

## **5.2 Artists**

## **5.3 Fitting**

## **5.4 Distribution and licensing**

## **5.5 Future directions**





## **Chapter 6**

# **Acquisition**

In the Wright Group, PyCMDS replaces the old acquisition softwares 'ps control', written by Kent Meyer and 'Control for Lots of Research in Spectroscopy' written by Schuyler Kain.

PyCMDS directly addresses the hardware during experiments.

## 6.1 Overview

PyCMDS has, through software improvements alone, dramatically lessened scan times...

- simultaneous motor motion
- digital signal processing
- ideal axis positions 6.2.1

## 6.2 Future directions

### 6.2.1 Ideal Axis Positions

Frequency domain multidimensional spectroscopy is a time-intensive process. A typical pixel takes between one-half second and three seconds to acquire. Depending on the exact hardware being scanned and signal being detected, this time may be mostly due to hardware motion or signal collection. Due to the curse of dimensionality, a typical three-dimensional CMDS experiment contains roughly 100,000 pixels. CMDS hardware is transiently-reliable, so speeding up experiments is a crucial component of unlocking ever larger dimensionalities and higher resolutions.

One obvious way to decrease the scan-time is to take fewer pixels. Traditionally, multidimensional scans are done with linearly arranged points in each axis—this is the simplest configuration to program into the acquisition software. Because signal features are often sparse or slowly varying (especially so in high-dimensional scans) linear stepping means that *most of the collected pixels* are duplicates or simply noise. A more intelligent choice of axis points can capture the same nonlinear spectrum in a fraction of the total pixel count.

An ideal distribution of pixels is linearized in *signal*, not coordinate. This means that every signal level (think of a contour in the N-dimensional case) has roughly the same number of pixels defining it. If some generic multidimensional signal goes between 0 and 1, one would want roughly 10% of the pixels to be between 0.9 and 1.0, 10% between 0.8 and 0.9 and so on. If the signal is sparse in the space explored (imagine a narrow two-dimensional Lorentzian in the center of a large 2D-Frequency scan) this would place the majority of the pixels near the narrow peak feature(s), with only a few of them defining the large (in axis space) low-signal floor. In contrast linear stepping would allocate the vast majority of the pixels in the low-signal 0.0 to 0.1 region, with only a few being used to capture the narrow peak feature. Of course, linearizing pixels in signal requires prior expectations about the shape of the multidimensional signal—linear stepping is still an appropriate choice for low-resolution “survey” scans.

CMDS scans often possess correlated features in the multidimensional space. In order to capture such features as cheaply as possible, one would want to define regions of increased pixel density along the correlated (diagonal) lineshape. As a concession to reasonable simplicity, our acquisition software (PyCMDS) assumes that all scans constitute a regular array with-respect-to the scanned axes. We can acquire arbitrary points along each axis, but not for the multidimensional scan. This means that we cannot achieve strictly ideal pixel distributions for arbitrary datasets. Still, we can do much better than linear spacing.

Almost all CMDS lineshapes (in frequency and delay) can be described using just a few lineshape functions:

1. exponential
2. Gaussian
3. Lorentzian
4. bimolecular

Exponential and bimolecular dynamics fall out of simple first and second-order kinetics (I will ignore higher-order kinetics here). Gaussians come from our Gaussian pulse envelopes or from normally-distributed inhomogeneous broadening. The measured line-shapes are actually convolutions of the above. I will ignore the convolution except for a few illustrative special cases. More exotic lineshapes are possible in CMDS—quantum beating and breathing modes, for example—I will also ignore these.

Derivations of the ideal pixel positions for each of these lineshapes appear below.

## 6.2.2 Exponential

Simple exponential decays are typically used to describe population and coherence-level dynamics in CMDS. For some generic exponential signal  $S$  with time constant  $\tau$ ,

$$S(t) = e^{-\frac{t}{\tau}}. \quad (6.1)$$

We can write the conjugate equation to 6.1, asking “what  $t$  do I need to get a certain signal level?”:

$$\log(S) = -\frac{t}{\tau} \quad (6.2)$$

$$t = -\tau \log(S). \quad (6.3)$$

So to step linearly in  $t$ , my step size has to go as  $-\tau \log(S)$ .

We want to go linearly in signal, meaning that we want to divide  $S$  into even sections. If  $S$  goes from 0 to 1 and we choose to acquire  $N$  points,

$$t_n = -\tau \log\left(\frac{n}{N}\right). \quad (6.4)$$

Note that  $t_n$  starts at long times and approaches zero delay. So the first  $t_1$  is the smallest signal and  $t_N$  is the largest.

Now we can start to consider realistic cases, like where  $\tau$  is not quite known and where some other longer dynamics persist (manifested as a static offset). Since these values are not separable in a general

system, I'll keep  $S$  normalized between 0 and 1.

$$S = (1 - c) e^{-\frac{t}{\tau_{\text{actual}}}} + c \quad (6.5)$$

$$S_n = (1 - c) e^{-\frac{-\tau_{\text{step}} \log\left(\frac{n}{N}\right)}{\tau_{\text{actual}}}} + c \quad (6.6)$$

$$S_n = (1 - c) e^{-\frac{\tau_{\text{step}} \log\left(\frac{N}{n}\right)}{\tau_{\text{actual}}}} + c \quad (6.7)$$

$$S_n = (1 - c) \left(\frac{N}{n}\right)^{-\frac{\tau_{\text{step}}}{\tau_{\text{actual}}}} + c \quad (6.8)$$

$$S_n = (1 - c) \left(\frac{n}{N}\right)^{\frac{\tau_{\text{step}}}{\tau_{\text{actual}}}} + c \quad (6.9)$$

[p!]

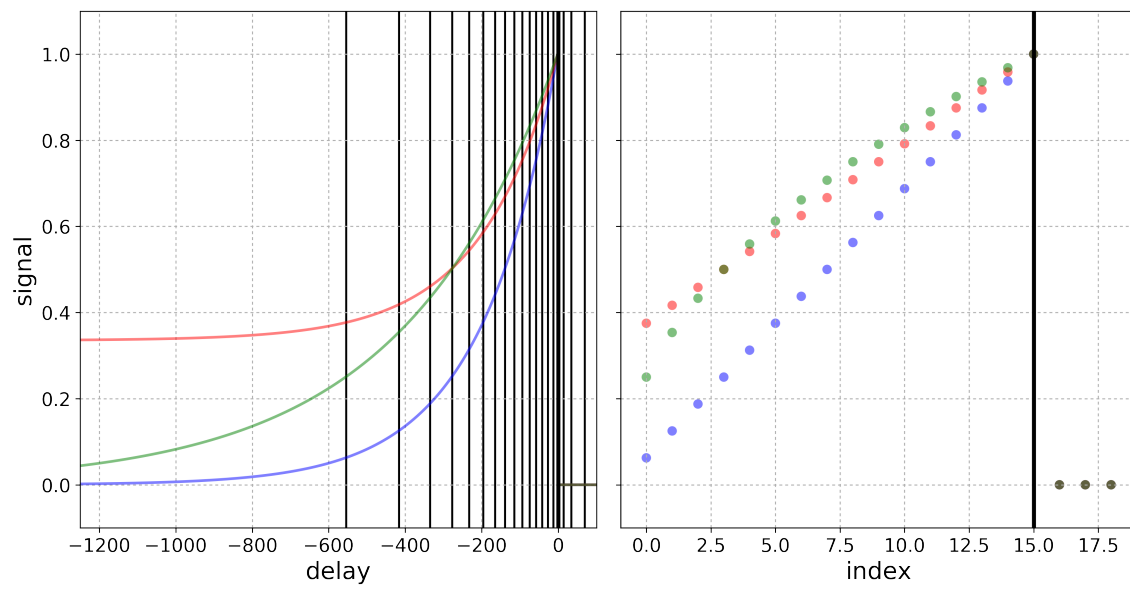


Figure 6.1: TODO

**Gaussian**

**Lorentzian**

**Bimolecular**





## Chapter 7

# Active Correction in MR-CMDS

### 7.1 Hardware

#### 7.1.1 Delay Stages

### 7.2 Signal Acquisition

Old boxcar: 300 ns window, 10 microsecond delay. Onset of saturation 2 V.

#### 7.2.1 Digital Signal Processing

### 7.3 Artifacts and Noise

#### 7.3.1 Scatter

Scatter is a complex microscopic process whereby light traveling through a material elastically changes its propagation direction. In CMDS we use propagation direction to isolate signal. Scattering samples defeat this isolation step and allow some amount of excitation light to reach the detector. In homodyne-

detected 4WM experiments,

$$I_{\text{detected}} = |E_{4\text{WM}} + E_1 + E_2 + E_{2'}|^2 \quad (7.1)$$

Where  $E$  is the entire time-dependent complex electromagnetic field. When expanded, the intensity will be composed of diagonal and cross terms:

$$\begin{aligned} I_{\text{detected}} = & \overline{(E_1 + E_2)E_{2'}} + (E_1 + E_2)\overline{E_{2'}} + |E_1 + E_2|^2 + (E_1 + E_2)\overline{E_{4\text{WM}}} \\ & + (E_1 + E_2)\overline{E_{4\text{WM}}} + \overline{E_{2'}}E_{4\text{WM}} + E_{2'}\overline{E_{4\text{WM}}} + |E_{4\text{WM}}|^2 \end{aligned} \quad (7.2)$$

A similar expression in the case of heterodyne-detected 4WM is derived by **BrixnerTobias2004a**. The goal of any 'scatter rejection' processing procedure is to isolate  $|E_{4\text{WM}}|^2$  from the other terms.

## Abandon the Random Phase Approximation

### Interference Patterns in TrEE

TrEE is implicitly homodyne-detected. Scatter from excitation fields will interfere on the amplitude level with TrEE signal, causing interference patterns that beat in delay and frequency space. The pattern of beating will depend on which excitation field(s) reach(es) the detector, and the parameterization of delay space chosen.

First I focus on the interference patterns in 2D delay space where all excitation fields and the detection field are at the same frequency.

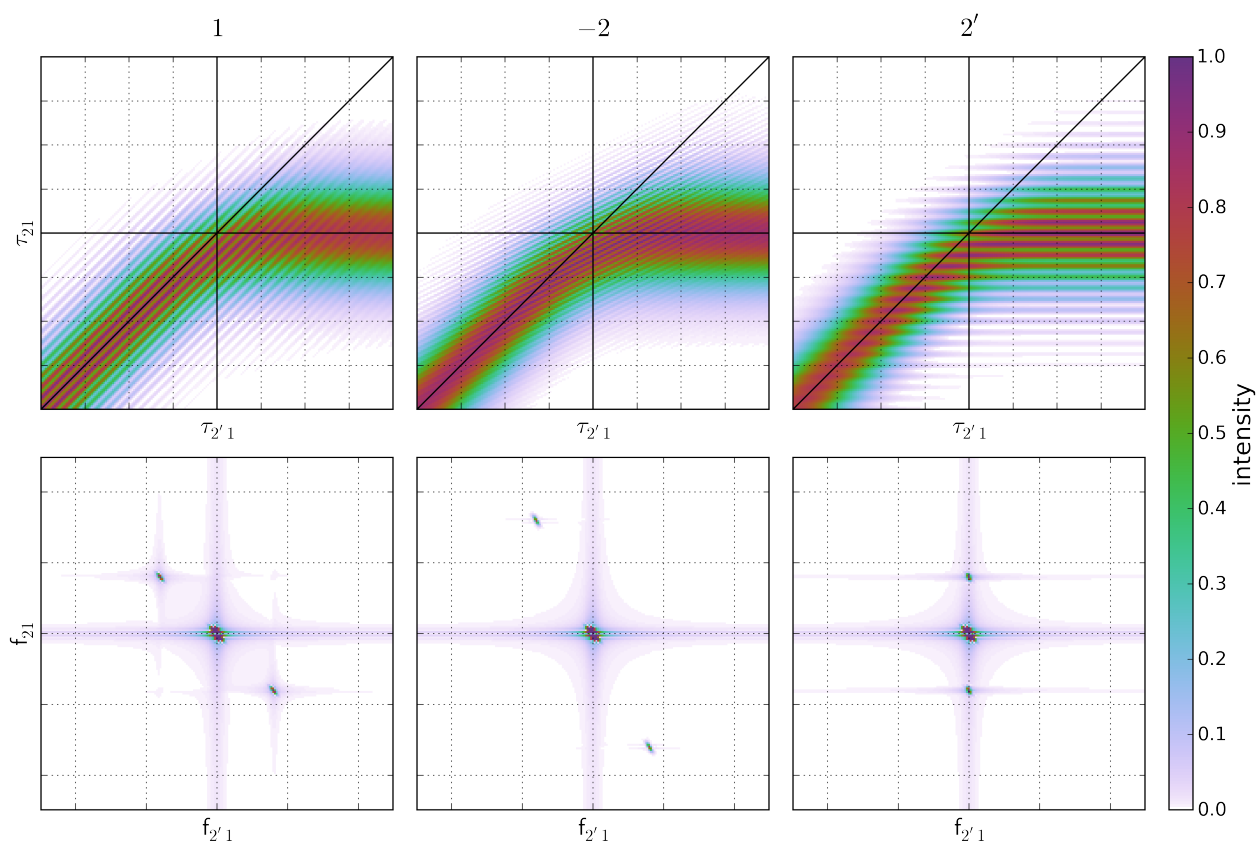


Figure 7.1: Numerically simulated interference patterns between scatter and TrEE for the old delay parametrization. Each column has scatter from a single excitation field. The top row shows the measured intensities, the bottom row shows the 2D Fourier transform, with the colorbar's dynamic range chosen to show the cross peaks.

labelfig:scatterinterferenceinTrEEold

Here I derive the slopes of constant phase for the old delay space, where  $d1 = \tau_{2'1}$  and  $d2 = \tau_{21}$ . For simplicity, I take  $\tau_1$  to be 0, so that  $\tau_{21} \rightarrow \tau_2$  and  $\tau_{2'1} \rightarrow \tau_{2'}$ . The phase of signal is then

$$\Phi_{\text{sig}} = e^{-((\tau_{2'} - \tau_2)\omega)} \quad (7.3)$$

The phase of each excitation field can also be written:

$$\Phi_1 = e^0 \quad (7.4)$$

$$\Phi_2 = e^{-\tau_2\omega} \quad (7.5)$$

$$\Phi_{2'} = e^{-\tau_{2'}\omega} \quad (7.6)$$

The cross term between scatter and signal is the product of  $\Phi_{\text{sig}}$  and  $\Phi_{\text{scatter}}$ . The cross terms are:

$$\Delta_1 = \Phi_{\text{sig}} = e^{-((\tau_{2'} - \tau_2)\omega)} \quad (7.7)$$

$$\Delta_2 = \Phi_{\text{sig}}e^{-\tau_2\omega} = e^{-((\tau_{2'} - 2\tau_2)\omega)} \quad (7.8)$$

$$\Delta_{2'} = \Phi_{\text{sig}}e^{-\tau_{2'}\omega} = e^{-\tau_2\omega} \quad (7.9)$$

Figure ?? presents numerical simulations of scatter interference as a visual aid. See Yurs 2011 [**YursLenaA2011a**].

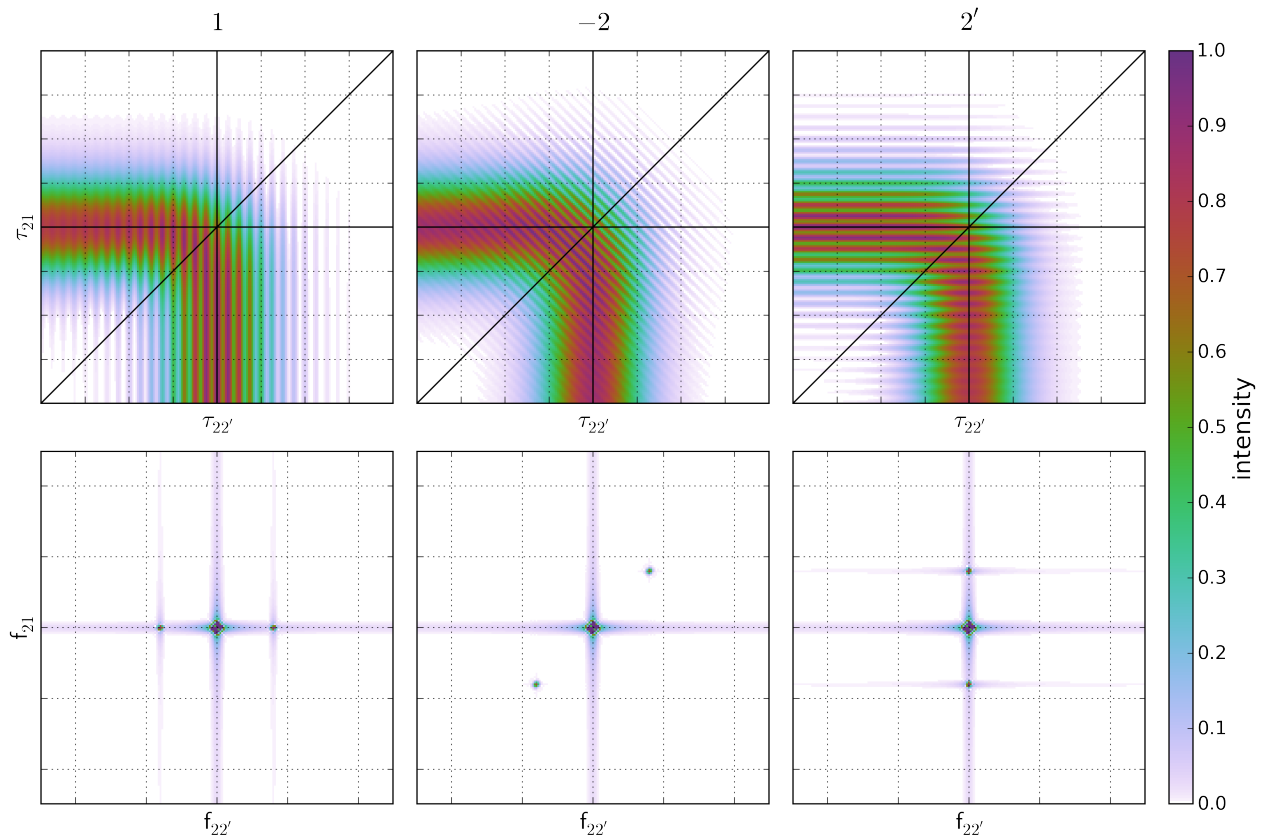


Figure 7.2: Numerically simulated interference patterns between scatter and TrEE for the current delay parametrization. Each column has scatter from a single excitation field. The top row shows the measured intensities, the bottom row shows the 2D Fourier transform, with the colorbar's dynamic range chosen to show the cross peaks.

Here I derive the slopes of constant phase for the current delay space, where  $d1 = \tau_{22'}$  and  $d2 = \tau_{21}$ . I take  $\tau_2$  to be 0, so that  $\tau_{22'} \rightarrow \tau_{2'}$  and  $\tau_{21} \rightarrow \tau_1$ . The phase of the signal is then

$$\Phi_{\text{sig}} = e^{-((\tau_{2'} + \tau_1)\omega)} \quad (7.10)$$

The phase of each excitation field can also be written:

$$\Phi_1 = e^{-\tau_1\omega} \quad (7.11)$$

$$\Phi_2 = e^0 \quad (7.12)$$

$$\Phi_{2'} = e^{-\tau_{2'}\omega} \quad (7.13)$$

The cross term between scatter and signal is the product of  $\Phi_{\text{sig}}$  and  $\Phi_{\text{scatter}}$ . The cross terms are:

$$\Delta_1 = \Phi_{\text{sig}}e^{-\tau_1\omega} = e^{-\tau_{2'}\omega} \quad (7.14)$$

$$\Delta_2 = \Phi_{\text{sig}} = e^{-((\tau_2 + \tau_1)\omega)} \quad (7.15)$$

$$\Delta_{2'} = \Phi_{\text{sig}}e^{-\tau_{2'}\omega} = e^{-\tau_1\omega} \quad (7.16)$$

Figure 7.2 presents numerical simulations of scatter interference for the current delay parameterization.

### Instrumental Removal of Scatter

The effects of scatter can be entirely removed from CMDS signal by combining two relatively straightforward instrumental techniques: *chopping* and *fibrillation*. Conceptually, chopping removes intensity-level offset terms and fibrillation removes amplitude-level interference terms. Both techniques work by modulating signal and scatter terms differently so that they may be separated after light collection.

We use the dual chopping scheme developed by **FurutaKoichi2012a** called 'phase shifted parallel modulation'. In this scheme, two excitation sources are chopped at 1/4 of the laser repetition rate (two pulses on, two pulses off). Very similar schemes are discussed by **AugulisRamunas2011a** and **HeislerIsmael2014a** for two-dimensional electronic spectroscopy. The two chop patterns are phase-shifted to make the four-pulse pattern represented in Table 7.1. In principle this chopping scheme can be

	A	B	C	D
signal			✓	
scatter 1		✓	✓	
scatter 2			✓	✓
other	✓	✓	✓	✓

Table 7.1: Four shot-types in a general phase shifted parallel modulation scheme. The 'other' category represents anything that doesn't depend on either chopper, including scatter from other excitation sources, background light, detector voltage offsets, etc.

achieved with a single judiciously placed mechanical chopper - this is one of the advantages of Furuta's scheme. Due to practical considerations we have generally used two choppers, one on each OPA. The key to phase shifted parallel modulation is that signal only appears when both of your chopped beams are passed. It is simple to show how signal can be separated through simple addition and subtraction of the A, B, C, and D phases shown in Table 7.1. First, the components of each phase:

$$A = I_{\text{other}} \quad (7.17)$$

$$B = I_1 + I_{\text{other}} \quad (7.18)$$

$$C = I_{\text{signal}} + I_1 + I_2 + I_{\text{other}} \quad (7.19)$$

$$D = I_2 + I_{\text{other}} \quad (7.20)$$

Grouping into difference pairs,

$$A - B = -I_1 \quad (7.21)$$

$$C - D = I_{\text{signal}} + I_1 \quad (7.22)$$

So:

$$A - B + C - D = I_{\text{signal}} \quad (7.23)$$

I have ignored amplitude-level interference terms in this treatment because they cannot be removed via any chopping strategy. Interference between signal and an excitation beam will only appear in 'C'-type shots, so it will not be removed in Equation 7.23. To remove such interference terms, you must *fibrillate* your excitation fields.

An alternative to dual chopping is single-chopping and 'leveling'... this technique was used prior to May 2016 in the Wright Group... 'leveling' and single-chopping is also used in some early 2DES work... [BrixnerTobias2004a].



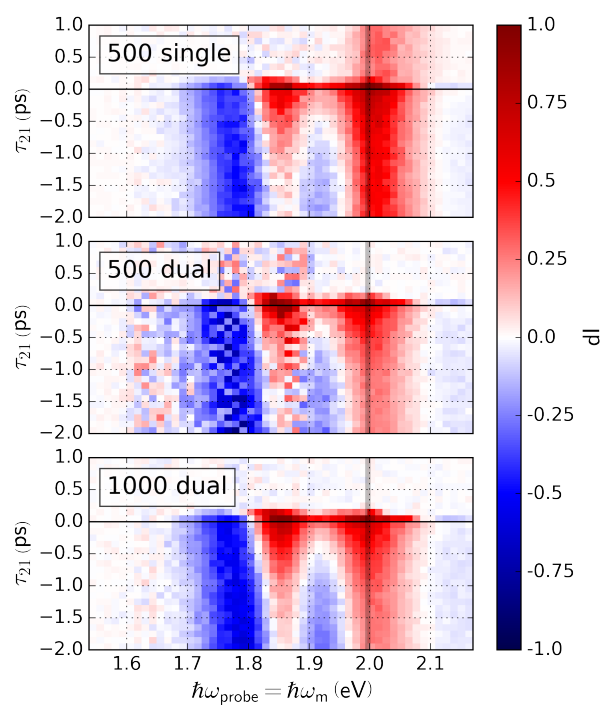


Figure 7.3: Comparison of single and dual chopping in a MoS<sub>2</sub> transient absorption experiment. Note that this data has not been processed in any way - the colorbar represents changes in intensity seen by the detector. The grey line near 2 eV represents the pump energy. The inset labels are the number of laser shots taken and the chopping strategy used.

Figure 7.3 shows the effects of dual chopping for some representative MoS<sub>2</sub> TA data. Each subplot is a probe wigner, with the vertical grey line representing the pump energy. Note that the single chopper passes pump scatter, visible as a time-invariant increase in intensity when the probe and monochromator are near the pump energy. Dual chopping efficiently removes pump scatter, but at the cost of signal to noise for the same number of laser shots. Taking twice as many laser shots when dual chopping brings the signal to noise to at least as good as the original single chopping.

Fibrillation is the intentional randomization of excitation phase during an experiment. Because the interference term depends on the phase of the excitation field relative to the signal, averaging over many shots with random phase will cause the interference term to approach zero. This is a well known strategy for removing unwanted interference terms [SpectorIvanC2015a, McClainBrianL2004a].

### 7.3.2 Normalization of dual-chopped self-heterodyned signal

Shot-by-shot normalization is not trivial for these experiments. As in table above, with 1 as pump and 2 as probe.

Starting with  $\Delta I$  from 7.23, we can normalize by probe intensity to get the popular  $\Delta I/I$  representation.

Using the names defined above:

$$\frac{\Delta I}{I} = \frac{A - B + C - D}{D - A} \quad (7.24)$$

Now consider the presence of excitation intensity monitors, indicated by subscripts PR for probe and PU for pump.

We can further normalize by the pump intensity by dividing the entire expression by  $C_{PU}$ :

$$\frac{\Delta I}{I} = \frac{A - B + C - D}{(D - A) * C_{PU}} \quad (7.25)$$

Now, substituting in BRAZARD formalism:

$$A = \text{constant} \quad (7.26)$$

$$B = SI_{PU}^B(1 + \delta_{PU}^B) \quad (7.27)$$

$$C = I_{PR}^C(1 + \delta_{PR}^C) + SI_{PU}^C(1 + \delta_{PR}^C) \quad (7.28)$$

$$D = I_{PR}^D(1 + \delta_{PR}^D) \quad (7.29)$$

$$\frac{\Delta I}{I} = \frac{\langle A \rangle - \frac{\langle B_{PU} \rangle B}{B_{PU}} + \frac{\langle C_{PU} \rangle \langle C_{PR} \rangle C}{C_{PU} C_{PR}} - \frac{\langle D_{PR} \rangle D}{D_{PR}}}{\langle PR \rangle \langle PU \rangle} \quad (7.30)$$

## 7.4 Light Generation

### 7.4.1 Automated OPA Tuning

## 7.5 Optomechanics

### 7.5.1 Automated Neutral Density Wheels



## Chapter 8

# A robust, fully automated algorithm to collect high quality OPA tuning curves

*Principle design features of the new EVV 2DIR optical delivery system include the following:*

- 1. Pairs of motorized gimbal mount mirrors on each OPA to compensate beam pointing changes.*
- 2. Automated calibration of OPAs, delay stages and motorized mounts.*

– Paul Donaldson, “Improving ... EVV 2DIR Spectroscopy” (2007) [[DonaldsonPaulMurray2007a](#)]

This chapter pasted from publication...

## Chapter 9

# Disentangling material and instrument response

*This Chapter borrows extensively from KohlerDanielDavid2017a.*

Ultrafast spectroscopy is often collected in the mixed frequency/time domain, where pulse durations are similar to system dephasing times. In these experiments, expectations derived from the familiar driven and impulsive limits are not valid. This work simulates the mixed-domain Four Wave Mixing response of a model system to develop expectations for this more complex field-matter interaction. We explore frequency and delay axes. We show that these line shapes are exquisitely sensitive to excitation pulse widths and delays. Near pulse overlap, the excitation pulses induce correlations which resemble signatures of dynamic inhomogeneity. We describe these line shapes using an intuitive picture that connects to familiar field-matter expressions. We develop strategies for distinguishing pulse-induced correlations from true system inhomogeneity. These simulations provide a foundation for interpretation of ultrafast experiments in the mixed domain.

## 9.1 Introduction

Ultrafast spectroscopy is based on using nonlinear interactions, created by multiple ultrashort ( $10^{-9}$  –  $10^{-15}$ s) pulses, to resolve spectral information on timescales as short as the pulses themselves. [RentzepisPM1970a, MukamelShaul2000a] The ultrafast spectra can be collected in the time domain or the frequency domain. [ParkKisam1998a]

Time-domain methods scan the pulse delays to resolve the free induction decay (FID). [GallagherSarahM1998a] The Fourier Transform of the FID gives the ultrafast spectrum. Ideally, these experiments are performed in the impulsive limit where FID dominates the measurement. FID occurs at the frequency of the transition that has been excited by a well-defined, time-ordered sequence of pulses. Time-domain methods are compromised when the dynamics occur on faster time scales than the ultrafast excitation pulses. As the pulses temporally overlap, FID from other pulse time-orderings and emission driven by the excitation pulses both become important. These factors are responsible for the complex “coherent artifacts” that are often ignored in pump-probe and related methods. [LebedevMV2007a, VardenyZ1981a, JoffreM1988a, PollardW1992a] Dynamics faster than the pulse envelopes are best measured using line shapes in frequency domain methods.

Frequency-domain methods scan pulse frequencies to resolve the ultrafast spectrum directly. [DruetSAJ1979a, OudarJL1980a] Ideally, these experiments are performed in the driven limit where the steady state dominates the measurement. In the driven limit, all time-orderings of the pulse interactions are equally important and FID decay is negligible. The output signal is driven at the excitation pulse frequencies during the excitation pulse width. Frequency-domain methods are compromised when the spectral line shape is narrower than the frequency bandwidth of the excitation pulses. Dynamics that are slower than the pulse envelopes can be measured in the time domain by resolving the phase oscillations of the output signal during the entire FID decay.

There is also the hybrid mixed-time/frequency-domain approach, where pulse delays and pulse frequencies are both scanned to measure the system response. This approach is uniquely suited for experiments where the dephasing time is comparable to the pulse durations, so that neither frequency-domain nor time-domain approaches excel on their own. [OudarJL1980a, WrightJohnCurtis1997b,



**WrightJohnCurtis1991a**] In this regime, both FID and driven processes are important. [**PakoulevAndreiV2006a**] Their relative importance depends on pulse frequencies and delays. Extracting the correct spectrum from the measurement then requires a more complex analysis that explicitly treats the excitation pulses and the different time-orderings. [**PakoulevAndreiV2007a**, **KohlerDanielDavid2014a**, **GelinMaximF2009b**] Despite these complications, mixed-domain methods have a practical advantage: the dual frequency- and delay-scanning capabilities allow these methods to address a wide variety of dephasing rates.

The relative importance of FID and driven processes and the changing importance of different coherence pathways are important factors for understanding spectral features in all ultrafast methods. These methods include partially-coherent methods involving intermediate populations such as pump-probe [**HammPeter2000a**], transient grating [**SalcedoJR1978a**, **FourkasJohnT1992a**, **FourkasJohnT1992b**], transient absorption/reflection [**AubockGerald2012a**, **BakkerHJ2002a**], photon echo [**DeBoeijWimP1996a**, **PattersonFG1984a**, **TokmakoffAndrei1995a**], two dimensional-infrared spectroscopy (2D-IR) [**HammPeter1999a**, **AsplundMC2000a**, **ZanniMartinT2001a**], 2D-electronic spectroscopy (2D-ES) [**HyblJohnD2001b**, **BrixnerTobias2004a**], and three pulse photon echo peak shift (3PEPS) [**EmdeMichelF1998a**, **DeBoeijWimP1996a**, **DeBoeijWimP1995a**, **ChoMinhaeng1992a**, **PassinoSeanA1997a**] spectroscopies. These methods also include fully-coherent methods involving only coherences such as Stimulated Raman Spectroscopy (SRS) [**YoonSangwoon2005a**, **McCamantDavidW2005a**], Doubly Vibrationally Enhanced (DOVE) [**ZhaoWei1999a**, **ZhaoWei1999b**, **ZhaoWei2000a**, **MeyerKentA2003a**, **DonaldsonPaulMurray2007b**, **DonaldsonPaulMurray2008a**, **FournierFrederic2008a**], Triply Resonant Sum Frequency (TRSF) [**BoyleErinSelene2013b**, **BoyleErinSelene2014a**], Sum Frequency Generation (SFG) [**LagutchevAlexi2007a**], Coherent Anti-Stokes Raman Spectroscopy (CARS) [**CarlsonRogerJ1990b**, **CarlsonRogerJ1990c**, **CarlsonRogerJ1991a**], and other coherent Raman methods [**SteehlerJK1985a**].

This paper focuses on understanding the nature of the spectral changes that occur in Coherent Multi-dimensional Spectroscopy (CMDS) as experiments transition between the two limits of frequency- and time-domain methods. CMDS is a family of spectroscopies that use multiple delay and/or frequency axes to extract homogeneous and inhomogeneous broadening, as well as detailed information about spectral diffusion and chemical changes. [**KwacKijeong2003a**, **WrightJohnCurtis2016a**] For time-domain CMDS (2D-IR, 2D-ES), the complications that occur when the impulsive approximation does not strictly hold has only recently been addressed. [**PerlikVaclav2017a**, **SmallwoodChristopherL2016a**]

Frequency-domain CMDS methods, referred to herein as multi-resonant CMDS (MR-CMDS), have similar capabilities for measuring homogeneous and inhomogeneous broadening. Although these experiments are typically described in the driven limit, [GallagherSarahM1998a, FourkasJohnT1992a, FourkasJohnT1992b] many of the experiments involve pulse widths that are comparable to the widths of the system. [MeyerKentA2003a, DonaldsonPaulMurray2007b, PakoulevAndreiV2009a, ZhaoWei1999a, CzechKyleJonathan2015a, KohlerDanielDavid2014a] MR-CMDS then becomes a mixed-domain experiment whereby resonances are characterized with marginal resolution in both frequency and time. For example, DOVE spectroscopy involves three different pathways [WrightJohnCurtis2003a] whose relative importance depends on the relative importance of FID and driven responses. [DonaldsonPaulMurray2010a] In the driven limit, the DOVE line shape depends on the difference between the first two pulse frequencies so the line shape has a diagonal character that mimics the effects of inhomogeneous broadening. In the FID limit where the coherence frequencies are defined instead by the transition, the diagonal character is lost. Understanding these effects is crucial for interpreting experiments, yet these effects have not been characterized for MR-CMDS.

This work considers the third-order MR-CMDS response of a 3-level model system using three ultrafast excitation beams with the commonly used four-wave mixing (FWM) phase-matching condition,  $\vec{k}_{\text{out}} = \vec{k}_1 - \vec{k}_2 + \vec{k}_2'$ . Here, the subscripts represent the excitation pulse frequencies,  $\omega_1$  and  $\omega_2 = \omega_2'$ . These experimental conditions were recently used to explore line shapes of excitonic systems, [KohlerDanielDavid2014a, CzechKyleJonathan2015a] and have been developed on vibrational states as well. [MeyerKentA2004a] Although MR-CMDS forms the context of this model, the treatment is quite general because the phase matching condition can describe any of the spectroscopies mentioned above with the exception of SFG and TRSF, for which the model can be easily extended. We numerically simulate the MR-CMDS response with pulse durations at, above, and below the system coherence time. To highlight the role of pulse effects, we build an interpretation of the full MR-CMDS response by first showing how finite pulses affect the evolution of a coherence, and then how finite pulses affect an isolated third-order pathway. When considering the full MR-CMDS response, we show that spectral features change dramatically as a function of delay, even for a homogeneous system with elementary dynamics. Importantly, the line shape can exhibit correlations that mimic inhomogeneity, and the temporal evolution of this line shape can mimic spectral diffusion. We identify key signatures

that can help differentiate true inhomogeneity and spectral diffusion from these measurement artifacts.

## **9.2 Theory**

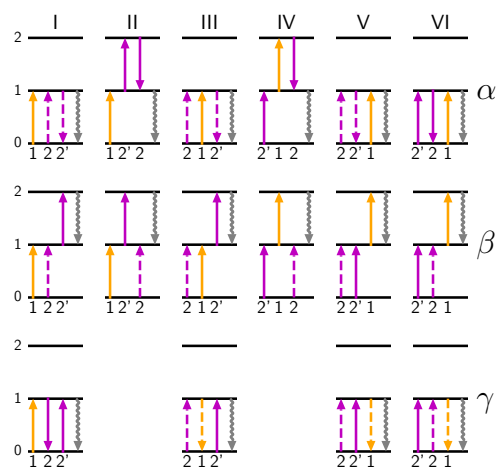


Figure 9.1: The sixteen triply-resonant Liouville pathways for the third-order response of the system used here. Time flows from left to right. Each excitation is labeled by the pulse stimulating the transition; excitations with  $\omega_1$  are yellow, excitations with  $\omega_2 = \omega_{2'}$  are purple, and the final emission is gray.

We consider a simple three-level system (states  $n = 0, 1, 2$ ) that highlights the multidimensional line shape changes resulting from choices of the relative dephasing and detuning of the system and the temporal and spectral widths of the excitation pulses. For simplicity, we will ignore population relaxation effects:  $\Gamma_{11} = \Gamma_{00} = 0$ .

The electric field pulses,  $\{E_I\}$ , are given by:

$$E_I(t; \omega_I, \tau_I, \vec{k}_I \cdot z) = \frac{1}{2} \left[ c_I(t - \tau_I) e^{i\vec{k}_I \cdot z} e^{-i\omega_I(t - \tau_I)} + c.c. \right], \quad (9.1)$$

where  $\omega_I$  is the field carrier frequency,  $\vec{k}_I$  is the wavevector,  $\tau_I$  is the pulse delay, and  $c_I$  is a slowly varying envelope. In this work, we assume normalized (real-valued) Gaussian envelopes:

$$c_I(t) = \frac{1}{\Delta_t} \sqrt{\frac{2 \ln 2}{2\pi}} \exp \left( -\ln 2 \left[ \frac{t}{\Delta_t} \right]^2 \right), \quad (9.2)$$

where  $\Delta_t$  is the temporal FWHM of the envelope intensity. We neglect non-linear phase effects such as chirp so the FWHM of the frequency bandwidth is transform limited:  $\Delta_\omega \Delta_t = 4 \ln 2 \approx 2.77$ , where  $\Delta_\omega$  is the spectral FWHM (intensity scale).

The Liouville-von Neumann Equation propagates the density matrix,  $\rho$ :

$$\frac{d\rho}{dt} = -\frac{i}{\hbar} \left[ \mathbf{H}_0 + \boldsymbol{\mu} \cdot \sum_{I=1,2,2'} E_I(t), \rho \right] + \boldsymbol{\Gamma} \rho. \quad (9.3)$$

Here  $\mathbf{H}_0$  is the time-independent Hamiltonian,  $\boldsymbol{\mu}$  is the dipole superoperator, and  $\boldsymbol{\Gamma}$  contains the pure dephasing rate of the system. We perform the standard perturbative expansion of Equation 9.3 to third order in the electric field interaction [MukamelShaul1995a, YeeTK1978a, OudarJL1980a, ArmstrongJA1962a, SchweigertIgorV2008a] and restrict ourselves only to the terms that have the correct spatial wave vector  $\vec{k}_{\text{out}} = \vec{k}_1 - \vec{k}_2 + \vec{k}_{2'}$ . This approximation narrows the scope to sets of three interactions, one from each field, that result in the correct spatial dependence. The set of three interactions have  $3! = 6$  unique time-ordered sequences, and each time-ordering produces either two or three unique system-field interactions for our system, for a total of sixteen unique system-field interaction sequences, or Liouville pathways, to consider. Fig. 9.1 shows these sixteen pathways as Wave Mixing

Energy Level (WMEL) diagrams[**LeeDuckhwan1985a**].

We first focus on a single interaction in these sequences, where an excitation pulse,  $x$ , forms  $\rho_{ij}$  from  $\rho_{ik}$  or  $\rho_{kj}$ . For brevity, we use  $\hbar = 1$  and abbreviate the initial and final density matrix elements as  $\rho_i$  and  $\rho_f$ , respectively. Using the natural frequency rotating frame,  $\tilde{\rho}_{ij} = \rho_{ij}e^{-i\omega_{ij}t}$ , the formation of  $\rho_f$  using pulse  $x$  is written as

$$\begin{aligned} \frac{d\tilde{\rho}_f}{dt} = & -\Gamma_f \tilde{\rho}_f \\ & + \frac{i}{2} \lambda_f \mu_f c_x(t - \tau_x) e^{i\kappa_f(\vec{k}_x \cdot \mathbf{z} + \omega_x \tau_x)} e^{i\kappa_f \Omega_{fx} t} \tilde{\rho}_i(t), \end{aligned} \quad (9.4)$$

where  $\Omega_{fx} = \kappa_f^{-1} \omega_f - \omega_x (= |\omega_f| - \omega_x)$  is the detuning,  $\omega_f$  is the transition frequency of the  $i^{th}$  transition,  $\mu_f$  is the transition dipole, and  $\Gamma_f$  is the dephasing/relaxation rate for  $\rho_f$ . The  $\lambda_f$  and  $\kappa_f$  parameters describe the phases of the interaction:  $\lambda_f = +1$  for ket-side transitions and  $-1$  for bra-side transitions, and  $\kappa_f$  depends on whether  $\rho_f$  is formed via absorption ( $\kappa_f = \lambda_f$ ) or emission ( $\kappa_f = -\lambda_f$ ).  $\kappa_f$  also has a direct relationship to the phase matching relationship: for transitions with  $E_2$ ,  $\kappa_f = 1$ , and for  $E_1$  or  $E_2'$ ,  $\kappa_f = -1$ . In the following equations we neglect spatial dependence ( $z = 0$ ).

Equation 9.4 forms the basis for our simulations. It provides a general expression for arbitrary values of the dephasing rate and excitation pulse bandwidth. The integral solution is

$$\begin{aligned} \tilde{\rho}_f(t) = & \frac{i}{2} \lambda_f \mu_f e^{i\kappa_f \omega_x \tau_x} e^{i\kappa_f \Omega_{fx} t} \\ & \times \int_{-\infty}^{\infty} c_x(t - u - \tau_x) \tilde{\rho}_i(t - u) \Theta(u) \\ & \times e^{-(\Gamma_f + i\kappa_f \Omega_{fx})u} du, \end{aligned} \quad (9.5)$$

where  $\Theta$  is the Heaviside step function. Equation 9.5 becomes the steady state limit expression when  $\Delta_t |\Gamma_f + i\kappa_f \Omega_{fx}| \gg 1$ , and the impulsive limit expression results when  $\Delta_t |\Gamma_f + i\kappa_f \Omega_{fx}| \ll 1$ . Both limits are important for understanding the multidimensional line shape changes discussed in this paper.

The steady state and impulsive limits of Equation 9.5 are discussed in TODO

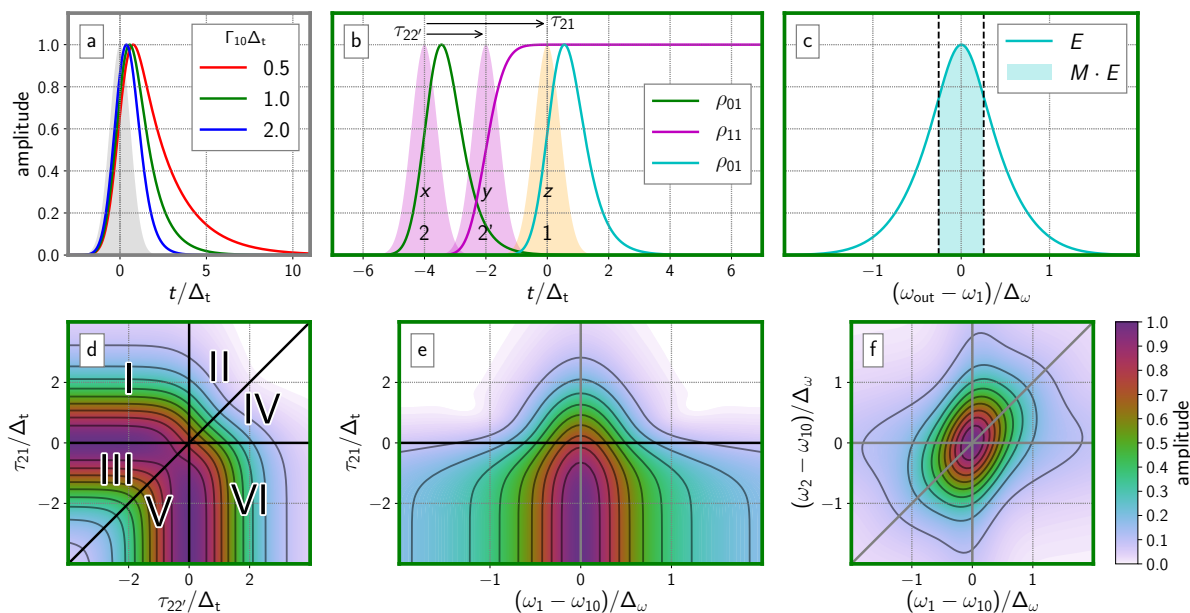


Figure 9.2: Overview of the MR-CMDS simulation. (a) The temporal profile of a coherence under pulsed excitation depends on how quickly the coherence dephases. In all subsequent panes, the relative dephasing rate is kept constant at  $\Gamma_{10}\Delta_t = 1$ . (b) Simulated evolution of the density matrix elements of a third-order Liouville pathway  $V\gamma$  under fully resonant excitation. Pulses can be labeled both by their time of arrival ( $x, y, z$ ) and by the lab lasers used to stimulate the transitions ( $2, 2', 1$ ). The final coherence (teal) creates the output electric field. (c) The frequency profile of the output electric field is filtered by a monochromator gating function,  $M(\omega)$ , and the passed components (shaded) are measured. (d-f) Signal is viewed against two laser parameters, either as 2D delay (d), mixed delay-frequency (e), or 2D frequency plots (f). The six time-orderings are labeled in (d) to help introduce our delay convention.

Fig. 9.2 gives an overview of the simulations done in this work. Fig. 9.2a shows an excitation pulse (gray-shaded) and examples of a coherent transient for three different dephasing rates. The color bindings to dephasing rates introduced in Fig. 9.2a will be used consistently throughout this work. Our simulations use systems with dephasing rates quantified relative to the pulse duration:  $\Gamma_{10}\Delta_t = 0.5, 1,$  or 2. The temporal axes are normalized to the pulse duration,  $\Delta_t$ . The  $\Gamma_{10}\Delta_t = 2$  transient is mostly driven by the excitation pulse while  $\Gamma_{10}\Delta_t = 0.5$  has a substantial free induction decay (FID) component at late times. Fig. 9.2b shows a pulse sequence (pulses are shaded orange and pink) and the resulting system evolution of pathway  $V\gamma$  ( $00 \xrightarrow{2} 01 \xrightarrow{2'} 11 \xrightarrow{1} 10 \xrightarrow{\text{out}} 00$ ) with  $\Gamma_{10}\Delta_t = 1$ . The final polarization (teal) is responsible for the emitted signal, which is then passed through a frequency bandpass filter to emulate monochromator detection (Fig. 9.2c). The resulting signal is explored in 2D delay space (Fig. 9.2d), 2D frequency space (Fig. 9.2f), and hybrid delay-frequency space (Fig. 9.2e). The detuning frequency axes are also normalized by the pulse bandwidth,  $\Delta_\omega$ .

We now consider the generalized Liouville pathway  $L : \rho_0 \xrightarrow{x} \rho_1 \xrightarrow{y} \rho_2 \xrightarrow{z} \rho_3 \xrightarrow{\text{out}} \rho_4$ , where  $x, y,$  and  $z$  denote properties of the first, second, and third pulse, respectively, and indices 0, 1, 2, 3, and 4 define the properties of the ground state, first, second, third, and fourth density matrix elements, respectively. Fig. 9.2b demonstrates the correspondence between  $x, y, z$  notation and 1, 2, 2' notation for the laser pulses with pathway  $V\gamma$ .

The electric field emitted from a Liouville pathway is proportional to the polarization created by the third-order coherence:

$$E_L(t) = i\mu_4\rho_3(t). \quad (9.6)$$

Equation 9.6 assumes perfect phase-matching and no pulse distortions through propagation. Equation 9.5 shows that the output field for this Liouville pathway is

$$E_L(t) = \frac{i}{8}\lambda_1\lambda_2\lambda_3\mu_1\mu_2\mu_3\mu_4 e^{i(\kappa_1\omega_x\tau_x + \kappa_2\omega_y\tau_y + \kappa_3\omega_z\tau_z)} e^{-i(\kappa_3\omega_z + \kappa_2\omega_y + \kappa_1\omega_x)t} \\ \times \int \int \int_{-\infty}^{\infty} c_z(t-u-\tau_z)c_y(t-u-v-\tau_y)c_x(t-u-v-w-\tau_x)R_L(u,v,w)dw dv du, \quad (9.7)$$

$$R_L(u,v,w) = \Theta(w)e^{-(\Gamma_1 + i\kappa_1\Omega_{1x})w}\Theta(v)e^{-(\Gamma_2 + i[\kappa_1\Omega_{1x} + \kappa_2\Omega_{2y}])v}\Theta(u)e^{-(\Gamma_3 + i[\kappa_1\Omega_{1x} + \kappa_2\Omega_{2y} + \kappa_3\Omega_{3z}])u}, \quad (9.8)$$



where  $R_L$  is the third-order response function for the Liouville pathway. The total electric field will be the superposition of all the Liouville pathways:

$$E_{\text{tot}} = \sum_L E_L(t). \quad (9.9)$$

For the superposition of Equation 9.9 to be non-canceling, certain symmetries between the pathways must be broken. In general, this requires one or more of the following inequalities:  $\Gamma_{10} \neq \Gamma_{21}$ ,  $\omega_{10} \neq \omega_{21}$ , and/or  $\sqrt{2}\mu_{10} \neq \mu_{21}$ . Our simulations use the last inequality, which is important in two-level systems ( $\mu_{21} = 0$ ) and in systems where state-filling dominates the non-linear response, such as in semiconductor excitons. The exact ratio between  $\mu_{10}$  and  $\mu_{21}$  affects the absolute amplitude of the field, but does not affect the multidimensional line shape. Importantly, the dipole inequality does not break the symmetry of double quantum coherence pathways (time-orderings II and IV), so such pathways are not present in our analysis.

In MR-CMDS, a monochromator resolves the driven output frequency from other nonlinear output frequencies, which in our case is  $\omega_m = \omega_1 - \omega_2 + \omega_{2'} = \omega_1$ . The monochromator can also enhance spectral resolution, as we show in Section 9.4.1. In this simulation, the detection is emulated by transforming  $E_{\text{tot}}(t)$  into the frequency domain, applying a narrow bandpass filter,  $M(\omega)$ , about  $\omega_1$ , and applying amplitude-scaled detection:

$$S_{\text{tot}}(\omega_1, \omega_2, \tau_{21}, \tau_{22'}) = \sqrt{\int |M(\omega - \omega_1)E_{\text{tot}}(\omega)|^2 d\omega}, \quad (9.10)$$

where  $E_{\text{tot}}(\omega)$  denotes the Fourier transform of  $E_{\text{tot}}(t)$  (see Fig. 9.2c). For  $M$  we used a rectangular function of width  $0.408\Delta_\omega$ . The arguments of  $S_{\text{tot}}$  refer to the *experimental* degrees of freedom. The signal delay dependence is parameterized with the relative delays  $\tau_{21}$  and  $\tau_{22'}$ , where  $\tau_{nm} = \tau_n - \tau_m$  (see Fig. 9.2b). Table S1 summarizes the arguments for each Liouville pathway. Fig. 9.2f shows the 2D  $(\omega_1, \omega_2)$   $S_{\text{tot}}$  spectrum resulting from the pulse delay times represented in Fig. 9.2b.

### 9.2.1 Inhomogeneity

Inhomogeneity is isolated in CMDS through both spectral signatures, such as line-narrowing [BesemannDanielM2004a, OudarJL1980a, CarlsonRogerJ1990a, RiebeMichaelT1988a, SteehlerJK1985a], and temporal signatures, such as photon echoes [WeinerAM1985a, AgarwalRitesh2002a]. We simulate the effects of static inhomogeneous broadening by convolving the homogeneous response with a Gaussian distribution function. Further details of the convolution are in Appendix ???. Dynamic broadening effects such as spectral diffusion are beyond the scope of this work.

## 9.3 Methods

A matrix representation of differential equations of the type in Equation 9.7 was numerically integrated for parallel computation of Liouville elements (see SI for details). [DickBernhard1983a, GelinMaximF2005a]

The lower bound of integration was  $2\Delta_t$  before the first pulse, and the upper bound was  $5\Gamma_{10}^{-1}$  after the last pulse, with step sizes much shorter than the pulse durations. Integration was performed in the FID rotating frame; the time steps were chosen so that both the system-pulse difference frequencies and the pulse envelope were well-sampled.

The following simulations explore the four-dimensional  $(\omega_1, \omega_2, \tau_{21}, \tau_{22'})$  variable space. Both frequencies are scanned about the resonance, and both delays are scanned about pulse overlap. We explored the role of sample dephasing rate by calculating signal for systems with dephasing rates such that  $\Gamma_{10}\Delta_t = 0.5, 1, \text{ and } 2$ . Inhomogeneous broadening used a spectral FWHM,  $\Delta_{\text{inhom}}$ , that satisfied  $\Delta_{\text{inhom}}/\Delta_\omega = 0, 0.5, 1, \text{ and } 2$  for the three dephasing rates. For all these dimensions, both  $\rho_3(t; \omega_1, \omega_2, \tau_{21}, \tau_{22'})$  and  $S_{\text{tot}}(\omega_1, \omega_2, \tau_{21}, \tau_{22'})$  are recorded for each unique Liouville pathway. Our simulations were done using the open-source SciPy library. [OliphantTravisE2007a]

### 9.3.1 Characteristics of Driven and Impulsive Response

The changes in the spectral line shapes described in this work are best understood by examining the driven/continuous wave (CW) and impulsive limits of Equations 9.5 and 9.7. The driven limit is achieved

when pulse durations are much longer than the response function dynamics:  $\Delta_t |\Gamma_f + i\kappa_f \Omega_{f_x}| \gg 1$ . In this limit, the system will adopt a steady state over excitation:  $d\rho/dt \approx 0$ . Neglecting phase factors, the driven solution to Equation 9.5 will be

$$\tilde{\rho}_f(t) = \frac{\lambda_f \mu_f}{2} \frac{c_x(t - \tau_x) e^{i\kappa_f \Omega_{f_x} t}}{\kappa_f \Omega_{f_x}} \tilde{\rho}_i(t). \quad (9.11)$$

The frequency and temporal envelope of the excitation pulse controls the coherence time evolution, and the relative amplitude and phase of the coherence is directly related to detuning from resonance.

The impulsive limit is achieved when the excitation pulses are much shorter than response function dynamics:  $\Delta_t |\Gamma_f + i\kappa_f \Omega_{f_x}| \ll 1$ . The full description of the temporal evolution has two separate expressions: one for times when the pulse is interacting with the system, and one for times after pulse interaction. Both expressions are important when describing CMDS experiments.

For times after the pulse interaction,  $t \gtrsim \tau_x + \Delta_t$ , the field-matter coupling is negligible. The evolution for these times, on resonance, is given by

$$\tilde{\rho}_f(t) = \frac{i\lambda_f \mu_f}{2} \tilde{\rho}_i(\tau_x) \int c_x(u) du e^{-\Gamma_f(t-\tau_x)}. \quad (9.12)$$

This is classic free induction decay (FID) evolution: the system evolves at its natural frequency and decays at rate  $\Gamma_f$ . It is important to note that, while this expression is explicitly derived from the impulsive limit, FID behavior is not exclusive to impulsive excitation, as we have defined it. A latent FID will form if the pulse vanishes at a fast rate relative to the system dynamics.

For evaluating times near pulse excitation,  $t \lesssim \tau_x + \Delta_t$ , we implement a Taylor expansion in the response function about zero:  $e^{-(\Gamma_f + i\kappa_f \Omega_{f_x})u} = 1 - (\Gamma_f + i\kappa_f \Omega_{f_x})u + \dots$ . Our impulsive criterion requires that a low order expansion will suffice; it is instructive to consider the result of the first order expansion of

Equation 9.5:

$$\begin{aligned}
\tilde{\rho}_f(t) = & \frac{i\lambda_f\mu_f}{2} e^{-i\kappa_f\omega_x\tau_x} e^{-i\kappa_f\Omega_{fx}t} \tilde{\rho}_i(\tau_x) \\
& \times \left[ (1 - (\Gamma_f + i\kappa_f\Omega_{fx})(t - \tau_x)) \int_{-\infty}^{t-\tau_x} c_x(u) du \right. \\
& \left. + (\Gamma_f + i\kappa_f\Omega_{fx}) \int_{-\infty}^{t-\tau_x} c_x(u) u du \right]. \tag{9.13}
\end{aligned}$$

During this time  $\tilde{\rho}_f$  builds up roughly according to the integration of the pulse envelope. The build-up is integrated because the pulse transfers energy before appreciable dephasing or detuning occurs. Contrary to the expectation of impulsive evolution, the evolution of  $\tilde{\rho}_f$  is explicitly affected by the pulse frequency, and the temporal profile evolves according to the pulse.

It is important to recognize that the impulsive limit is defined not only by having slow relaxation relative to the pulse duration, but also by small detuning relative to the pulse bandwidth (as is stated in the inequality). As detuning increases, the higher orders of the response function Taylor expansion will be needed to describe the rise time, and the driven limit of Equation 9.11 will become valid. The details of this build-up time can often be neglected in impulsive approximations because build-up contributions are often negligible in analysis; the period over which the initial excitation occurs is small in comparison to the free evolution of the system. The build-up behavior can be emphasized by the measurement, which makes Equation 9.13 important.

We now consider full Liouville pathways in the impulsive and driven limits of Equation 9.7. For the driven limit, Equation 9.7 can be reduced to

$$\begin{aligned}
E_L(t) = & \frac{1}{8} \lambda_1 \lambda_2 \lambda_3 \mu_1 \mu_2 \mu_3 \mu_4 e^{-i(\kappa_1\omega_x\tau_x + \kappa_2\omega_y\tau_y + \kappa_3\omega_z\tau_z)} \\
& \times e^{i(\kappa_3\omega_z + \kappa_2\omega_y + \kappa_1\omega_x)t} \\
& \times c_z(t - \tau_z) c_y(t - \tau_y) c_x(t - \tau_x) \\
& \times \frac{1}{\kappa_1\Omega_{1x} - i\Gamma_1} \frac{1}{\kappa_1\Omega_{1x} + \kappa_2\Omega_{2y} - i\Gamma_2} \\
& \times \frac{1}{\kappa_1\Omega_{1x} + \kappa_2\Omega_{2y} + \kappa_3\Omega_{3z} - i\Gamma_3}. \tag{9.14}
\end{aligned}$$

It is important to note that the signal depends on the multiplication of all the fields; pathway discrimina-

tion based on pulse time-ordering is not achievable because polarizations exists only when all pulses are overlapped. This limit is the basis for frequency-domain techniques. Frequency axes, however, are not independent because the system is forced to the laser frequency and influences the resonance criterion for subsequent excitations. As an example, observe that the first two resonant terms in Equation 9.14 are maximized when  $\omega_x = |\omega_1|$  and  $\omega_y = |\omega_2|$ . If  $\omega_x$  is detuned by some value  $\varepsilon$ , however, the occurrence of the second resonance shifts to  $\omega_y = |\omega_2| + \varepsilon$ , effectively compensating for the  $\omega_x$  detuning. This shifting of the resonance results in 2D line shape correlations.

If the pulses do not temporally overlap ( $\tau_x + \Delta_t \lesssim \tau_y + \Delta_t \lesssim \tau_z + \Delta_t \lesssim t$ ), then the impulsive solution to the full Liouville pathway of Equation 9.7 is

$$\begin{aligned}
 E_L(t) &= \frac{i}{8} \lambda_1 \lambda_2 \lambda_3 \mu_1 \mu_2 \mu_3 \mu_4 e^{i(\omega_1 + \omega_2 + \omega_3)t} \\
 &\quad \times \int c_x(w) dw \int c_y(v) dv \int c_z(u) du \\
 &\quad \times e^{-\Gamma_1(\tau_y - \tau_x)} e^{-\Gamma_2(\tau_z - \tau_y)} e^{-\Gamma(t - \tau_z)}.
 \end{aligned} \tag{9.15}$$

Pathway discrimination is demonstrated here because the signal is sensitive to the time-ordering of the pulses. This limit is suited for delay scanning techniques. The emitted signal frequency is determined by the system and can be resolved by scanning a monochromator.

The driven and impulsive limits can qualitatively describe our simulated signals at certain frequency and delay combinations. Of the three expressions, the FID limit most resembles signal when pulses are near resonance and well-separated in time (so that build-up behavior is negligible). The build-up limit approximates well when pulses are near-resonant and arrive together (so that build-up behavior is emphasized). The driven limit holds for large detunings, regardless of delay.

### 9.3.2 Convolution Technique for Inhomogeneous Broadening

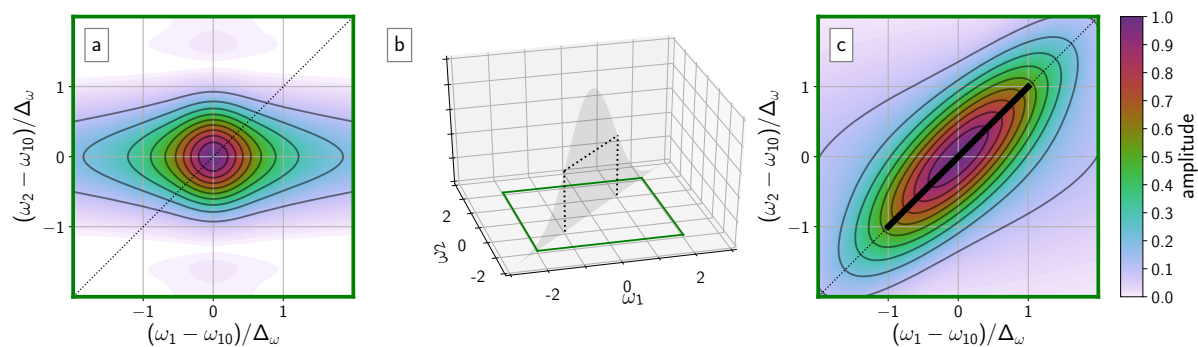


Figure 9.3: Overview of the convolution. (a) The homogeneous line shape. (b) The distribution function,  $K$ , mapped onto laser coordinates. (c) The resulting ensemble line shape computed from the convolution. The thick black line represents the FWHM of the distribution function.

Here we describe how to transform the data of a single reference oscillator signal to that of an inhomogeneous distribution. The oscillators in the distribution are allowed have arbitrary energies for their states, which will cause frequency shifts in the resonances. To show this, we start with a modified, but equivalent, form of Equation 9.4:

$$\begin{aligned} \frac{d\tilde{\rho}_f}{dt} = & -\Gamma_f \tilde{\rho}_f + \frac{i}{2} \lambda_f \mu_f c_x (t - \tau_x) \\ & \times e^{i\kappa_f(\vec{k} \cdot \mathbf{z} + \omega_x \tau_x)} e^{-i\kappa_f(\omega_x - |\omega_f|)t} \tilde{\rho}_i(t). \end{aligned} \quad (9.16)$$

We consider two oscillators with transition frequencies  $\omega_f$  and  $\omega'_f = \omega_f + \delta$ . So long as  $|\delta| \leq \omega_f$  (so that  $|\omega_f + \delta| = |\omega_f| + \delta$  and thus the rotating wave approximation does not change), Equation 9.16 shows that the two are related by

$$\frac{d\tilde{\rho}'_f}{dt}(t; \omega_x) = \frac{d\tilde{\rho}_f}{dt}(t; \omega_x - \delta) e^{i\kappa_f \delta \tau_x}. \quad (9.17)$$

Because both coherences are assumed to have the same initial conditions ( $\rho_0(-\infty) = \rho'_0(-\infty) = 0$ ), the equality also holds when both sides of the equation are integrated. The phase factor  $e^{i\kappa_f \delta \tau_x}$  in the substitution arises from Equation 9.1, where the pulse carrier frequency maintains its phase within the pulse envelope for all delays.

The resonance translation can be extended to higher order signals as well. For a third-order signal, we compare systems with transition frequencies  $\omega'_{10} = \omega_{10} + a$  and  $\omega'_{21} = \omega_{21} + b$ . The extension of Equation 9.17 to pathway  $V\beta$  gives

$$\begin{aligned} \tilde{\rho}'_3(t; \omega_2, \omega'_2, \omega_1) = & \tilde{\rho}_3(t; \omega_2 - a, \omega'_2 - a, \omega_1 - b) \\ & \times e^{i\kappa_2 a \tau_2} e^{i\kappa_2' a \tau_2'} e^{i\kappa_1 b \tau_1}. \end{aligned} \quad (9.18)$$

The translation of each laser coordinate depends on which transition is made (e.g.  $a$  for transitions between  $|0\rangle$  and  $|1\rangle$  or  $b$  for transitions between  $|1\rangle$  and  $|2\rangle$ ), so the exact translation relation differs between pathways. We can now compute the ensemble average of signal for pathway  $V\beta$  as a convolution

between the distribution function of the system,  $K(a, b)$ , and the single oscillator response:

$$\begin{aligned} \langle \tilde{\rho}_3(t; \omega_2, \omega_{2'}, \omega_1) \rangle &= \iint K(a, b) \\ &\times \tilde{\rho}_3(t; \omega_2 + a, \omega_{2'} + a, \omega_1 + b) \\ &\times e^{i\kappa_2 a \tau_2} e^{i\kappa_{2'} a \tau_{2'}} e^{i\kappa_1 b \tau_1} da db. \end{aligned} \quad (9.19)$$

For this work, we restrict ourselves to a simpler ensemble where all oscillators have equally spaced levels (i.e.  $a = b$ ). This makes the translation identical for all pathways and reduces the dimensionality of the convolution. Since pathways follow the same convolution we may also perform the convolution on the total signal field:

$$\begin{aligned} \langle E_{\text{tot}}(t) \rangle &= \sum_L \mu_{4,L} \int K(a, a) \\ &\times \tilde{\rho}_{3,L}(t; \omega_x - a, \omega_y - a, \omega_z - a) \\ &\times e^{ia(\kappa_x \tau_x + \kappa_y \tau_y + \kappa_z \tau_z)} da. \end{aligned} \quad (9.20)$$

Furthermore, since  $\kappa = -1$  for  $E_1$  and  $E_{2'}$ , while  $\kappa = 1$  for  $E_2$ , we have  $e^{ia(\kappa_x \tau_x + \kappa_y \tau_y + \kappa_z \tau_z)} = e^{-ia(\tau_1 - \tau_2 + \tau_{2'})}$  for all pathways. Equivalently, if the electric field is parameterized in terms of laser coordinates  $\omega_1$  and  $\omega_2$ , the ensemble field can be calculated as

$$\begin{aligned} \langle E_{\text{tot}}(t; \omega_1, \omega_2) \rangle &= \int K(a, a) E_{\text{tot}}(t; \omega_1 - a, \omega_2 - a) \\ &\times e^{-ia(\tau_1 - \tau_2 + \tau_{2'})} da. \end{aligned} \quad (9.21)$$

which is a 1D convolution along the diagonal axis in frequency space. Fig. 9.3 demonstrates the use of Equation 9.21 on a homogeneous line shape.

## 9.4 Results

We now present portions of our simulated data that highlight the dependence of the spectral line shapes and transients on excitation pulse width, the dephasing rate, detuning from resonance, the pulse delay times, and inhomogeneous broadening.



### 9.4.1 Evolution of single coherence

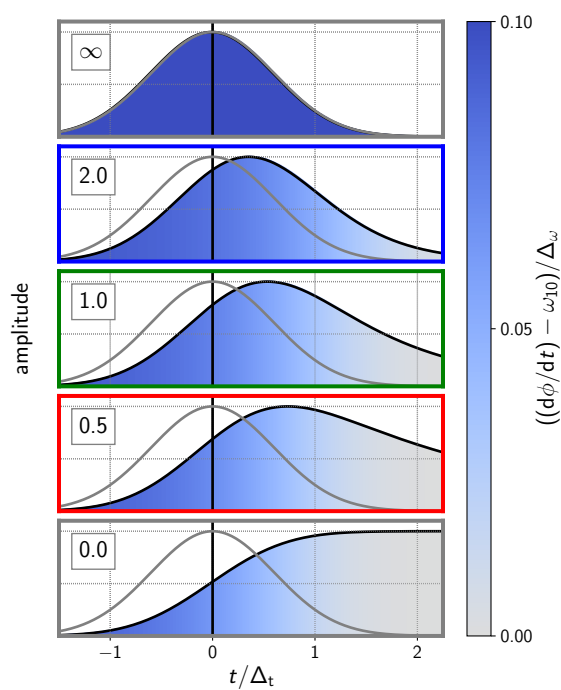


Figure 9.4: The relative importance of FID and driven response for a single quantum coherence as a function of the relative dephasing rate (values of  $\Gamma_{10}\Delta_t$  are shown inset). The black line shows the coherence amplitude profile, while the shaded color indicates the instantaneous frequency (see colorbar). For all cases, the pulsed excitation field (gray line, shown as electric field amplitude) is slightly detuned (relative detuning,  $\Omega_{fx}/\Delta\omega = 0.1$ ).

It is illustrative to first consider the evolution of single coherences,  $\rho_0 \xrightarrow{x} \rho_1$ , under various excitation conditions. Fig. 9.4 shows the temporal evolution of  $\rho_1$  with various dephasing rates under Gaussian excitation. The value of  $\rho_1$  differs only by phase factors between various Liouville pathways (this can be verified by inspection of Equation 9.5 under the various conditions in Table S1), so the profiles in Fig. 9.4 apply for the first interaction of any pathway. The pulse frequency was detuned from resonance so that frequency changes could be visualized by the color bar, but the detuning was kept slight so that it did not appreciably change the dimensionless product,  $\Delta_t (\Gamma_f + ik_f \Omega_{fx}) \approx \Gamma_{10} \Delta_t$ . In this case, the evolution demonstrates the maximum impulsive character the transient can achieve. The instantaneous frequency,  $d\varphi/dt$ , is defined as

$$\frac{d\varphi}{dt} = \frac{d}{dt} \tan^{-1} \left( \frac{\text{Im}(\rho_1(t))}{\text{Re}(\rho_1(t))} \right). \quad (9.22)$$

The cases of  $\Gamma_{10} \Delta_t = 0(\infty)$  agree with the impulsive (driven) expressions derived in Appendix 9.3.1. For  $\Gamma_{10} \Delta_t = 0$ , the signal rises as the integral of the pulse and has instantaneous frequency close to that of the pulse (Equation 9.13), but as the pulse vanishes, the signal adopts the natural system frequency and decay rate (Equation 9.12). For  $\Gamma_{10} \Delta_t = \infty$ , the signal follows the amplitude and frequency of the pulse for all times (the driven limit, Equation 9.11).

The other three cases show a smooth interpolation between limits. As  $\Gamma_{10} \Delta_t$  increases from the impulsive limit, the coherence within the pulse region conforms less to a pulse integral profile and more to a pulse envelope profile. In accordance, the FID component after the pulse becomes less prominent, and the instantaneous frequency pins to the driving frequency more strongly through the course of evolution. The trends can be understood by considering the differential form of evolution (Equation 9.4), and the time-dependent balance of optical coupling and system relaxation. We note that our choices of  $\Gamma_{10} \Delta_t = 2.0, 1.0$ , and  $0.5$  give coherences that have mainly driven, roughly equal driven and FID parts, and mainly FID components, respectively. FID character is difficult to isolate when  $\Gamma_{10} \Delta_t = 2.0$ .

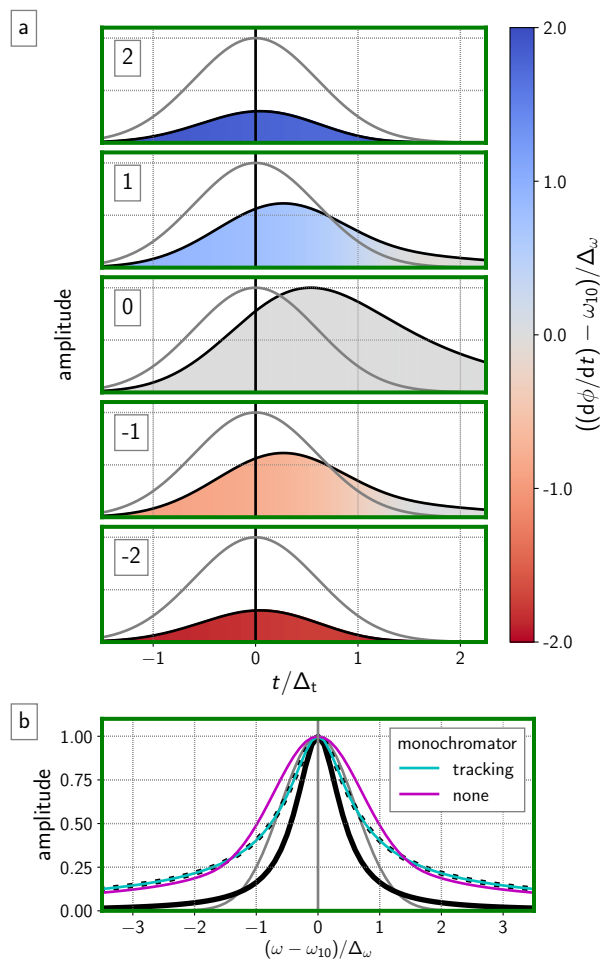


Figure 9.5: Pulsed excitation of a single quantum coherence and its dependence on the pulse detuning. In all cases, relative dephasing is kept at  $\Gamma_{10}\Delta_t = 1$ . (a) The relative importance of FID and driven response for a single quantum coherence as a function of the detuning (values of relative detuning,  $\Omega_{fx}/\Delta_\omega$ , are shown inset). The color indicates the instantaneous frequency (scale bar on right), while the black line shows the amplitude profile. The gray line is the electric field amplitude. (b) The time-integrated coherence amplitude as a function of the detuning. The integrated amplitude is collected both with (teal) and without (magenta) a tracking monochromator that isolates the driven frequency components. For comparison, the Green's function of the single quantum coherence is also shown (amplitude is black, hashed; imaginary is black, solid). In all plots, the gray line is the electric field amplitude.

Fig. 9.5a shows the temporal evolution of  $\rho_1$  at several values of  $\Omega_{1x}/\Delta_\omega$  with  $\Gamma_{10}\Delta_t = 1$ .

As detuning increases, total amplitude decreases, FID character vanishes, and  $\rho_1$  assumes a more driven character, as expected. During the excitation,  $\rho_1$  maintains a phase relationship with the input field (as seen by the instantaneous frequency in Fig. 9.5a). The coherence will persist beyond the pulse duration only if the pulse transfers energy into the system; FID evolution equates to absorption. The FID is therefore sensitive to the absorptive (imaginary) line shape of a transition, while the driven response is the composite of both absorptive and dispersive components. If the experiment isolates the latent FID response, there is consequently a narrower spectral response. This spectral narrowing can be seen in Fig. 9.5a by comparing the coherence amplitudes at  $t = 0$  (driven) and at  $t/\Delta_t = 2$  (FID); amplitudes for all  $\Omega_{fx}/\Delta_\omega$  values shown are comparable at  $t = 0$ , but the lack of FID formation for  $\Omega_{fx}/\Delta_\omega = \pm 2$  manifests as a visibly disproportionate amplitude decay. Many ultrafast spectroscopies take advantage of the latent FID to suppress non-resonant background, improving signal to noise. [**LagutchevAlexi2007a, LagutchevAlexi2010a, DonaldsonPaulMurray2010a, DonaldsonPaulMurray2008a**]

In driven experiments, the output frequency and line shape are fully constrained by the excitation beams. In such experiments, there is no additional information to be resolved in the output spectrum. The situation changes in the mixed domain, where  $E_{\text{tot}}$  contains FID signal that lasts longer than the pulse duration. Fig. 9.5a provides insight on how frequency-resolved detection of coherent output can enhance resolution when pulses are spectrally broad. Without frequency-resolved detection, mixed-domain resonance enhancement occurs in two ways: (1) the peak amplitude increases, and (2) the coherence duration increases due to the FID transient. Frequency-resolved detection can further discriminate against detuning by requiring that the driving frequency agrees with latent FID. The implications of discrimination are most easily seen in Fig. 9.5a with  $\Omega_{1x}/\Delta_\omega = \pm 1$ , where the system frequency moves from the driving frequency to the FID frequency. When the excitation pulse frequency is scanned, the resonance will be more sensitive to detuning by isolating the driven frequency (tracking the monochromator with the excitation source).

The functional form of the measured line shape can be deduced by considering the frequency domain

form of Equation 9.5 (assume  $\rho_i = 1$  and  $\tau_x = 0$ ):

$$\tilde{\rho}_f(\omega) = \frac{i\lambda_f\mu_f}{2\sqrt{2\pi}} \cdot \frac{\mathcal{F}\{c_x\}(\omega - \kappa_f\Omega_{fx})}{\Gamma_f + i\omega}, \quad (9.23)$$

where  $\mathcal{F}\{c_x\}(\omega)$  denotes the Fourier transform of  $c_x$ , which in our case gives

$$\mathcal{F}\{c_x\}(\omega) = \frac{1}{\sqrt{2\pi}} e^{-\frac{(\Delta_f\omega)^2}{4\ln^2}}. \quad (9.24)$$

For squared-law detection of  $\rho_f$ , the importance of the tracking monochromator is highlighted by two limits of Equation 9.23:

- When the transient is not frequency resolved,  $\text{sig} \approx \int |\tilde{\rho}_f(\omega)|^2 d\omega$  and the measured line shape will be the convolution of the pulse envelope and the intrinsic (Green's function) response (Fig. 9.5b, magenta).
- When the driven frequency is isolated,  $\text{sig} \approx |\tilde{\rho}_f(\kappa_f\Omega_{fx})|^2$  and the measured line shape will give the un-broadened Green's function (Fig. 9.5b, teal).

Monochromatic detection can remove broadening effects due to the pulse bandwidth. For large  $\Gamma_{10}\Delta_t$  values, FID evolution is negligible at all  $\Omega_{fx}/\Delta_\omega$  values and the monochromator is not useful. Fig. 9.5b shows the various detection methods for the relative dephasing rate of  $\Gamma_{10}\Delta_t = 1$ .

#### 9.4.2 Evolution of single Liouville pathway

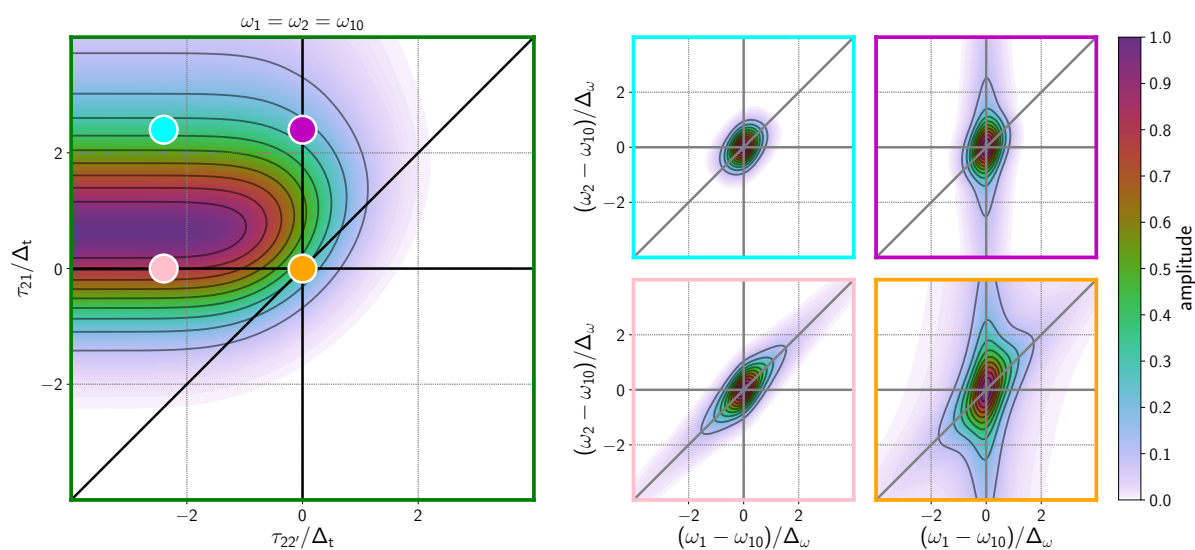


Figure 9.6: Changes to the 2D frequency response of a single Liouville pathway ( $I_\gamma$ ) at different delay values. The normalized dephasing rate is  $\Gamma_{10}\Delta_t = 1$ . Left: The 2D delay response of pathway  $I_\gamma$  at triple resonance. Right: The 2D frequency response of pathway  $I_\gamma$  at different delay values. The delays at which the 2D frequency plots are collected are indicated on the delay plot; compare 2D spectrum frame color with dot color on 2D delay plot.

We now consider the multidimensional response of a single Liouville pathway involving three pulse interactions. In a multi-pulse experiment,  $\rho_1$  acts as a source term for  $\rho_2$  (and subsequent excitations). The spectral and temporal features of  $\rho_1$  that are transferred to  $\rho_2$  depend on when the subsequent pulse arrives. Time-gating later in  $\rho_1$  evolution will produce responses with FID behavior, while time-gating  $\rho_1$  in the presence of the initial pulse will produce driven responses. An analogous relationship holds for  $\rho_3$  with its source term  $\rho_2$ . As discussed above, signal that time-gates FID evolution gives narrower spectra than driven-gated signal. As a result, the spectra of even single Liouville pathways will change based on pulse delays.

The final coherence will also be frequency-gated by the monochromator. The monochromator isolates signal at the fully driven frequency  $\omega_{\text{out}} = \omega_1$ . The monochromator will induce line-narrowing to the extent that FID takes place. It effectively enforces a frequency constraint that acts as an additional resonance condition,  $\omega_{\text{out}} = \omega_1$ . The driven frequency will be  $\omega_1$  if  $E_1$  is the last pulse interaction (time-orderings V and VI), and the monochromator tracks the coherence frequency effectively. If  $E_1$  is not the last interaction, the output frequency may not be equal to the driven frequency, and the monochromator plays a more complex role.

We demonstrate this delay dependence using the multidimensional response of the  $l\gamma$  Liouville pathway as an example (see Fig. 9.1). Fig. 9.6 shows the resulting 2D delay profile of pathway  $l\gamma$  signals for  $\Gamma_{10}\Delta_t = 1$  (left) and the corresponding  $\omega_1, \omega_2$  2D spectra at several pulse delay values (right). The spectral changes result from changes in the relative importance of driven and FID components. The prominence of FID signal can change the resonance conditions; Table 9.1 summarizes the changing resonance conditions for each of the four delay coordinates studied. Since  $E_1$  is not the last pulse in pathway  $l\gamma$ , the tracking monochromator must also be considered.



Table 9.1: Conditions for peak intensity at different pulse delays for pathway I $\gamma$ .

Delay		Approximate Resonance Conditions			
$\tau_{21}/\Delta_t$	$\tau_{22'}/\Delta_t$	$\rho_0 \xrightarrow{1} \rho_1$	$\rho_1 \xrightarrow{2} \rho_2$	$\rho_2 \xrightarrow{2'} \rho_3$	$\rho_3 \rightarrow \text{detection at } \omega_m = \omega_1$
0	0	$\omega_1 = \omega_{10}$	$\omega_1 = \omega_2$	$\omega_1 = \omega_{10}$	–
0	-2.4	$\omega_1 = \omega_{10}$	$\omega_1 = \omega_2$	$\omega_2 = \omega_{10}$	$\omega_1 = \omega_2$
2.4	0	$\omega_1 = \omega_{10}$	$\omega_2 = \omega_{10}$	–	$\omega_1 = \omega_{10}$
2.4	-2.4	$\omega_1 = \omega_{10}$	$\omega_2 = \omega_{10}$	$\omega_2 = \omega_{10}$	$\omega_1 = \omega_2$

When the pulses are all overlapped ( $\tau_{21} = \tau_{22'} = 0$ , lower right, orange), all transitions in the Liouville pathway are simultaneously driven by the incident fields. This spectrum strongly resembles the driven limit spectrum. For this time-ordering, the first, second, and third density matrix elements have driven resonance conditions of  $\omega_1 = \omega_{10}$ ,  $\omega_1 - \omega_2 = 0$ , and  $\omega_1 - \omega_2 + \omega_{2'} = \omega_{10}$ , respectively. The second resonance condition causes elongation along the diagonal, and since  $\omega_2 = \omega_{2'}$ , the first and third resonance conditions are identical, effectively making  $\omega_1$  doubly resonant at  $\omega_{10}$  and resulting in the vertical elongation along  $\omega_1 = \omega_{10}$ .

The other three spectra of Fig. 9.6 separate the pulse sequence over time so that not all interactions are driven. At  $\tau_{21} = 0$ ,  $\tau_{22'} = -2.4\Delta_t$  (lower left, pink), the first two resonances remain the same as at pulse overlap (orange) but the last resonance is different. The final pulse,  $E_{2'}$ , is latent and probes  $\rho_2$  during its FID evolution after memory of the driven frequency is lost. There are two important consequences. Firstly, the third driven resonance condition is now approximated by  $\omega_{2'} = \omega_{10}$ , which makes  $\omega_1$  only singly resonant at  $\omega_1 = \omega_{10}$ . Secondly, the driven portion of the signal frequency is determined only by the latent pulse:  $\omega_{\text{out}} = \omega_{2'}$ . Since our monochromator gates  $\omega_1$ , we have the detection-induced correlation  $\omega_1 = \omega_{2'}$ . The net result is double resonance along  $\omega_1 = \omega_2$ , and the vertical elongation of pulse overlap is strongly attenuated.

At  $\tau_{21} = 2.4\Delta_t$ ,  $\tau_{22'} = 0$  (upper right, purple), the first pulse  $E_1$  precedes the latter two, which makes the two resonance conditions for the input fields  $\omega_1 = \omega_{10}$  and  $\omega_2 = \omega_{10}$ . The signal depends on the FID conversion of  $\rho_1$ , which gives vertical elongation at  $\omega_1 = \omega_{10}$ . Furthermore,  $\rho_1$  has no memory of  $\omega_1$  when  $E_2$  interacts, which has two important implications. First, this means the second resonance condition  $\omega_1 = \omega_2$  and the associated diagonal elongation is now absent. Second, the final output polarization frequency content is no longer functional of  $\omega_1$ . Coupled with the fact that  $E_2$  and  $E_{2'}$  are coincident, so that the final coherence can be approximated as driven by these two, we can approximate the final frequency as  $\omega_{\text{out}} = \omega_{10} - \omega_2 + \omega_{2'} = \omega_{10}$ . Surprisingly, the frequency content of the output is strongly independent of all pulse frequencies. The monochromator narrows the  $\omega_1 = \omega_{10}$  resonance. The  $\omega_1 = \omega_{10}$  resonance condition now depends on the monochromator slit width, the FID propagation of  $\rho_1$ , the spectral bandwidth of  $\rho_3$ ; its spectral width is not easily related to material parameters. This resonance demonstrates the importance of the detection scheme for experiments and how the optimal detection can change depending on the pulse delay time.

Finally, when all pulses are well-separated ( $\tau_{21} = -\tau_{22'} = 2.4\Delta_t$ , upper left, cyan), each resonance condition is independent and both  $E_1$  and  $E_2$  require FID buildup to produce final output. The resulting line shape is narrow in all directions. Again, the emitted frequency does not depend on  $\omega_1$ , yet the monochromator resolves the final coherence at frequency  $\omega_1$ . Since the driven part of the final interaction comes from  $E_{2'}$ , and since the monochromator track  $\omega_1$ , the output signal will increase when  $\omega_1 = \omega_{2'}$ . As a result, the line shape acquires a diagonal character.

The changes in line shape seen in Fig. 9.6 have significant ramifications for the interpretations and strategies of MR-CMDS in the mixed domain. Time-gating has been used to isolate the 2D spectra of a certain time-ordering [MeyerKentA2004a, PakoulevAndreiV2006a, DonaldsonPaulMurray2007b], but here we show that time-gating itself causes significant line shape changes to the isolated pathways. The phenomenon of time-gating can cause frequency and delay axes to become functional of each other in unexpected ways.

### 9.4.3 Temporal pathway discrimination

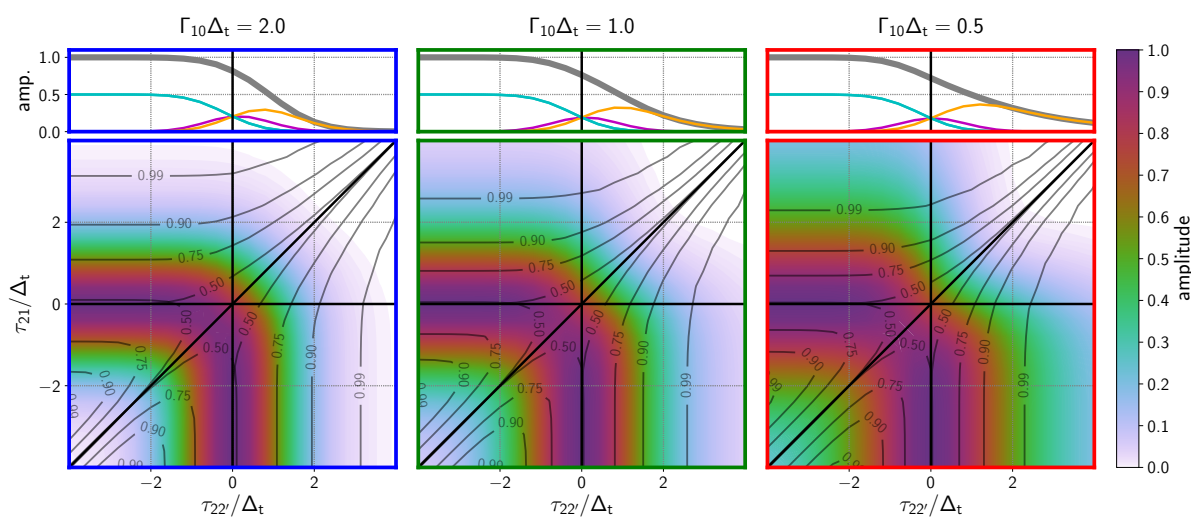


Figure 9.7: Comparison of the 2D delay response for different relative dephasing rates (labeled atop each column). All pulses are tuned to exact resonance. In each 2D delay plot, the signal amplitude is depicted by the colors. The black contour lines show signal purity,  $P$  (see Equation 9.25), with purity values denoted on each contour. The small plots above each 2D delay plot examine a  $\tau_{22}'$  slice of the delay response ( $\tau_{21} = 0$ ). The plot shows the total signal (black), as well as the component time-orderings VI (orange), V (purple), and III or I (teal).

In the last section we showed how a single pathway's spectra can evolve with delay due to pulse effects and time gating. In real experiments, evolution with delay is further complicated by the six time-orderings/sixteen pathways present in our three-beam experiment (see Fig. 9.1). Each time-ordering has different resonance conditions. When signal is collected near pulse overlap, multiple time-orderings contribute. To identify these effects, we start by considering how strongly time-orderings are isolated at each delay coordinate.

While the general idea of using time delays to enhance certain time-ordered regions is widely applied, quantitation of this discrimination is rarely explored. Because the temporal profile of the signal is dependent on both the excitation pulse profile and the decay dynamics of the coherence itself, quantitation of pathway discrimination requires simulation.

Fig. 9.7 shows the 2D delay space with all pathways present for  $\omega_1, \omega_2 = \omega_{10}$ . It illustrates the interplay of pulse width and system decay rates on the isolation of time-ordered pathways. The color bar shows the signal amplitude. Signal is symmetric about the  $\tau_{21} = \tau_{22'}$  line because when  $\omega_1 = \omega_2$ ,  $E_1$  and  $E_{2'}$  interactions are interchangeable:  $S_{\text{tot}}(\tau_{21}, \tau_{22'}) = S_{\text{tot}}(\tau_{22'}, \tau_{21})$ . The overlaid black contours represent signal "purity,"  $P$ , defined as the relative amount of signal that comes from the dominant pathway at that delay value:

$$P(\tau_{21}, \tau_{22'}) = \frac{\max\{S_L(\tau_{21}, \tau_{22'})\}}{\sum_L S_L(\tau_{21}, \tau_{22'})}. \quad (9.25)$$

The dominant pathway ( $\max\{S_L(\tau_{21}, \tau_{22'})\}$ ) at given delays can be inferred by the time-ordered region defined in Fig. 9.2d. The contours of purity generally run parallel to the time-ordering boundaries with the exception of time-ordered regions II and IV, which involve the double quantum coherences that have been neglected.

A commonly-employed metric for temporal selectivity is how definitively the pulses are ordered. This metric agrees with our simulations. The purity contours have a weak dependence on  $\Delta_t \Gamma_{10}$  for  $|\tau_{22'}|/\Delta_t < 1$  or  $|\tau_{21}|/\Delta_t < 1$  where there is significant pathway overlap and a stronger dependence at larger values where the pathways are well-isolated. Because responses decay exponentially, while pulses decay as Gaussians, there always exist delays where temporal discrimination is possible. As  $\Delta_t \Gamma_{10} \rightarrow \infty$ , however, such discrimination is only achieved at vanishing signal intensities; the contour of  $P = 0.99$  across our systems highlights this trend.

#### 9.4.4 Multidimensional line shape dependence on pulse delay time

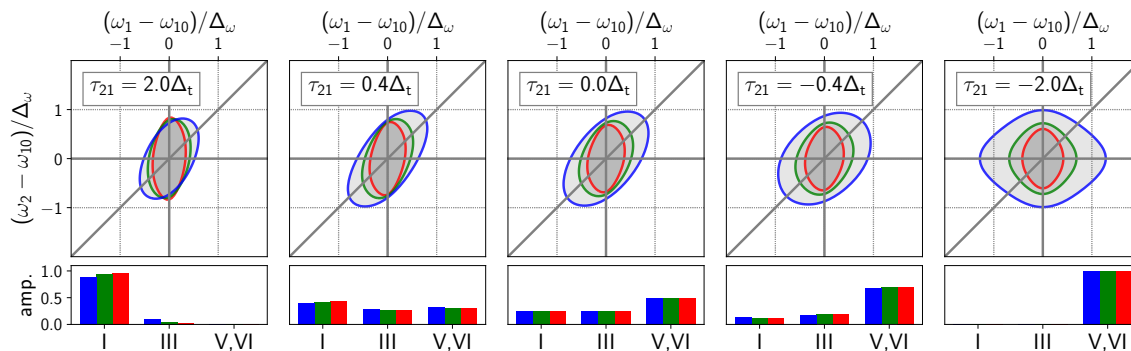


Figure 9.8: Evolution of the 2D frequency response as a function of  $\tau_{21}$  (labeled inset) and the influence of the relative dephasing rate ( $\Gamma_{10}\Delta_t = 0.5$  (red), 1.0 (green), and 2.0 (blue)). In all plots  $\tau_{22'} = 0$ . To ease comparison between different dephasing rates, the colored line contours (showing the half-maximum) for all three relative dephasing rates are overlaid. The colored histograms below each 2D frequency plot show the relative weights of each time-ordering for each relative dephasing rate. Contributions from V and VI are grouped together because they have equal weights at  $\tau_{22'} = 0$ .

In the previous sections we showed how pathway spectra and weights evolve with delay. This section ties the two concepts together by exploring the evolution of the spectral line shape over a span of  $\tau_{21}$  delay times that include all pathways. It is a common practice to explore spectral evolution against  $\tau_{21}$  because this delay axis shows population evolution in a manner analogous to pump-probe spectroscopies. The  $\vec{k}_2$  and  $\vec{k}_2'$  interactions correspond to the pump, and the  $\vec{k}_1$  interaction corresponds to the probe. Time-orderings V and VI are the normal pump-probe time-orderings, time-ordering III is a mixed pump-probe-pump ordering (so-called pump polarization coupling), and time-ordering I is the probe-pump ordering (so-called perturbed FID). Scanning  $\tau_{21}$  through pulse overlap complicates interpretation of the line shape due to the changing nature and balance of the contributing time-orderings. At  $\tau_{21} > 0$ , time-ordering I dominates; at  $\tau_{21} = 0$ , all time-orderings contribute equally; at  $\tau_{21} < 0$  time-orderings V and VI dominate (Fig. 9.7). Conventional pump-probe techniques recognized these complications long ago, [BritoCruzCH1988a, PalfreySL1985a] but the extension of these effects to MR-CMDS has not previously been done.

Fig. 9.8 shows the MR-CMDS spectra, as well as histograms of the pathway weights, while scanning  $\tau_{21}$  through pulse overlap. The colored histogram bars and line shape contours correspond to different values of the relative dephasing rate,  $\Gamma_{10}\Delta_t$ . The contour is the half-maximum of the line shape. The dependence of the line shape amplitude on  $\tau_{21}$  can be inferred from Fig. 9.7.

The qualitative trend, as  $\tau_{21}$  goes from positive to negative delays, is a change from diagonal/compressed line shapes to much broader resonances with no correlation ( $\omega_1$  and  $\omega_2$  interact with independent resonances). Such spectral changes could be misinterpreted as spectral diffusion, where the line shape changes from correlated to uncorrelated as population time increases due to system dynamics. The system dynamics included here, however, contain no structure that would allow for such diffusion. Rather, the spectral changes reflect the changes in the majority pathway contribution, starting with time-ordering I pathways, proceeding to an equal admixture of I, III, V, and VI, and finishing at an equal balance of V and VI when  $E_1$  arrives well after  $E_2$  and  $E_2'$ . Time-orderings I and III both exhibit a spectral correlation in  $\omega_1$  and  $\omega_2$  when driven, but time-orderings V and VI do not. Moreover, such spectral correlation is forced near zero delay because the pulses time-gate the driven signals of the first two induced polarizations. The monochromator detection also plays a dynamic role, because time-orderings V always VI always emit a signal at the monochromator frequency, while in time-orderings I



and III the emitted frequency is not defined by  $\omega_1$ , as discussed above.

When we isolate time-orderings V and VI, we can maintain the proper scaling of FID bandwidth in the  $\omega_1$  direction because our monochromator can gate the final coherence. This gating is not possible in time-orderings I and III because the final coherence frequency is determined by  $\omega_2$ , which is identical to  $\omega_2$ .

There are differences in the line shapes for the different values of the relative dephasing rate,  $\Gamma_{10}\Delta_t$ . The spectral correlation at  $\tau_{21}/\Delta_t = 2$  decreases in strength as  $\Gamma_{10}\Delta_t$  decreases. As we illustrated in Fig. 9.6, this spectral correlation is a signature of driven signal from temporal overlap of  $E_1$  and  $E_2$ ; the loss of spectral correlation reflects the increased prominence of FID in the first coherence as the field-matter interactions become more impulsive. This increased prominence of FID also reflects an increase in signal strength, as shown by  $\tau_{21}$  traces in Fig. 9.7. When all pulses are completely overlapped, ( $\tau_{21} = 0$ ), each of the line shapes exhibit spectral correlation. At  $\tau_{21}/\Delta_t = -2$ , the line shape shrinks as  $\Gamma_{10}\Delta_t$  decreases, with the elongation direction changing from horizontal to vertical. The general shrinking reflects the narrowing homogeneous linewidth of the  $\omega_{10}$  resonance. In all cases, the horizontal line shape corresponds to the homogeneous linewidth because the narrow bandpass monochromator resolves the final  $\omega_1$  resonance. The change in elongation direction is due to the resolving power of  $\omega_2$ . At  $\Gamma_{10}\Delta_t = 0.5$ , the resonance is broader than our pulse bandwidth and is fully resolved vertically. It is narrower than the  $\omega_1$  resonance because time-orderings V and VI interfere to isolate only the absorptive line shape along  $\omega_2$ . This narrowing, however, is unresolvable when the pulse bandwidth becomes broader than that of the resonance, which gives rise to a vertically elongated signal when  $\Gamma_{10}\Delta_t = 0.5$ .

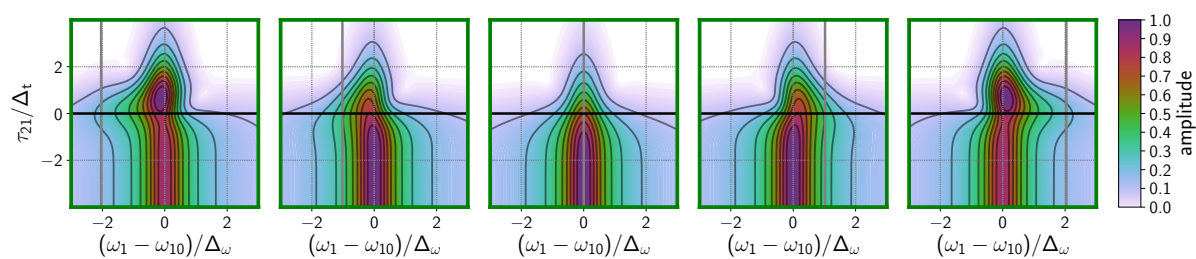


Figure 9.9: Transient ( $\omega_1$ ) line shapes and their dependence on  $\omega_2$  frequency. The relative dephasing rate is  $\Gamma_{10}\Delta_t = 1$  and  $\tau_{22'} = 0$ . For each plot, the corresponding  $\omega_2$  value is shown as a light gray vertical line.

It is also common to represent data as “Wigner plots,” where one axis is delay and the other is frequency.

[KohlerDanielDavid2014a, AubbockGerald2012a, CzechKyleJonathan2015a, PakoulevAndreiV2007a]

In Fig. 9.9 we show five  $\tau_{21, \omega_1}$  plots for varying  $\omega_2$  with  $\tau_{22'} = 0$ . The plots are the analogue to the most common multidimensional experiment of Transient Absorption spectroscopy, where the non-linear probe spectrum is plotted as a function of the pump-probe delay. For each plot, the  $\omega_2$  frequency is denoted by a vertical gray line. Each Wigner plot is scaled to its own dynamic range to emphasize the dependence on  $\omega_2$ . The dramatic line shape changes between positive and negative delays can be seen. This representation also highlights the asymmetric broadening of the  $\omega_1$  line shape near pulse overlap when  $\omega_2$  becomes non-resonant. Again, these features can resemble spectral diffusion even though our system is homogeneous.

#### 9.4.5 Inhomogeneous broadening

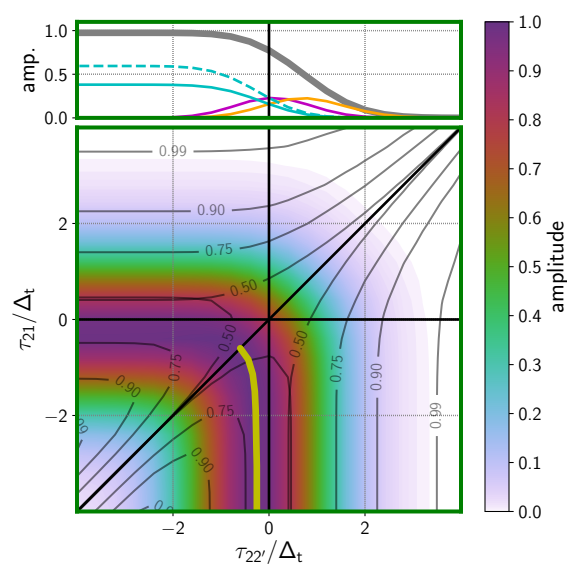


Figure 9.10: 2D delay response for  $\Gamma_{10}\Delta_t = 1$  with sample inhomogeneity. All pulses are tuned to exact resonance. The colors depict the signal amplitude. The black contour lines show signal purity,  $P$  (see Equation 9.25), with purity values denoted on each contour. The thick yellow line denotes the peak amplitude position that is used for 3PEPS analysis. The small plot above each 2D delay plot examines a  $\tau_{22}'$  slice of the delay response ( $\tau_{21} = 0$ ). The plot shows the total signal (black), as well as the component time-orderings VI (orange), V (purple), III (teal, dashed), and I (teal, solid).

With the homogeneous system characterized, we can now consider the effect of inhomogeneity. For inhomogeneous systems, time-orderings III and V are enhanced because their final coherence will rephase to form a photon echo, whereas time-orderings I and VI will not. In delay space, this rephasing appears as a shift of signal to time-ordered regions III and V that persists for all population times. Fig. 9.10 shows the calculated spectra for relative dephasing rate  $\Gamma_{10}\Delta_t = 1$  with a frequency broadening function of width  $\Delta_{\text{inhom}} = 0.441\Gamma_{10}$ . The inhomogeneity makes it easier to temporally isolate the rephasing pathways and harder to isolate the non-rephasing pathways, as shown by the purity contours.

A common metric of rephasing in delay space is the 3PEPS measurement. [WeinerAM1985a, FlemingGrahmR1998a, DeBoeijWimP1998a, SalvadorMayroseR2008a] In 3PEPS, one measures the signal as the first coherence time,  $\tau$ , is scanned across both rephasing and non-rephasing pathways while keeping population time,  $T$ , constant. The position of the peak is measured; a peak shifted away from  $\tau = 0$  reflects the rephasing ability of the system. An inhomogeneous system will emit a photon echo in the rephasing pathway, enhancing signal in the rephasing time-ordering and creating the peak shift. In our 2D delay space, the  $\tau$  trace can be defined if we assume  $E_2$  and  $E_{2'}$  create the population (time-orderings V and VI). The trace runs parallel to the III-V time-ordering boundary (diagonal) if  $\tau_{22'} < 0$  and runs parallel to the IV-VI time-ordering boundary (horizontal) if  $\tau_{22'} > 0$ , and both intersect at  $\tau_{22'} = 0$ ; the  $-\tau_{21}$  value at this intersection is  $T$ . In our 2D delay plots (Fig. 9.7, Fig. 9.10), the peak shift is seen as the diagonal displacement of the signal peak from the  $\tau_{21} = 0$  vertical line. Fig. 9.10 highlights the peak shift profile as a function of population time with the yellow trace; it is easily verified that our static inhomogeneous system exhibits a non-zero peak shift value for all population times.

The unanticipated feature of the 3PEPS analysis is the dependence on  $T$ . Even though our inhomogeneity is static, the peak shift is maximal at  $T = 0$  and dissipates as  $T$  increases, mimicking spectral diffusion. This dynamic arises from signal overlap with time-ordering III, which uses  $E_2$  and  $E_1$  as the first two interactions, and merely reflects  $E_1$  and  $E_2$  temporal overlap. At  $T = 0$ , the  $\tau$  trace gives two ways to make a rephasing pathway (time-orderings III and V) and only one way to make a non-rephasing pathway (time-ordering VI). This pathway asymmetry shifts signal away from  $\tau = 0$  into the rephasing direction. At large  $T$  (large  $\tau_{21}$ ), time-ordering III is not viable and pathway asymmetry disappears. Peak shifts imply inhomogeneity only when time-orderings V and III are minimally contaminated by each other i.e. at population times that exceed pulse overlap. This fact is easily illustrated by the

dynamics of homogeneous system (Fig. 9.7); even though the homogeneous system cannot rephase, there is a non-zero peak shift near  $T = 0$ . The contamination of the 3PEPS measurement at pulse overlap is well-known and is described in some studies, [DeBoeijWimP1996a, AgarwalRitesh2002a] but the dependence of pulse and system properties on the distortion has not been investigated previously. Peak-shifting due to pulse overlap is less important when  $\omega_1 \neq \omega_2$  because time-ordering III is decoupled by detuning.

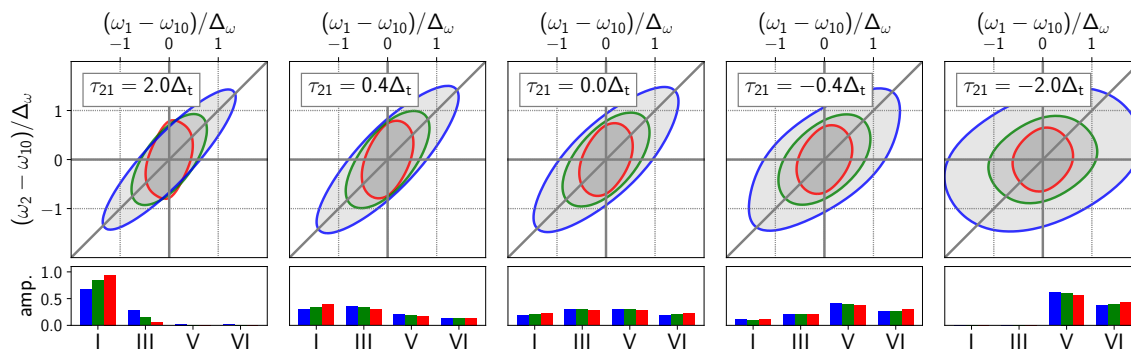


Figure 9.11: Same as Fig. 9.8, but each system has inhomogeneity ( $\Delta_{\text{inhom}} = 0.441\Gamma_{10}$ ). Relative dephasing rates are  $\Gamma_{10}\Delta_t = 0.5$  (red),  $1.0$  (green), and  $2.0$  (blue). In all plots  $\tau_{22'} = 0$ . To ease comparison between different dephasing rates, the colored line shapes of all three systems are overlaid. Each 2D plot shows a single representative contour (half-maximum) for each  $\Gamma_{10}\Delta_t$  value. The colored histograms below each 2D frequency plot show the relative weights of each time-ordering for each 2D frequency plot. In contrast to Fig. 9.8, inhomogeneity makes the relative contributions of time-orderings V and VI unequal.

In frequency space, spectral elongation along the diagonal is the signature of inhomogeneous broadening. Fig. 9.11 shows the line shape changes of a Gaussian inhomogeneous distribution. All systems are broadened by a distribution proportional to their dephasing bandwidth. As expected, the sequence again shows a gradual broadening along the  $\omega_1$  axis, with a strong spectral correlation at early delays ( $\tau_{21} > 0$ ) for the more driven signals. The anti-diagonal width at early delays (e.g. Fig. 9.11,  $\tau_{21} = 2.0\Delta_t$ ) again depends on the pulse bandwidth and the monochromator slit width. At delay values that isolate time-orderings V and VI, however, the line shapes retain diagonal character, showing the characteristic balance of homogeneous and inhomogeneous width.

## 9.5 Discussion

### 9.5.1 An intuitive picture of pulse effects

Our chosen values of the relative dephasing time,  $\Gamma_{10}\Delta_t$ , describe experiments where neither the impulsive nor driven limit unilaterally applies. We have illustrated that in this intermediate regime, the multidimensional spectra contain attributes of both limits, and that it is possible to judge when these attributes apply. In our three-pulse experiment the second and third pulses time-gate coherences and populations produced by the previous pulse(s), and the monochromator frequency-gates the final coherence. Time-gating isolates different properties of the coherences and populations. Consequently, spectra evolve against delay. For any delay coordinate, one can develop qualitative line shape expectations by considering the following three principles:

1. When time-gating during the pulse, the system pins to the driving frequency with a buildup efficiency determined by resonance.
2. When time-gating after the pulse, the FID dominates the system response.
3. The emitted signal field contains both FID and driven components; the  $\omega_{\text{out}} = \omega_1$  component is isolated by the tracking monochromator.

Fig. 9.4 illustrates principles 1 and 2 and Fig. 9.5 illustrates principle 2 and 3. Fig. 9.6 provides a detailed example of the relationship between these principles and the multidimensional line shape



changes for different delay times.

The principles presented above apply to a single pathway. For rapidly dephasing systems it is difficult to achieve complete pathway discrimination, as shown in Fig. 9.7. In such situations the interference between pathways must be considered to predict the line shape. The relative weight of each pathway to the interference can be approximated by the extent of pulse overlap. The pathway weights exchange when scanning across pulse overlap, which creates the dramatic line shape changes observed in Figs. 9.8 and 9.11.

### 9.5.2 Conditional validity of the driven limit

We have shown that the driven limit misses details of the line shape if  $\Gamma_{10}\Delta_t \approx 1$ , but we have also reasoned that in certain conditions the driven limit can approximate the response well (see principle 1). Here we examine the line shape at delay values that demonstrate this agreement. Fig. 9.12 compares the results of our numerical simulation (third column) with the driven limit expressions for populations where  $\Gamma_{11}\Delta_t = 0$  (first column) or 1 (second column). The top and bottom rows compare the line shapes when  $(\tau_{22'}, \tau_{21} = (0, 0))$  and  $(0, -4\Delta_t)$ , respectively. The third column demonstrates the agreement between the driven limit approximations with the simulation by comparing the diagonal and anti-diagonal cross-sections of the 2D spectra.

Note the very sharp diagonal feature that appears for  $(\tau_{21}, \tau_{22'}) = (0, 0)$  and  $\Gamma_{11} = 0$ ; this is due to population resonance in time-orderings I and III. This expression is inaccurate: the narrow resonance is only observed when pulse durations are much longer than the coherence time. A comparison of picosecond and femtosecond studies of quantum dot exciton line shapes (Yurs *et al.* [YursLenaA2011a] and KohlerDanielDavid2014a, respectively) demonstrates this difference well. The driven equation fails to reproduce our numerical simulations here because resonant excitation of the population is impulsive; the experiment time-gates only the rise time of the population, yet driven theory predicts the resonance to be vanishingly narrow ( $\Gamma_{11} = 0$ ). In light of this, one can approximate this time-gating effect by substituting population lifetime with the pulse duration ( $\Gamma_{11}\Delta_t = 1$ ), which gives good agreement with the numerical simulation (third column).

When  $\tau_{22'} = 0$  and  $\tau_{21} < \Delta_t$ , signals can also be approximated by driven signal (Fig. 9.12 bottom row). Only time-orderings V and VI are relevant. The intermediate population resonance is still impulsive but it depends on  $\omega_{2'} - \omega_2$  which is not explored in our 2D frequency space.

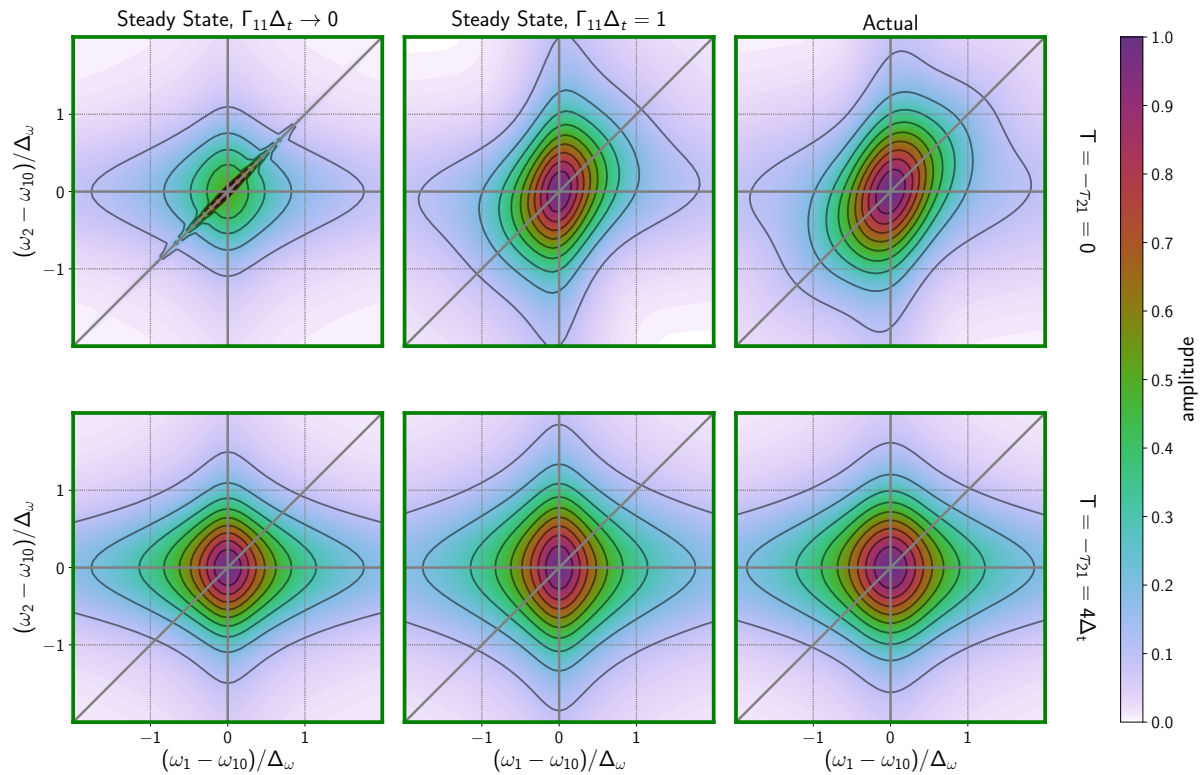


Figure 9.12: Comparing approximate expressions of the 2D frequency response with the directly integrated response.  $\Gamma_{10}\Delta_t = 1$ . The top row compares the 2D response of all time-orderings ( $\tau_{21} = 0$ ) and the bottom row compares the response of time-orderings V and VI ( $\tau_{21} = -4\Delta_t$ ). First column: The driven limit response. Note the narrow diagonal resonance for  $\tau_{21} = 0$ . Second column: Same as the first column, but with ad hoc substitution  $\Gamma_{11} = \Delta_t$ . Third column: The directly integrated response.

### 9.5.3 Extracting true material correlation

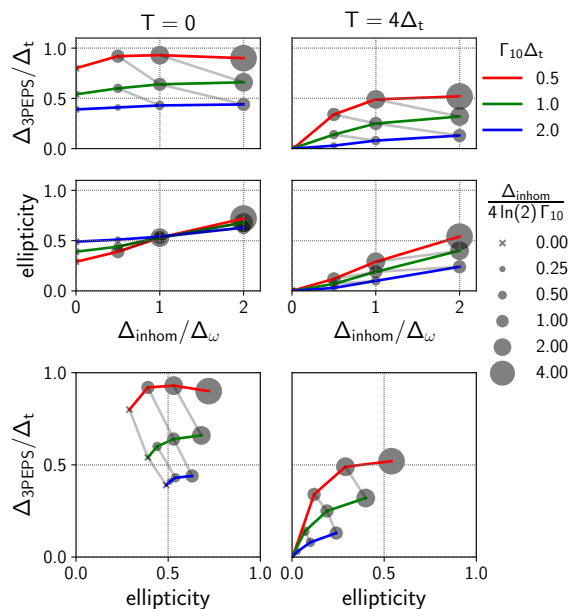


Figure 9.13: Temporal (3PEPS) and spectral (ellipticity) metrics of correlation and their relation to the true system inhomogeneity. The left column plots the relationship at pulse overlap ( $T = 0$ ) and the right column plots the relationship at a delay where driven correlations are removed ( $T = 4\Delta_t$ ). For the ellipticity measurements,  $\tau_{22'} = 0$ . In each case, the two metrics are plotted directly against system inhomogeneity (top and middle row) and against each other (bottom row). Colored lines guide the eyes for systems with equal relative dephasing rates ( $\Gamma_{10}\Delta_t$ , see upper legend), while the area of the data point marker indicates the relative inhomogeneity ( $\Delta_{\text{inhom}}/\Gamma_{10}$ , see lower legend). Gray lines indicate contours of constant relative inhomogeneity (scatter points with the same area are connected).

We have shown that pulse effects mimic the qualitative signatures of inhomogeneity. Here we address how one can extract true system inhomogeneity in light of these effects. We focus on two ubiquitous metrics of inhomogeneity: 3PEPS for the time domain and ellipticity for the frequency domain [KwacKijeong2003a, OkumuraKo1999a]. There are many ways to characterize the ellipticity of a peak shape. We adopt the convention  $\mathcal{E} = (a^2 - b^2) / (a^2 + b^2)$ , where  $a$  is the diagonal width and  $b$  is the antidiagonal width. In the driven (impulsive) limit, ellipticity (3PEPS) corresponds to the frequency correlation function and uniquely extracts the inhomogeneity of the models presented here. In their respective limits, the metrics give values proportional to the inhomogeneity.

Fig. 9.13 shows the results of this characterization for all  $\Delta_{\text{inhom}}$  and  $\Gamma_{10}\Delta_t$  values explored in this work. We study how the correlations between the two metrics depend on the relative dephasing rate,  $\Gamma_{10}\Delta_t$ , the absolute inhomogeneity,  $\Delta_{\text{inhom}}/\Delta_\omega$ , the relative inhomogeneity  $\Delta_{\text{inhom}}/\Gamma_{10}$ , and the population time delay. The top row shows the correlations of the  $\Delta_{3\text{PEPS}}/\Delta_t$  3PEPS metric that represents the normalized coherence delay time required to reach the peak intensity. The upper right graph shows the correlations for a population time delay of  $T = 4\Delta_t$  that isolates the V and VI time-orderings. For this time delay, the  $\Delta_{3\text{PEPS}}/\Delta_t$  metric works well for all dephasing times of  $\Gamma_{10}\Delta_t$  when the relative inhomogeneity is  $\Delta_{\text{inhom}}/\Delta_\omega \ll 1$ . It becomes independent of  $\Delta_{\text{inhom}}/\Delta_\omega$  when  $\Delta_{\text{inhom}}/\Delta_\omega > 1$ . This saturation results because the frequency bandwidth of the excitation pulses becomes smaller than the inhomogeneous width and only a portion of the inhomogeneous ensemble contributes to the 3PEPS experiment. [WeinerAM1985a] The corresponding graph for  $T = 0$  shows a large peak shift occurs, even without inhomogeneity. In this case, the peak shift depends on pathway overlap, as discussed in Section 9.4.5.

The middle row in Fig. 9.13 shows the ellipticity dependence on the relative dephasing rate and inhomogeneity assuming the measurement is performed when the first two pulses are temporally overlapped ( $\tau_{22'} = 0$ ). For a  $T = 4\Delta_t$  population time, the ellipticity is proportional to the inhomogeneity until  $\Delta_{\text{inhom}}/\Delta_\omega \ll 1$  where the excitation bandwidth is wide compared with the inhomogeneity. Unlike 3PEPS, saturation is not observed because pulse bandwidth does not limit the frequency range scanned. The 3PEPS and ellipticity metrics are therefore complementary since 3PEPS works well for  $\Delta_{\text{inhom}}/\Delta_\omega \ll 1$  and ellipticity works well for  $\Delta_{\text{inhom}}/\Delta_\omega \gg 1$ . When all pulses are temporally overlapped at  $T = 0$ , the ellipticity is only weakly dependent on the inhomogeneity and dephasing rate.

The ellipticity is instead dominated by the dependence on the excitation pulse frequency differences of time-orderings I and III that become important at pulse overlap.

It is clear from the previous discussion that both metrics depend on the dephasing and inhomogeneity. The dephasing can be measured independently in the frequency or time domain, depending upon whether the dephasing is very fast or slow, respectively. In the mixed frequency/time domain, measurement of the dephasing becomes more difficult. One strategy to address this challenge is to use both the 3PEPS and ellipticity metrics. The bottom row in Fig. 9.13 plots 3PEPS against ellipticity to show how the relationship between the metrics changes for different amounts of dephasing and inhomogeneity. The anti-diagonal contours of constant relative inhomogeneity show that these metrics are complementary and can serve to extract the system correlation parameters.

Importantly, the metrics are uniquely mapped both in the presence and absence of pulse-induced effects (demonstrated by  $T = 0$  and  $T = 4\Delta_t$ , respectively). The combined metrics can be used to determine correlation at  $T = 0$ , but the correlation-inducing pulse effects give a mapping significantly different than at  $T = 4\Delta_t$ . At  $T = 0$ , 3PEPS is almost nonresponsive to inhomogeneity; instead, it is an almost independent characterization of the pure dephasing. In fact, the  $T = 0$  trace is equivalent to the original photon echo traces used to resolve pure dephasing rates.[AartsmaThijsJ1976a] Both metrics are offset due to the pulse overlap effects. Accordingly, the region to the left of homogeneous contour is non-physical, because it represents observed correlations that are less than that given by pulse overlap effects. If the metrics are measured as a function of  $T$ , the mapping gradually changes from the left figure to the right figure in accordance with the pulse overlap. Both metrics will show a decrease, even with static inhomogeneity. If a system has spectral diffusion, the mapping at late times will disagree with the mapping at early times; both ellipticity and 3PEPS will be smaller at later times than predicted by the change in mappings alone.

## 9.6 Conclusion

This study provides a framework to describe and disentangle the influence of the excitation pulses in mixed-domain ultrafast spectroscopy. We analyzed the features of mixed domain spectroscopy through

detailed simulations of MR-CMDS signals. When pulse durations are similar to coherence times, resolution is compromised by time-bandwidth uncertainty and the complex mixture of driven and FID response. The dimensionless quantity  $\Delta_t (\Gamma_f + i\kappa_f \Omega_{f_x})$  captures the balance of driven and FID character in a single field-matter interaction. In the nonlinear experiment, with multiple field-matter interactions, this balance is also controlled by pulse delays and frequency-resolved detection. Our analysis shows how these effects can be intuitive.

The dynamic nature of pulse effects can lead to misleading changes to spectra when delays are changed. When delays separate pulses, the spectral line shapes of individual pathways qualitatively change because the delays isolate FID contributions and de-emphasize driven response. When delays are scanned across pulse overlap, the weights of individual pathways change, further changing the line shapes. In a real system, these changes would all be present in addition to actual dynamics and spectral changes of the material.

Finally, we find that, in either frequency or time domain, pulse effects mimic signatures of ultrafast inhomogeneity. Even homogeneous systems take on these signatures. For mixed domain experiments, pulse effects induce spectral ellipticity and photon echo signatures, even in homogeneous systems. Driven character gives rise to pathway overlap peak shifting in the 2D delay response, which artificially produces rephasing near pulse overlap. Driven character also produces resonances that depend on  $\omega_1 - \omega_2$  near pulse overlap. Determination of the homogeneous and inhomogeneous broadening at ultrashort times is only possible by performing correlation analysis in both the frequency and time domain.



## **Part III**

# **Applications**



## Chapter 10

# PbSe

Relevant content from PbSe publications goes here.



## Chapter 11

# Transition metal dichalcogenide thin films

*This Chapter borrows extensively from CzechKyleJonathan2015a.*

We report the first coherent multidimensional spectroscopy study of a MoS<sub>2</sub> film. A four-layer sample of MoS<sub>2</sub> was synthesized on a silica substrate by a simplified sulfidation reaction and characterized by absorption and Raman spectroscopy, atomic force microscopy, and transmission electron microscopy. State-selective coherent multidimensional spectroscopy (CMDS) on the as-prepared MoS<sub>2</sub> film resolved the dynamics of a series of diagonal and cross-peak features involving the spin—orbit split A and B excitonic states and continuum states. The spectra are characterized by striped features that are similar to those observed in CMDS studies of quantum wells where the continuum states contribute strongly to the initial excitation of both the diagonal and cross-peak features, while the A and B excitonic states contributed strongly to the final output signal. The strong contribution from the continuum states to the initial excitation of both the diagonal and cross-peak features, while the A and B excitonic states contributed strongly to the final output signal. The strong contribution from the continuum states to the initial excitation shows that the continuum states are coupled to the A and B excitonic states and that fast intraband relaxation is occurring on a sub-70 fs time scale. A comparison of the CMDS excitation signal and the absorption spectrum shows that the relative importance of the continuum

states is determined primarily by their absorption strength. Diagonal and cross-peak features decay with a 680 fs time constant characteristic of exciton recombination and/or trapping. The short time dynamics are complicated by coherent and partially coherent pathways that become important when the excitation pulses are temporally overlapped. In this region, the coherent dynamics create diagonal features involving both the excitonic states and continuum states, while the partially coherent pathways contribute to cross-peak features.

## 11.1 Introduction

Transition metal dichalcogenides (TMDCs), such as MoS<sub>2</sub>, are layered semiconductors with strong spin-orbit coupling, high charge mobility, and an indirect band gap that becomes direct for monolayers. [WangQingHua2012a, MakKinFai2010a] The optical properties are dominated by the A and B excitonic transitions between two HOMO spin-orbit split valence bands and the lowest state of the conduction band at the *K* and *K'* valleys of the two-dimensional hexagonal Brillouin zone. [MolinaSanchezAlejandro2013a] The spin and valley degrees of freedom are coupled in individual TMDC layers as a result of the strong spin-orbit coupling and the loss of inversion symmetry. The coupling suppresses spin and valley relaxation since both spin and valley must change in a transition. These unusual properties have motivated the development of TMDC monolayers for next-generation nano/optoelectronic devices as well as model systems for spintronics and valleytronics applications. [MakKinFai2010a, XuXiaodong2014a, XiaoDi2012a]

Ultrafast dynamics of the MoS<sub>2</sub> A and B electronic states have been measured by pump-probe, transient absorption, and transient reflection spectroscopy. [FangHui2014a, KumarNardeep2013a, NieZhaogang2014a, SunDezheng2014a, SimSangwan2013a] The spectra contain A and B excitonic features that result from ground-state bleaching (GSB), stimulated emission (SE), and excited-state absorption (ESA) pathways. The excitons exhibit biexponential relaxation times of  $\approx 10$ – $20$  and  $\approx 350$ – $650$  fs, depending on the fluence and temperature. The dependence on excitation frequency has not been explored in previous ultrafast experiments on MoS<sub>2</sub>, but it has played a central role in understanding exciton cooling dynamics and exciton-phonon coupling in studies of quantum dots. [KambhampatiPatanjali2011a]

Coherent multidimensional spectroscopy (CMDS) is a complementary four wave mixing (FWM) methodology that differs from pump-probe, transient absorption, and transient reflection methods. [XiaoDi2012a, FangHui2014a, KumarNardeep2013a, NieZhaogang2014a, SimSangwan2013a, MakKinFai2012a, SunDezheng2014a] Rather than measuring the intensity change of a probe beam caused by the state population changes induced by a pump beam, CMDS measures the intensity of a coherent output beam created by interactions with three excitation pulses. The interest in CMDS methods arise from their ability to remove inhomogeneous broadening, define interstate coupling, and resolve coherent and incoherent dynamics. [CundiffStevenT2008a, TurnerDanielB2009a, KohlerDanielDavid2014a, YursLenaA2011a, GriffinGrahamB2013a, HarelElad2012a, CundiffStevenT1996a, BirkedaDI1996a, WehnerMU1996a] CMDS typically requires interferometric phase stability between excitation pulses, so CMDS has been limited to materials with electronic states within the excitation-pulse bandwidth. Multiresonant CMDS is a particularly attractive method for the broader range of complex materials because it does not require interferometric stability and is able to use independently tunable excitation pulses over wide frequency ranges.

The multiresonant CMDS used in this work employs two independently tunable excitation beams with frequencies  $\omega_1$  and  $\omega_2$ . The  $\omega_2$  beam is split into two beams, denoted by  $\omega_2$  and  $\omega_2'$ . These three beams are focused onto the MoS<sub>2</sub> thin film at angles, creating an output beam in the phase-matched direction  $\mathbf{k}_{\text{out}} = \mathbf{k}_1 - \mathbf{k}_2 + \mathbf{k}_{2'}$  where  $\mathbf{k}$  is the wave vector for each beam and the subscripts label the excitation frequencies. Multidimensional spectra result from measuring the output intensity dependence on frequency and delay times.

Figure 11.1 introduces our conventions for representing multidimensional spectra. Figure 11.1b,d are simulated data. Figure 11.1a shows one of the six time orderings of the three excitation pulses where  $\tau_{22'} \equiv t_2 - t_{2'} > 0$  and  $\tau_{21} \equiv t_2 - t_1 < 0$ ; that is, the  $\omega_{2'}$  pulse interacts first and the  $\omega_1$  pulse interacts last. Figure 11.1b illustrates the 2D delay-delay spectrum for all six time orderings when  $\omega_1$  and  $\omega_2$  are both resonant with the same state. The color denotes the output amplitude. Along the negative ordinate where  $\tau_{22'} = 0$ , interactions with the  $\omega_2$  and  $\omega_{2'}$  pulses create a population that is probed by  $\omega_1$ . Similarly, along the negative abscissa where  $\tau_{21} = 0$ , interactions with the  $\omega_2$  and  $\omega_1$  pulses create a population that is probed by  $\omega_{2'}$ . The decay along these axes measures the population relaxation dynamics. Note that these delay representations differ from previous publications by our

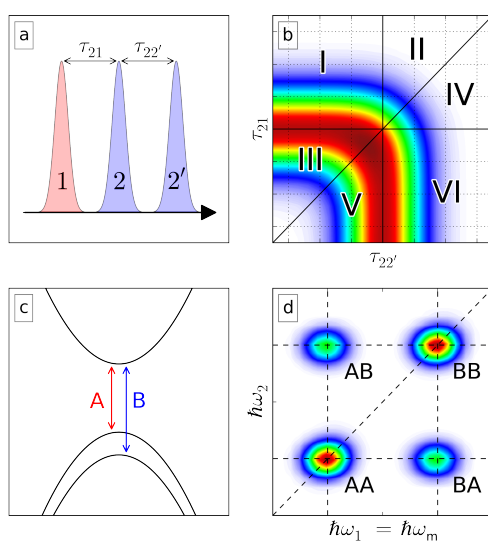


Figure 11.1: (a) Example delays of the  $\omega_1$ ,  $\omega_2$ , and  $\omega_{2'}$  excitation pulses. (b) Dependence of the output intensity on the  $\tau_{22'}$  and  $\tau_{21}$  time delays for  $\omega_1 = \omega_2$ . The solid lines define the regions for the six different time orderings of the  $\omega_1$ ,  $\omega_2$ , and  $\omega_{2'}$  excitation pulses. We have developed a convention for numbering these time orderings, as shown. (c) Diagram of the band structure of MoS<sub>2</sub> at the *K* point. The A and B exciton transitions are shown. (d) Two dimensional frequency-frequency plot labeling two diagonal and cross-peak features for the A and B excitons.



group. [PakoulevAndreiV2006a] This paper specifically explores the dynamics along the ordinate where  $\tau_{22'}$  is zero and the  $\tau_{21}$  delay is changed.

Figure 11.1c depicts the A and B excitonic transitions between the spin-orbit split valence bands and the degenerate conduction band states of MoS<sub>2</sub>. Figure 11.1d illustrates the 2D frequency-frequency spectrum when  $\omega_1$  and  $\omega_2$  are scanned over two narrow resonances. The spectrum contains diagonal and cross-peaks that we label according to the excitonic resonances AA, AB BA, and BB for illustrative purposes. The dynamics of the individual quantum states are best visualized by 2D frequency-delay plots, which combine the features seen in Figure 11.1b,d.

This work reports the first multiresonant CMDS spectra of MoS<sub>2</sub>. It includes the excitation frequency dependence of the A and B excitonic-state dynamics. These experiments provide a fundamental understanding of the multidimensional MoS<sub>2</sub> spectra and a foundation for interpreting CMDS experiments on more complex TMDC heterostructures. The experimental spectra differ from the simple 2D spectrum shown in Figure 11.1d and those of earlier CMDS experiments with model systems. The line shape of the CMDS excitation spectrum closely matches the absorption spectrum, but the line shape of the output coherence is dominated by the A and B excitonic features. The difference arises from fast, < 70 fs intraband relaxation from the hot A and B excitons of the continuum to the band edge. A longer, 680 fs relaxation occurs because of trapping and/or exciton dynamics. [SimSangwan2013a] The intensity of the cross-peaks depends on the importance of state filling and intraband relaxation of hot A excitons as well as the presence of interband population transfer of the A and B exciton states.

## 11.2 Methods

MoS<sub>2</sub> thin films were prepared *via* a Mo film sulfidation reaction, similar to methods reported by LaskarMasihhurR2013a. A 1 nm amount of Mo (Kurt J. Lesker, 99.95%) metal was electron-beam evaporated onto a fused silica substrate at a rate of 0.05 Å/s. The prepared Mo thin films were quickly transferred to the center of a 1-inch fused silica tub furnace equipped with gas flow controllers (see Figure 11.2) and purged with Ar. The temperature of the Mo substrate was increased to 900 °C over the course of 15 min, after which 200 mg of sulfur was evaporated into the reaction chamber. Sulfidation

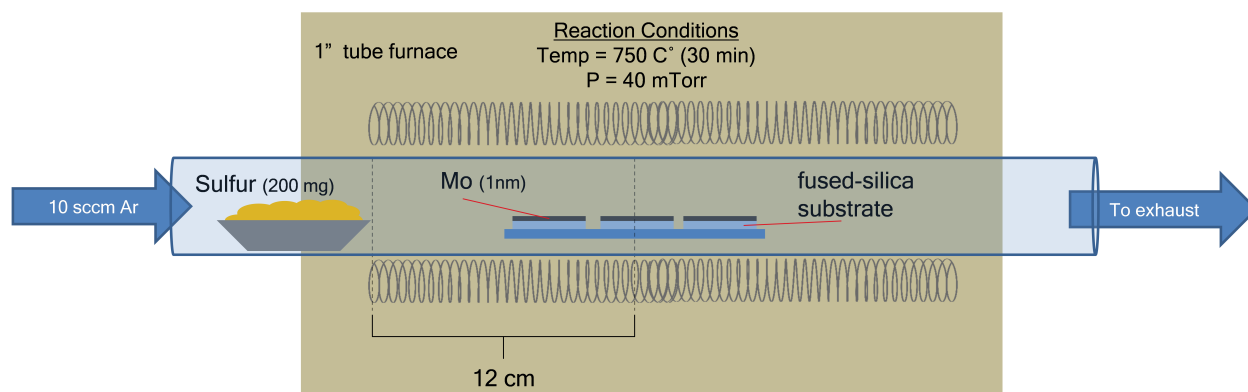


Figure 11.2: Schematic of the synthetic setup used for Mo thin film sulfidation reactions.

was carried out for 30 min, and the furnace was subsequently cooled to room temperature; then the reactor tube was returned to atmospheric pressure, and the MoS<sub>2</sub> thin film samples were collected. The MoS<sub>2</sub> samples were characterized and used for CMDS experiments with no further preparation.

MoS<sub>2</sub> thin film absorption spectra were collected by a Shimadzu 2401PC ultraviolet-visible spectrophotometer. Raman and photoluminescence experiments were carried out in parallel using a Thermo DXR Raman microscope with a 100x 0.9 NA focusing objective and a 2.0 mW 532 nm excitation source. Raman/PL measurements were intentionally performed at an excitation power of <8.0 mW to prevent sample damage. [CastellanosGomezA2012a] Contact-mode atomic force microscopy was performed with an Agilent 5500 AFM. MoS<sub>2</sub> film thickness was determined by scratching the sample to provide a clean step-edge between the MoS<sub>2</sub> film and the fused silica substrate. TEM samples were prepared following the method outlined by ShanmugamMariyappan2012a using concentrated KOH in a 35 °C oil bath for 20 minutes. The delaminated MoS<sub>2</sub> sample was removed from the basic solution, rinsed five times with DI water, and transferred to a Cu-mesh TEM grid. TEM experiments were performed on a FEI Titan aberration corrected (S)TEM under 200 kV accelerating voltage.

The coherent multidimensional spectroscopy system used a 35 fs seed pulse, centered at 800 nm and generated by a 1 kHz Tsunami Ti-sapphire oscillator. The seed was amplified by a Spitfire-Pro regenerative amplifier. The amplified output was split to pump two TOPAS-C collinear optical parametric amplifiers. OPA signal output was immediately frequency doubled with BBO crystals, providing two  $\approx 50$  fs independently tunable pulses denoted  $\omega_1$  and  $\omega_2$  with frequencies ranging from 1.62 to 2.12 eV. Signal and idler were not filtered out, but played no role due to their low photon energy. Pulse  $\omega_2$  was split into pulses labeled  $\omega_2$  and  $\omega_2'$  to create a total of three excitation pulses.

In this experiment we use motorized OPAs which allow us to set the output color in software. OPA1 and OPA2 were used to create the  $\omega_1$  and  $\omega_2$  frequencies, respectively. In Figure 11.4 we compare the spectral envelope generated by the OPA at each set color. Negative detuning values correspond to regions of the envelope lower in energy than the corresponding set color. The colorbar allows for comparison between set color intensities. The fluence values reported correspond to the brightest set color for each OPA. A single trace of OPA2 output at set color = 1.95 eV can be found in Figure 11.7.

After passing through automated delay stages (Newport SMC100 actuators), all three beams were

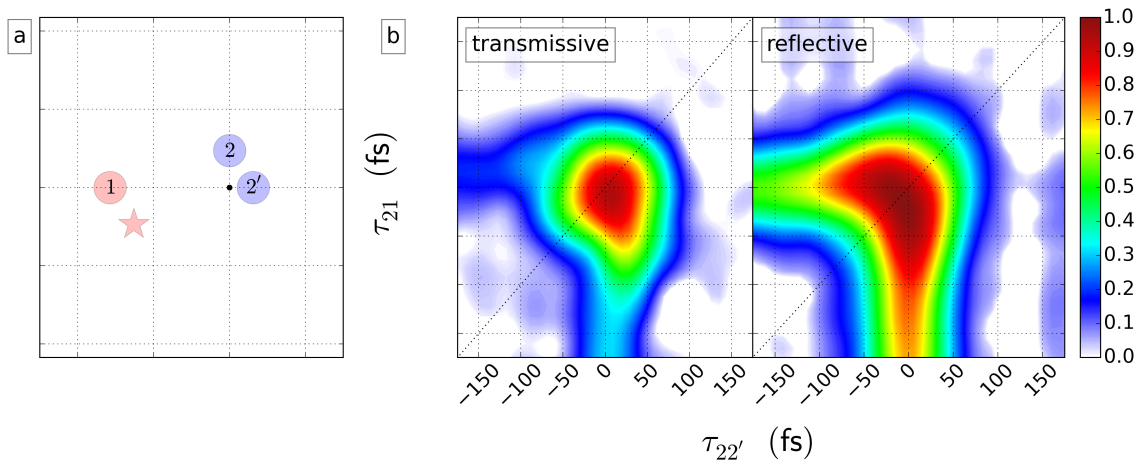


Figure 11.3: (a) Mask. (b) 2D delay spectra at the BB diagonal ( $\omega_1 = \omega_2 \approx 1.95$  eV) for transmissive and reflective geometries. Transmissive signal is a mixture of MoS<sub>2</sub> signal and a large amount of driven signal from the substrate that only appears in the pulse overlap region. Reflective signal is representative of the pure MoS<sub>2</sub> response.

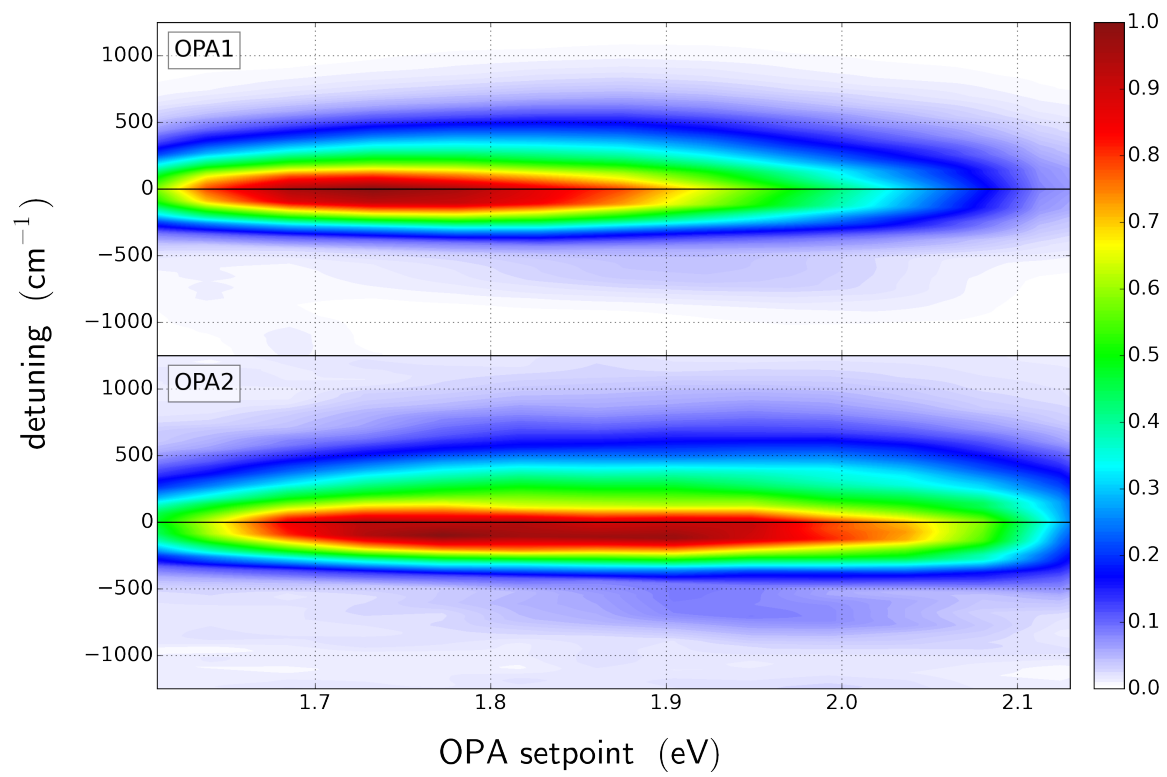


Figure 11.4: OPA outputs at each color explored.

focused onto the sample surface by a 1 meter focal length spherical mirror in a distorted BOXCARS geometry to form a 630, 580, and 580  $\mu\text{m}$  FWHM spot sizes for  $\omega_1$ ,  $\omega_2$ , and  $\omega_{2'}$ , respectively.

Figure 11.5 represents delay corrections applied for each OPA. The corrections were experimentally determined using driven FWM output from fused silica. Corrections were approximately linear against photon energy, in agreement with the normal dispersion of transmissive optics inside our OPAs and between the OPAs and the sample. OPA2 required a relatively small correction along  $\tau_{22'}$  (middle subplot) to account for any dispersion experienced differently between the two split beams. OPA1 was not split and therefore needed no such correction.

Figure 11.3a represents the to-scale mask that defines our distorted BOXCARS configuration. Relative to the center of the BOXCARS mask (small black dot),  $\omega_1$ ,  $\omega_2$ , and  $\omega_{2'}$  enter the sample at angles of 5.0, 1.5, and 1.0 degrees. Each is angled only along the vertical or horizontal dimension, as indicated in Figure 11.3a. This distortion allowed us to remove a large amount of unwanted  $\omega_2$  and  $\omega_{2'}$  photons from our signal path (Figure 11.3a red star).  $\omega_1$  photons were less efficiently rejected, as we show below. The center of the BOXCARS mask was brought into the sample at  $\approx 45$  degrees. All three beams had S polarization. After reflection, the output beam was isolated using a series of apertures, spectrally resolved with a monochromator (spectral resolution 9 meV), and detected using a photomultiplier (RCA C31034A).

Our experimental setup allowed for the collection of both transmissive and reflective (epi-directional) FWM signal. The 2D delay spectra in Figure 11.3b show the presence of a large nonresonant contribution at the origin for the transmissive FWM signal and weaker signals from the  $\text{MoS}_2$  thin film at negative values of  $\tau_{21}$  and  $\tau_{22'}$ . The nonresonant contribution is much weaker than the signals from the film for the reflective signal and is the geometry chosen for this experiment. This discrimination between a film and the substrate was also seen in reflective and transmissive CARS microscopy experiments.

**[VolkmerAndreas2001a]**

Once measured, the FWM signal was sent through a four-stage workup process to create the data set shown here. This workup procedure is visualized in Figure 11.6. We use a chopper and boxcar in active background subtraction mode (averaging 100 laser shots) to extract the FWM signal from  $\omega_1$  and  $\omega_2$  scatter. We collect this differential signal (Figure 11.6b) in software with an additional 50 shots of

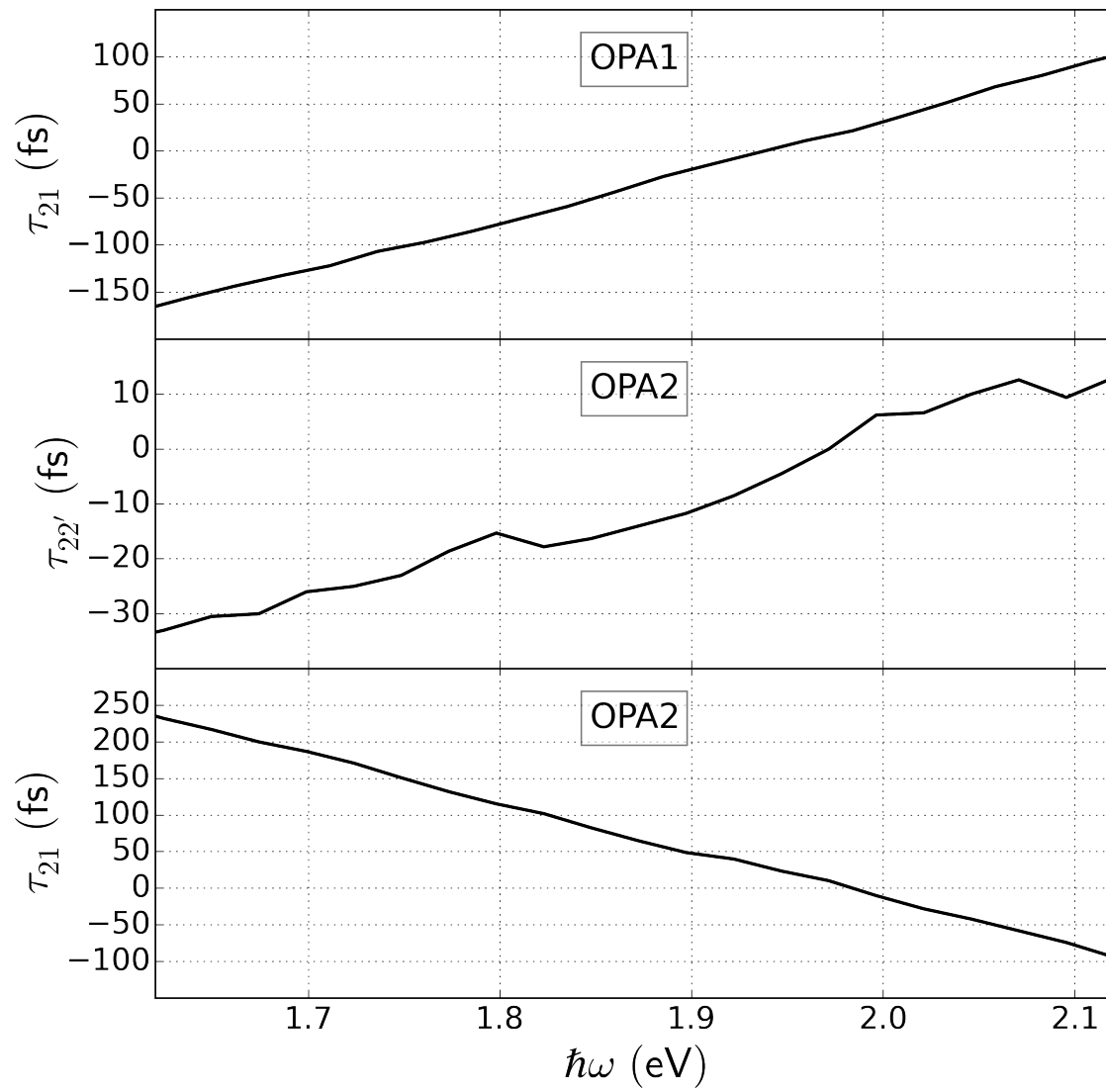


Figure 11.5: Spectral delay correction.

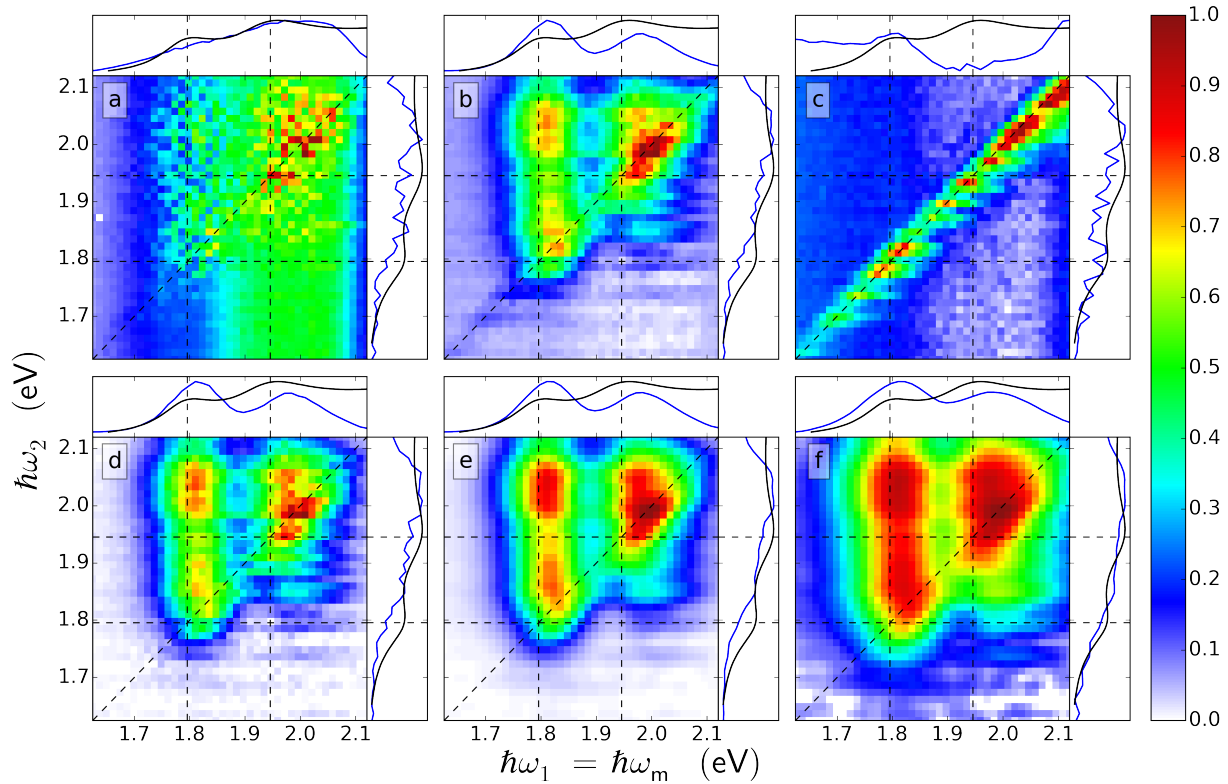


Figure 11.6: Visualization of data collection and processing. With the exception of (c), each subsequent pane represents an additional processing step on top of previous processing. The color bar of each image is separate. (a) Voltages read by the detector at each color combination. The large vertical feature is  $\omega_1$  scatter; the shape is indicative of the power curve of the OPA. MoS<sub>2</sub> response can be barely seen above this scatter. (b) Data after chopping and active background subtraction at the boxcar (100 shots). (c) The portion of chopped signal that is not material response. This portion is extracted by averaging several collections at very positive  $\tau_{21}$  values, where no material response is present due to the short coherence times of MoS<sub>2</sub> electronic states. The largest feature is  $\omega_2$  scatter. Cross-talk between digital-to-analog channels can also be seen as the negative portion that goes as  $\omega_1$  intensity. (d) Signal after (c) is subtracted. (e) Smoothed data. (f) Amplitude level (square root) data. This spectrum corresponds to that at 0 delay in Figure 11.9. Note that the color bar's range is different than in Figure 11.9.



averaging. In post-process we subtract  $\omega_2$  scatter and smooth the data using a 2D Kaiser window. Finally, we represent the homodyne collected data as  $(\text{sig})^{1/2}$  to make the dynamics and line widths comparable to heterodyne-collected techniques like absorbance and pump-probe spectra. Throughout this work, zero signal on the color bar is set to agree with the average rather than the minimum of noise. Values below zero due to measurement uncertainty underflow the color bar and are plotted in white. This is especially evident in lots such as +120 fs in Figure 11.14, where there is no real signal. IPython [PerezFernando2007a] and matplotlib [HunterJohnD2007a] were important for data processing and plotting in this work.

### 11.3 Results and discussion

The few-layer MoS<sub>2</sub> thin film sample studied in this work was prepared on a transparent fused silica substrate by a simple sulfidation reaction of a Mo thin film using a procedure modified from a recent report. [LaskarMasihhurR2013a] Figure 11.7a and b show the homogeneous deposition and surface smoothness of the sample over the centimeter-sized fused silica substrate, respectively. The Raman spectrum shows the  $E_{2g}^1$  and  $A_{1g}$  vibrational modes (Figure 11.7c) that are characteristic of MoS<sub>2</sub>. [LiuLiSongLin2012a] The transmission electron micrograph (TEM) in Figure 11.7d shows the lattice fringes of the film with an inset fast Fourier transform (FFT) of the TEM image indicative of the hexagonal crystal structure of the film corresponding to the 0001 plane of MoS<sub>2</sub>. [LukowskiMarkA2013a] The MoS<sub>2</sub> film thickness was determined to be 2.66 nm by atomic force microscopy and corresponds to approximately four monolayers. Figure 11.73 shows the absorption and fluorescence spectrum of the film along with the A and B excitonic line shapes that were extracted from the absorption spectrum. A representative excitation pulse profile is also shown in red for comparison.

Extracting the exciton absorbance spectrum is complicated by the large “rising background” signal from other MoS<sub>2</sub> bands. With this in mind, we fit the second derivative absorption spectrum to a sum of two second derivative Gaussians, as seen in Figure 11.8. Conceptually, this method can be thought of as maximizing the smoothness (as opposed to minimizing the amplitude) of the remainder between the fit and the absorption spectrum. The fit parameters can be found in the inset table in Figure 11.8. The Gaussians themselves and the remainder can be found in Figure 11.8.

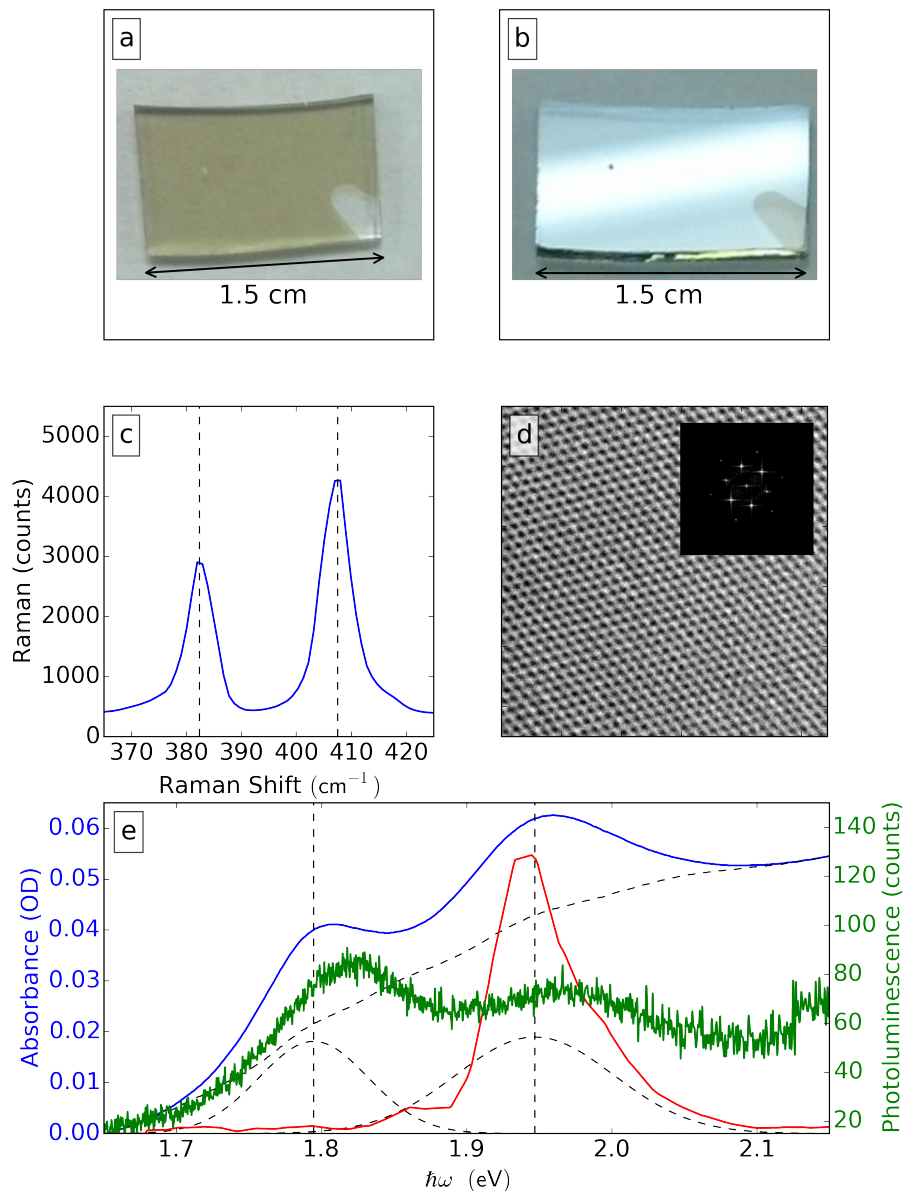


Figure 11.7: Characterization of the few-layer MoS<sub>2</sub> film studied in this work. Optical images of the MoS<sub>2</sub> thin film on fused silica substrate in (a) transmission and (b) reflection. (c) Raman spectrum of the  $E_{2g}^1$  and  $A_{1g}$  vibrational modes. (d) High-resolution TEM image and its corresponding FFT shown in the inset. (e) Absorption (blue), photoluminescence (green), Gaussian fits to the A and B excitons, along with the residues between the fits and absorbance (dotted), A and B exciton centers (dotted) and representative excitation pulse shape (red).

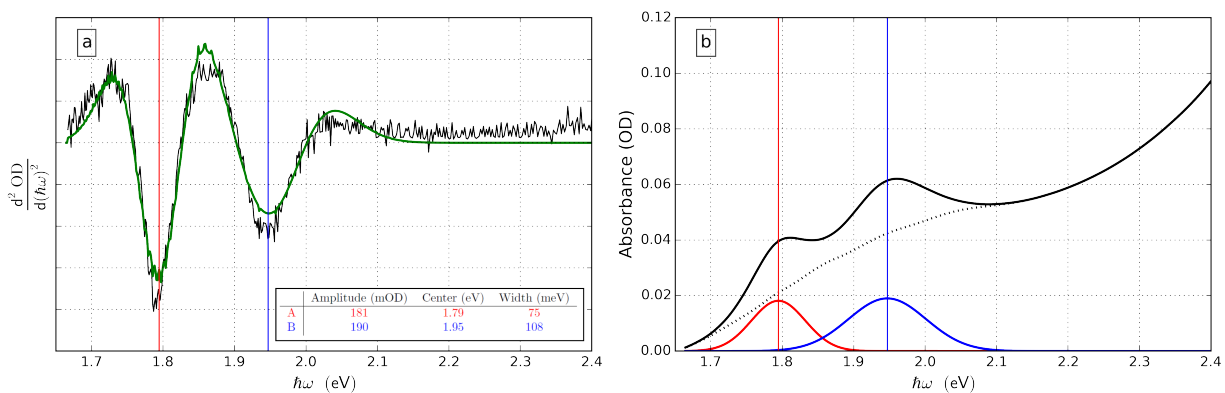


Figure 11.8: Extraction of excitonic features from absorbance spectrum. (a) Second derivative spectra of absorbance (black) and fit second derivative spectrum (green). Gaussian fit parameters are shown in the inset table. (b) Absorption curve (black), Gaussian fits (blue and red), and remainder (black dotted).

The multiresonant CMDS experiment uses  $\approx 70$  fs excitation pulses created by two independently tunable optical parametric amplifiers (OPAs). Automated delay stages and neutral density filters set the excitation time delays over all values of  $\tau_{21}$  with  $\tau_{22'} = 0$  and the pulse fluence to  $90 \mu\text{J}/\text{cm}^2$  ( $114 \mu\text{J}/\text{cm}^2$ ) for the  $\omega_1$  ( $\omega_2$  and  $\omega_{2'}$ ) beam(s). Each pulse was focused onto the sample using a distorted BOXCARS configuration. [EckbrethAlanC1978a] The FWM signal was spatially isolated and detected with a monochromator that tracks the output frequency so  $\omega_m = \omega_1$ . In order to compare the FWM spectra with the absorption spectrum, the signal has been defined as the square root of the measured FWM signal since FWM depends quadratically on the sample concentration and path length.

The main set of data presented in this work is an  $\omega_1\omega_2\tau_{21}$  “movie” with  $\tau_{22'} = 0$ . ?? shows representative 2D frequency-frequency slices from this movie at increasingly negative  $\tau_{21}$  times. Each 2D frequency spectrum contains side plots along both axes that compare the absorbance spectrum (black) to the projection of the integrated signal onto the axis (blue). Along  $\omega_1$  (which for negative  $\tau_{21}$  times acts as the “probe”) we observe two peaks corresponding to the A and B excitons. In contrast, we see no well-defined excitonic peaks along the  $\omega_2$  “pump” axis. Instead, the signal amplitude increases toward bluer  $\omega_2$  values. The decrease in FWM above 2.05 eV is caused by a drop in the  $\omega_2$  OPA power.

Figures 11.10 and 11.11 show representative 2D frequency-delay slices from this movie, where the abscissa is the  $\omega_1$  or  $\omega_2$  frequency, respectively, the ordinate is the  $\tau_{21}$  delay time, and the solid bold lines represent five different  $\omega_2$  or  $\omega_1$  frequencies. The color bar is normalized to the brightest feature in each subplot. This normalization allows comparison of the time dependence of the line shapes, positions, and relative signal amplitudes along the  $\omega_1$  or  $\omega_2$  axis directly.

Each subplot in Figure 11.10 is similar to published pump-probe, transient absorption, multidimensional transient reflection experiments that have measured the electronic dynamics of the A and B excitons. [XiaoDi2012a, FangHui2014a, KumarNardeep2013a, NieZhaogang2014a, SunDezheng2014a, SimSangwan2013a, MakKinFai2012a, ThomallaMarkus2006a] These previous experiments measure relaxation dynamics on the same  $\approx 400$ -600 fs time scale that is characteristic of Figure 11.10.

Our experiments also show how the spectral features change as a function of the  $\omega_2$  excitation frequency. The top to subplots of Figure 11.10 reflect the changes in the AA and BA features, while the bottom two subplots reflect the changes in the AB and BB features. The figure highlights the changes in the

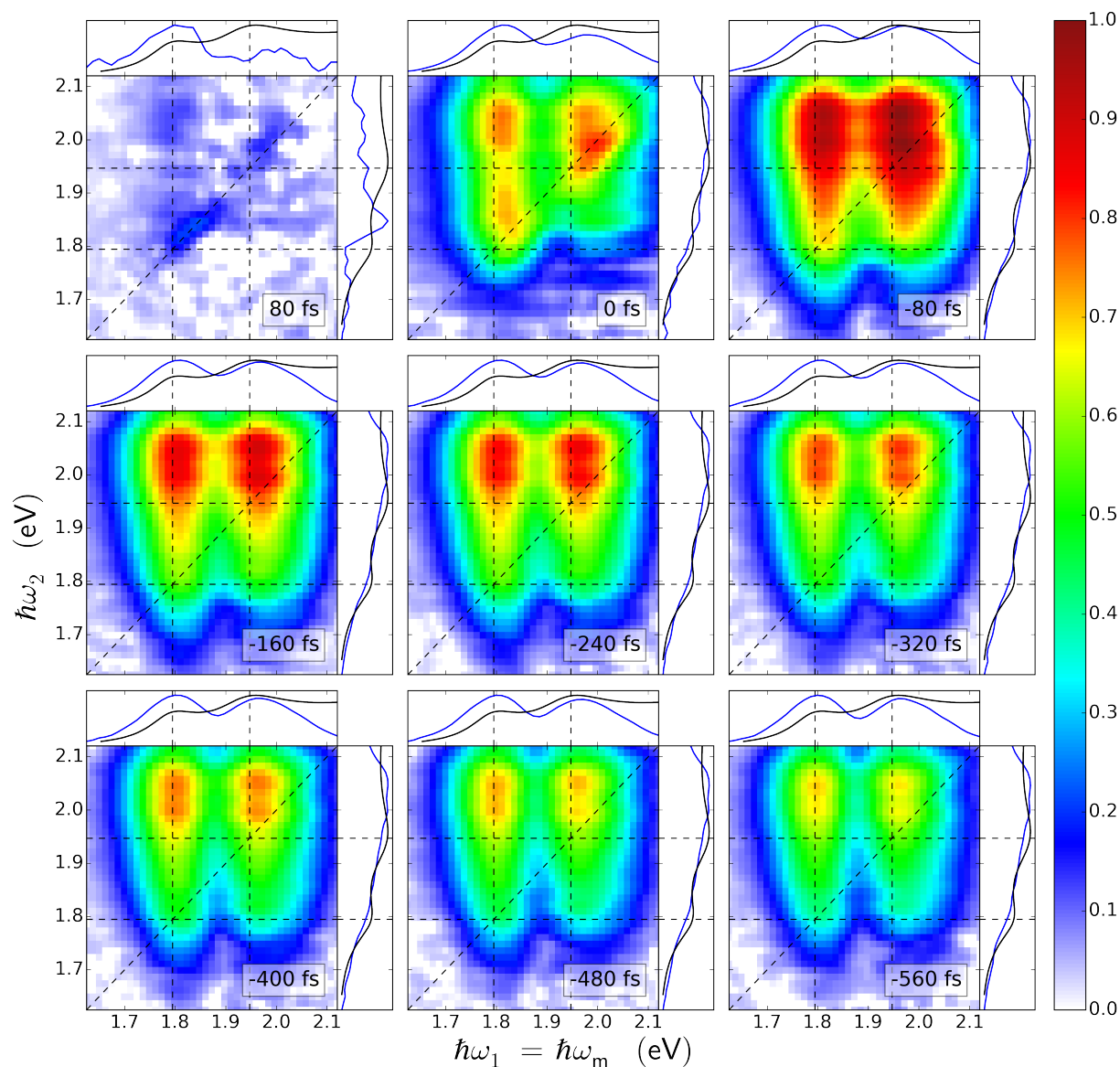


Figure 11.9: 2D frequency-frequency spectra of the MoS<sub>2</sub> sample in the epi configuration. In all spectra  $\tau_{22'} = 0$  fs, while  $\tau_{21}$  is designated in the bottom-right corner of each spectral panel. The color bar defines the square root of the intensity normalized to the most intense feature in the series of spectra. The integration of the signal onto the  $\hbar\omega_1 = \hbar\omega_m$  and  $\hbar\omega_2$  axes are represented as the blue curves in the top and right side plots, respectively. The side plots also contain the absorbance spectrum (black line) to aid interpretation of the dynamics of the integrated 2D signals. The dashed lines mark the centers of the A and B excitons, as designated from the absorbance spectrum.

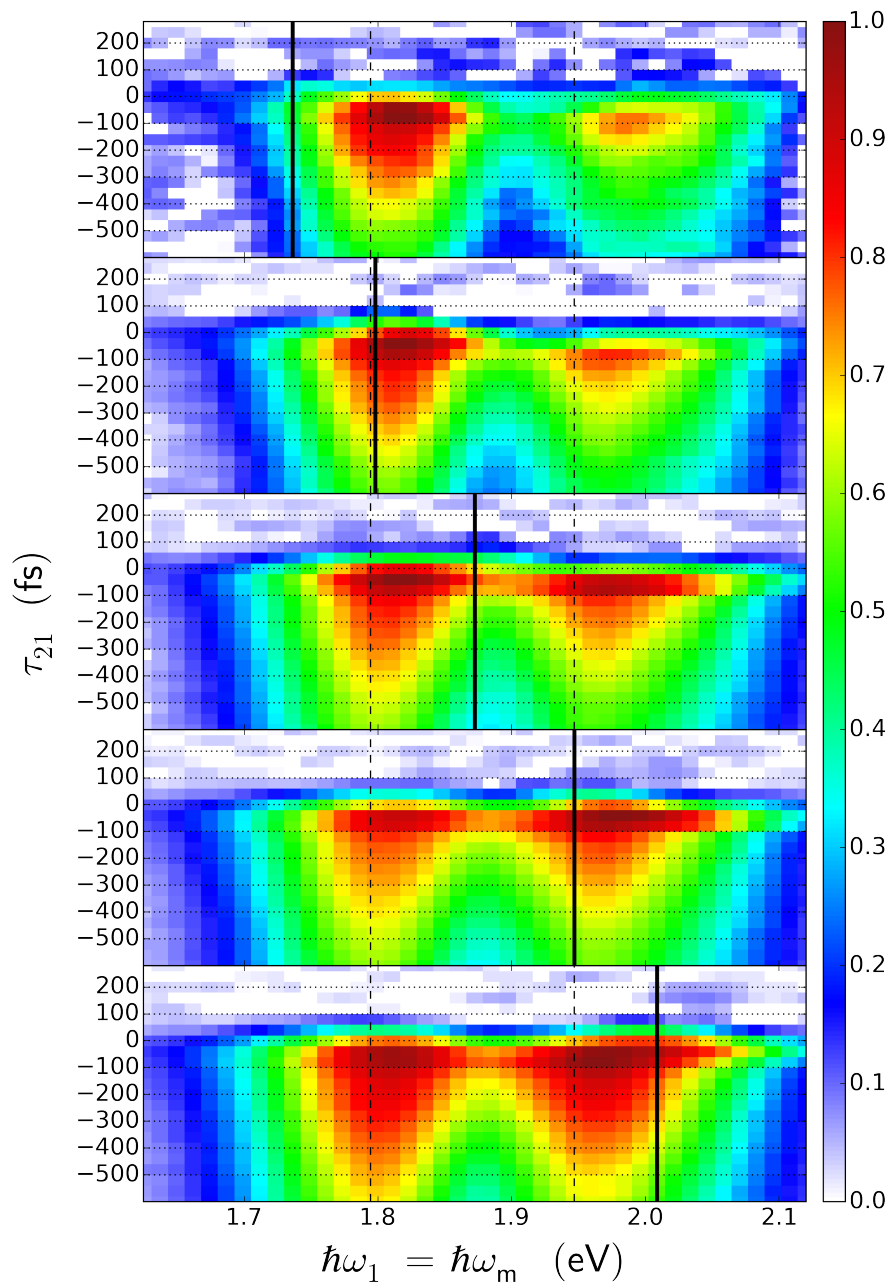


Figure 11.10: Mixed  $\omega_1$ — $\tau_{21}$  time—frequency representations of the 3D data set at five ascending  $\omega_2$  excitation frequencies (solid black lines) showing the impact of the  $\omega_2$  excitation frequency on the  $\omega_1$  spectral line shape as a function of time. The A and B exciton energies are marked as dashed lines within each spectrum.

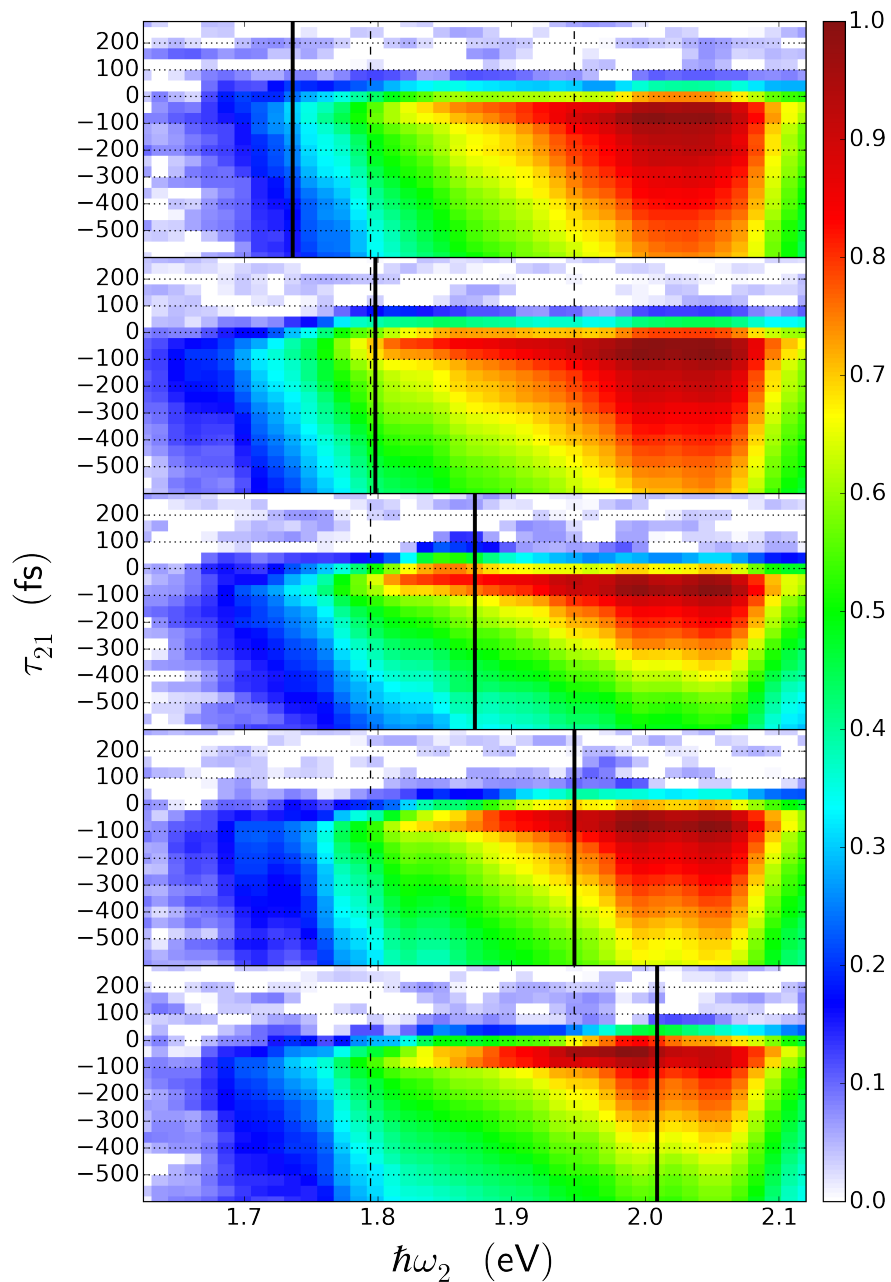


Figure 11.11: Mixed  $\omega_2$ — $\tau_{21}$  time—frequency representations of the 3D data set at five ascending  $\omega_1$  probe frequencies (solid black lines) showing the impact of the  $\omega_1$  excitation frequency on the  $\omega_2$  spectral line shape as a function of time. The A and B exciton energies are marked as dashed lines within each spectrum.

relative amplitude of the A and B features as a function of excitation frequency. Both the line shapes and the dynamics of the spectral features are very similar. Figure 11.11 is an excitation spectrum that shows that the dynamics of the spectral features do not depend strongly on the  $\omega_1$  frequency.

The spectral features in Figures 11.9, 11.10 and 11.11 depend on the quantum mechanical interference effects caused by the different pathways. Figure 11.12 shows all of the Liouville pathways required to understand the spectral features. [PakoulevAndreiV2010a, PakoulevAndreiV2009a] These pathways correspond to the time orderings labeled V and VI in Figure 11.7b. The letters denote the density matrix elements,  $\rho_{ij}$ , where g representst the ground state and e, e' represent any excitonic state. Interaction with the temporally overlapped  $\omega_2$  and  $\omega_2'$  pulses excites the ee excited-state population and bleaches the ground-state population. Subsequent interaction with  $\omega_1$  creates the output coherences for the diagonal spectral features when  $\omega_1 = \omega_2$  or the cross-peak features when  $\omega_1 \neq \omega_2$ . The stimulated emission (SE) and ground-state bleaching (GSB) pathways create the eg or e'g output coherences from the ee and gg populations, respectively, while the excited-state absorption pathway creates the 2e,e or e'+e,e biexcitonic output coherences. Figure 11.12 also includes a population transfer pathway from the ee excited-state population to an e'e' population from which similar SE and ESA pathways occur. Since the ESA pathways destructively interfere with the SE and GSB pathways, the output signal depends on the differences between the pathways. Factors that change the biexcitonic output coherences such as the transition moments, state filling (Pauli blocking), frequency shifts, or dephasing rate changes will control the output signal. State filling and ground-state depletion are important factors for MoS<sub>2</sub> since the transitions excite specific electron and hole spin and valley states in individual layers.

The state-filling and ground-state bleaching effects on the diagonal and cross-peak features in Figure 11.9 depend on the spin and valley states in the output coherence. [XuXiaodong2014a] The effects of these spins will disappear as the spin and valley states return to equilibrium. [ZengHualing2012a, ZhuBairen2014a, MaiCong2013a] If we assume spin relaxation is negligible, the FWM transitions that create the diagonal features involve either the A or B ESA transitions, so the resulting 2e,e state includes two spin-aligned conduction band electrons and valence band holes. Similarly, the cross-peak regions denoted by AB or BA in Figure 11.1d will have two transitions involving an A exciton, so the initial e'+e,e state will include antialigned spins. A quantitative treatment of the cancellation effects between the GSB, SE, and ESA pathways requies knowledge of the transition moments and state



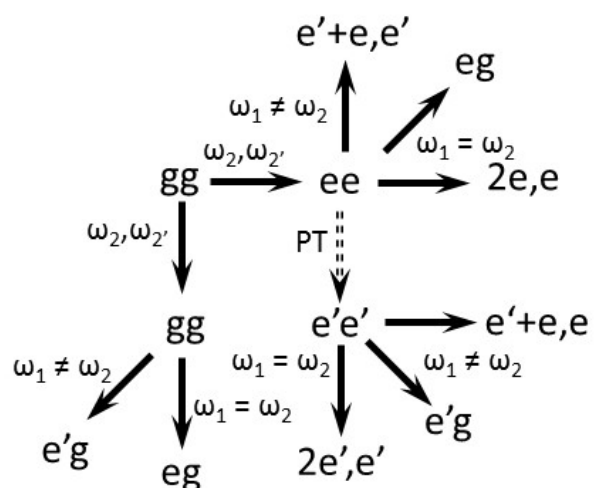


Figure 11.12: Liouville pathways for Figure 11.10.  $gg$  and  $ee$  designate ground- and excited-state populations, the  $eg$ ,  $2e, e$ , and  $e'+e, e$  represent the excitonic and biexcitonic output coherences, and the arrows are labeled with the frequencies or population transfer responsible for the transitions.  $e$  and  $e'$  represent either A or B excitonic states.

degeneracies and is beyond the scope of this paper. [WongCathyY2011a]

The most important characteristic of the experimental spectra is the contrast between the absence of well-resolved excitonic features that depend on  $\omega_2$  in Figures 11.9 and 11.11 and the well-defined excitonic features that depend on  $\omega_1$ . It is also important to note that the projections of the signal amplitude onto the  $\omega_2$  axis in Figure 11.9 match closely with the continuum features in the absorption spectrum and that the line shapes of the features along the  $\omega_2$  axis in Figure 11.11 do not change appreciably for different delay times or  $\omega_1$  values. It should be noted that the excitation pulse bandwidth (see Figure 11.7e) contributes to the absence of well-resolved A and B excitonic features along  $\omega_2$ . The similarity to the continuum states in the absorption spectrum and the absence of a strong dependence on  $\omega_1$  show that the continuum states observed at higher  $\omega_2$  frequencies participate directly in creating the final output coherences and that their increasing importance reflects the increasing absorption strength of higher energy continuum states. In contrast, the features dependent on  $\omega_1$  in Figures 11.9 and 11.10 match the line shapes of the A and B excitonic resonances. Although the relative amplitudes of the spectral features depend on the  $\omega_2$  frequency, they do not depend strongly on the delay times. These characteristics show that hot A and B excitonic states undergo rapid intraband population relaxation over a  $<70$  fs time scale set by excitation pulses to the A and B excitonic states excited by  $\omega_1$ .

A central feature of Figures 11.9 and 11.10 is that the AB region is much brighter than the BA region. This difference is surprising because simple models predict cross-peaks of equal amplitude, as depicted in Figure 11.1d. The symmetry in simple models arises because the AB and BA cross-peaks involve the same four transitions. The symmetry between AB and BA may be broken by material processes such as population relaxation and transfer, the output coherence dephasing rates, and the bleaching and state-filling effects of the valence and conduction band states involved in the transitions.

We believe that ultrafast intraband population transfer breaks the symmetry of AB and BA cross-peaks. For the BA peak, the interactions with  $\omega_2$  and  $\omega_2'$  generate only A excitons that do not relax on  $<70$  fs time scales. For the AB peak,  $\omega_2$  and  $\omega_2'$  generate two kinds of excitons: (1) B excitons and (2) hot excitons in the A band. Relaxation to A may occur by interband transitions of B excitons or intraband transitions of hot A excitons. Either will lead to the GSB, SE, and ESA shown in the ee  $\rightarrow$

$e'e'$  population transfer pathways of Figure 11.12. This relaxation must occur on the time scale of our pulse-width since the cross-peak asymmetry is observed even during temporal overlap. We believe that intraband relaxation of hot A excitons is the main factor in breaking the symmetry between AB and BA cross-peaks. Figure 11.10 shows that  $B \rightarrow A$  interband relaxation occurs on a longer time scale. The B/A ratio is higher when  $\omega_2$  is resonant with the B excitonic transition than when  $\omega_2$  is lower than the A exciton frequency (the top subplot). If population transfer of holes from the B to A valence bands occurred during temporal overlap, the B/A ratio would be independent of pump frequency at  $\tau_{21} < 0$ .

Figure 11.13 shows the delay transients at the different frequencies shown in the 2D spectrum. The colors of the dots on the 2D frequency-frequency spectrum match the colors of the transients. The transients were taken with a smaller step size and a longer time scale than the delay space explored in the 3D data set. The transients are quite similar. Our data are consistent with both monomolecular biexponential and bimolecular kinetic models and cannot discriminate between them. We have fit the decay kinetics to a single exponential model with a time constant of 680 fs and an offset that represents the long time decay. The 680 fs decay is similar to previously published pump-probe and transient absorption experiments. [NieZhaogang2014a, SunDezheng2014a, DochertyCallumJ2014a]

The spectral features change quantitatively for delay times near temporal overlap. Figure 11.14 shows a series of 2D spectra for both positive and negative  $\tau_{21}$  delay times with  $\tau_{22'} = 0$ . Each spectrum is normalized to its brightest feature. The spectra at positive  $\tau_{21}$  delay times become rapidly weaker as the delay times become more positive until the features vanish into the noise at +120 fs. The spectra also develop more diagonal character as the delay time moves from negative to positive values. The AB cross-peak is also a strong feature in the spectrum at early times.

The pulse overlap region is complicated by the multiple Liouville pathways that must be considered. Additionally, interference between scattered light from the  $\omega_1$  excitation beam and the output signal becomes a larger factor as the FWM signal decreases. Figure 11.15 shows the  $\omega_1$ ,  $\omega_2$ , and  $\omega_{2'}$  time ordered pathway that becomes an important consideration for positive  $\tau_{21}$  delay times. Since  $\tau_{22'} = 0$ , the initial  $\omega_1$  pulse creates an excited-state coherence, while the subsequent  $\omega_2$  and  $\omega_{2'}$  pulses create the output coherence. The output signal is only important at short  $\tau_{21} > 0$  values because the initially excited coherence dephases very rapidly. When  $\omega_1 \neq \omega_2$ , the first two interactions create an  $e'e'$  zero

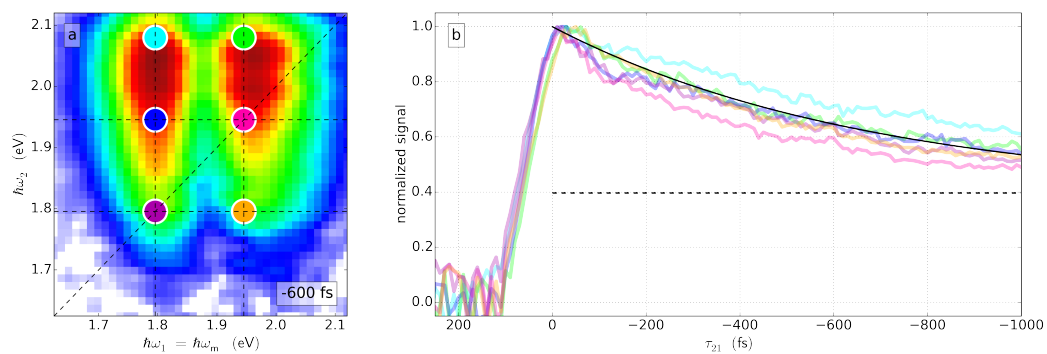


Figure 11.13: Transients taken at the different  $\omega_1$  and  $\omega_2$  frequencies indicated by the colored markers on the 2D spectrum. The dynamics are assigned to a 680 fs fast time constant (black solid line) and a slow time constant represented as an unchanging offset over this timescale (black dashed line).

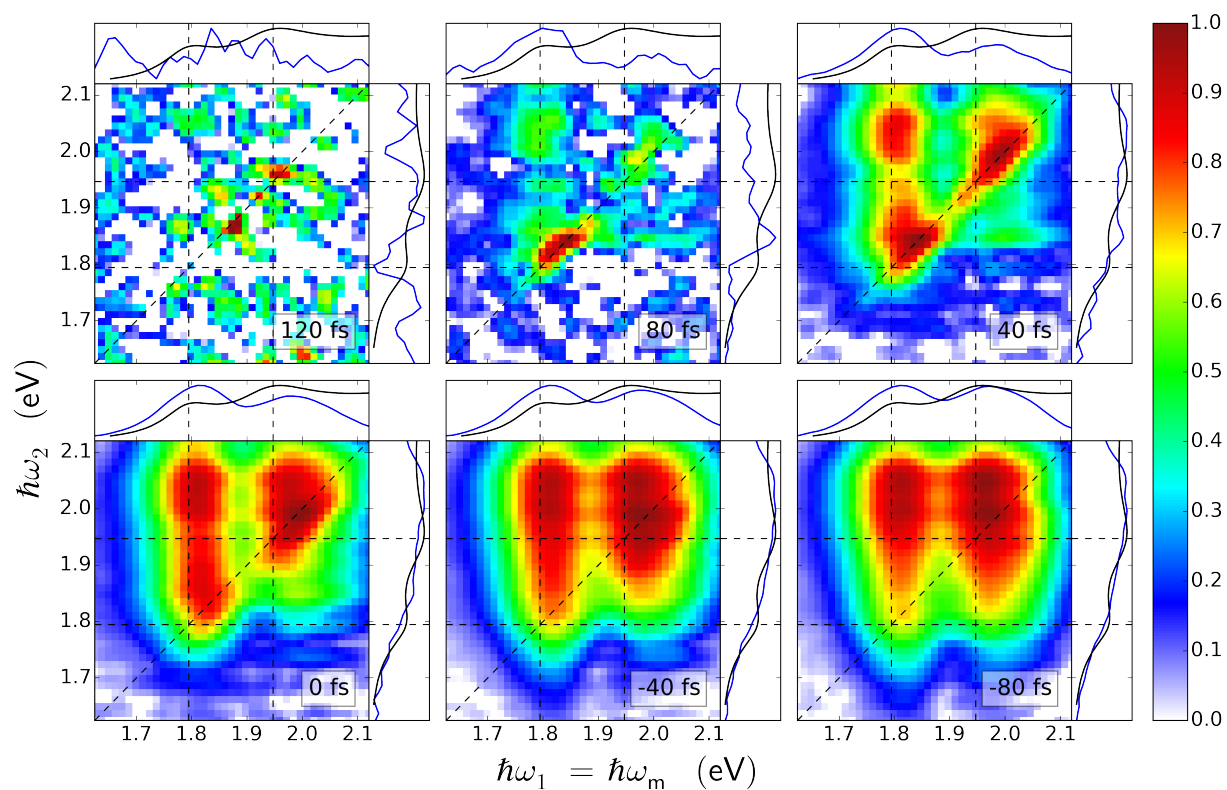


Figure 11.14: 2D frequency-frequency spectra near zero  $\tau_{21}$  delay times. The signal amplitude is normalized to the brightest features in each spectrum.

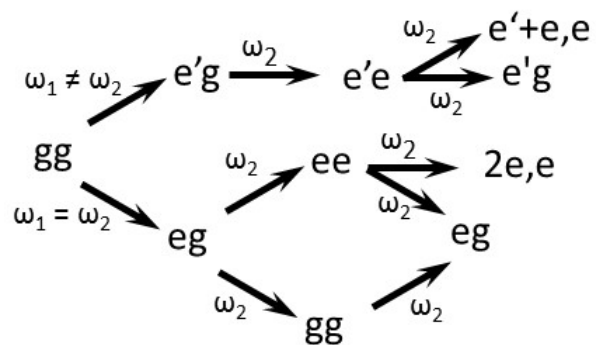


Figure 11.15: Liouville pathways for the  $\omega_1$ ,  $\omega_2$ , and  $\omega_2'$  time ordering of pulse interactions.  $e$  and  $e'$  represent either A or B excitonic states.

quantum coherence that also dephases rapidly. However, when  $\omega_1 = \omega_2$ , the first two interactions create an ee, gg population difference that relaxes on longer time scales. The resulting signal will therefore appear as the diagonal feature in Figure 11.14 (e.g., see the +40 fs 2D spectrum). In addition to the diagonal feature in Figure 11.14, there is also a vertical feature when  $\omega_1$  is resonant with the A excitonic transition as well as the AB cross-peak. These features are attributed to the pathways in Figure 11.12. Although these pathways are depressed when  $\tau_{21} > 0$ , there is sufficient temporal overlap between the  $\omega_2$ ,  $\omega_2'$ , and  $\omega_1$  pulses to make their contribution comparable to those in Figure 11.15. More positive values of  $\tau_{21}$  emphasize the Figure 11.15 pathways over the Figure 11.12 pathways, accounting for the increasing percentage of diagonal character at increasingly positive delays.

## 11.4 Conclusions

This paper presents the first coherent multidimensional spectroscopy of MoS<sub>2</sub> thin films. CMDS methods are related to the earlier ultrafast pump-probe and transient absorption methods since they all share bleaching, stimulated emission, Pauli blocking, and excited-state absorption pathways, but they differ in how these pathways define the spectra. In addition, CMDS methods have many additional pathways that become important when the coherence dephasing times are longer than the excitation pulse widths. In this work, the dephasing times are short so the pathways are identical to transient absorption. This work reports the first frequency-frequency-delay spectra of MX<sub>2</sub> samples. These spectra are complementary to previous work because they allow a direct comparison between the initially excited excitonic states and the states creating the final output coherence. The spectra show that the same hot A and B exciton continuum states that are observed in the absorption spectrum also dominate the CMDS excitation spectra. They also show that rapid,  $\sim 70$  fs intraband relaxation occurs to create the band-edge A and B excitonic features observed in the CMDS spectrum. The relative intensity of the diagonal peak features depends on the relative absorption strength of the A and B excitons. The relative intensity of cross-peak features in the 2D spectra depends on the excitation frequency. Excitation at or above the B exciton feature creates strong cross-peaks associated with hot A and B excitons that undergo ultrafast intraband population transfer. Excitation below the B excitonic feature creates a weak cross-peak indicating A-induced B-state bleaching but at a lower signal level corresponding to the lower optical density at this

energy. Population relaxation occurs over  $\approx 680$  fs, either by transfer to traps or by bimolecular charge recombination.

These experiments provide the understanding of MoS<sub>2</sub> coherent multidimensional spectra that will form the foundation required to measure the dynamical processes occurring in more complex MoS<sub>2</sub> and other TMDC heterostructures with quantum-state resolution. The frequency domain based multiresonant CMDS methods described in this paper will play a central role in these measurements. They use longer, independently tunable pulses that provide state-selective excitation over a wide spectral range without the requirement for interferometric stability.



## Chapter 12

# PEDOT:PSS

### 12.1 Introduction

Poly(3,4-ethylenedioxythiophene)-poly(styrenesulfonate) (PEDOT:PSS) is a transparent, electrically conductive (up to  $4380 \text{ S cm}^{-1}$  [KimNara2013a]) polymer. It has found widespread use as a flexible, cheap alternative to inorganic transparent electrodes such as indium tin oxide.

As a polymer, PEDOT:PSS implicitly contains a large amount of structural inhomogeneity. On top of this, PEDOT:PSS is a two component material, composed of PEDOT (low molecular weight, p-doped, highly conductive) and PSS (high molecular-weight, insulating, stabilizing). These two components segment into domains of conductive and non-conductive material, leading to even more structural inhomogeneity. Nonlinear spectroscopy may be able to shed light on the microscopic environment of electronic states within PEDOT:PSS.

### 12.2 Background

Complex microstructure:

1. PEDOT oligomers (6—18-mers)

2. these oligomers  $\pi$ -stack to form small nanocrystalites, 3 to 14 oligomers for pristine films to as many as 13—14 oligomers for more conductive solvent treated films
3. nanocrystalites then arrange into globular conductive particles in a pancake-like shape
4. these particles themselves are then linked via PSS-rich domains and assembled into nanofibril geometry akin to a string of pearls
5. nanofibrils interweave to form thin films, with PSS capping layer at surface

Prior spectroscopy (absorption anisotropy, X-ray scattering, conductivity).

Broad in the infrared due to midgap states created during doping from charge-induced lattice relaxations. These electronic perturbations arise from injected holes producing a quinoidal distortion spread over 4-5 monomers of the CP aromatic backbone, collectively called a polaron. Energetically favorable to be spin-silent bipolaron.

## 12.3 Methods

PEDOT:PSS (Orgacon Dry, Sigma Aldrich) was dropcast onto a glass microscope slide at 1 mg/mL at a tilt to ensure homogeneous film formation. The sample was heated at 100 °C for ~15 min to evaporate water.

An ultrafast oscillator (Spectra-Physics Tsunami) was used to prepare ~35 fs seed pulses. These were amplified (Spectra-Physics Spitfire Pro XP, 1 kHz), split, and converted into 1300 nm 40 fs pulses using two separate optical parametric amplifiers (Light Conversion TOPAS-C): “OPA1” and “OPA2”. Pulses from OPA2 were split again, for a total of three excitation pulses:  $\omega_1$ ,  $\omega_2$  and  $\omega_{2'}$ . These were passed through motorized (Newport MFA-CC) retroreflectors to control their relative arrival time (“delay”) at the sample:  $\tau_{21} = \tau_2 - \tau_1$  and  $\tau_{22'} = \tau_2 - \tau_{2'}$ . The three excitation pulses were focused into the sample in a 1° right-angle isocetes triangle, as in the BOXCARS configuration. [EckbrethAlanC1978a] Each excitation beam was 67 nJ focused into a 375  $\mu\text{m}$  symmetric Gaussian mode for an intensity of 67  $\mu\text{J}/\text{cm}^2$ . A new beam, emitted coherently from the sample, was isolated with apertures and passed into a monochromator (HORIBA Jobin Yvon MicroHR, 140 mm focal length) with a visible grating (500 nm blaze 300 groves per mm). The monochromator was set to pass all colors (0 nm, 250  $\mu\text{m}$

slits) to keep the measurement impulsive. Signal was detected using an InSb photodiode (Teledyne Judson J10D-M204-R01M-3C-SP28). Four wave mixing was isolated from excitation scatter using dual chopping and digital signal processing.

## 12.4 Transmittance and reflectance

Figure 12.1 shows the transmission, reflectance, and extinction spectrum of the thin film used in this work.

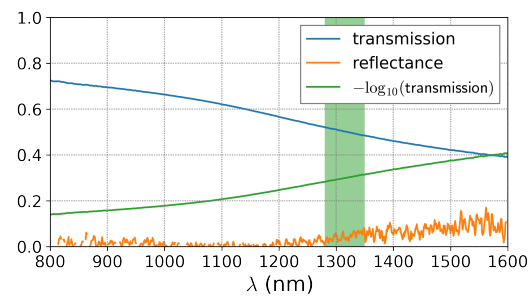


Figure 12.1: Thin film spectra. Transmission, reflectance, and extinction spectrum of the thin film used in this work. Extinction is  $\log_{10}(\text{transmission})$ .

## 12.5 Three-pulse echo spectroscopy

Two dimensional  $\tau_{21}, \tau_{22'}$  scans were taken for two phase matching configurations: (1)  $k_{\text{out}} = k_1 - k_2 + k_{2'}$  (3PE) and (2)  $k_{\text{out}} = k_1 + k_2 - k_{2'}$  (3PE\*). The rephasing and nonrephasing pathways exchange their time dependence between these two configurations. Comparing both pathways, rephasing-induced peak shifts can be extracted as in 3PE. [CITE] All data was modeled using numerical integration of the Liouville-von Numann equation.

Continuously variable ND filters (THORLABS NDC-100C-4M, THORLABS NDL-10C-4) were used to ensure that all three excitation pulse powers were equal within measurement error.

Figure 12.2 diagrams the phase matching mask used in this set of experiments.

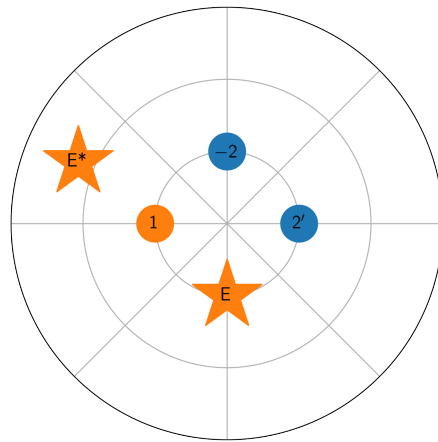


Figure 12.2: Phase matching mask used in this experiment. Each successive ring subtends 1 degree, such that the excitation pulses are each angled one degree relative to the mask center. The two stars mark the two output poyntings detected in this work.

Figure 12.3 shows the ten raw 2D delay-delay scans that comprise the primary dataset described in this section. The rows correspond to the two phase matching conditions, as labeled.

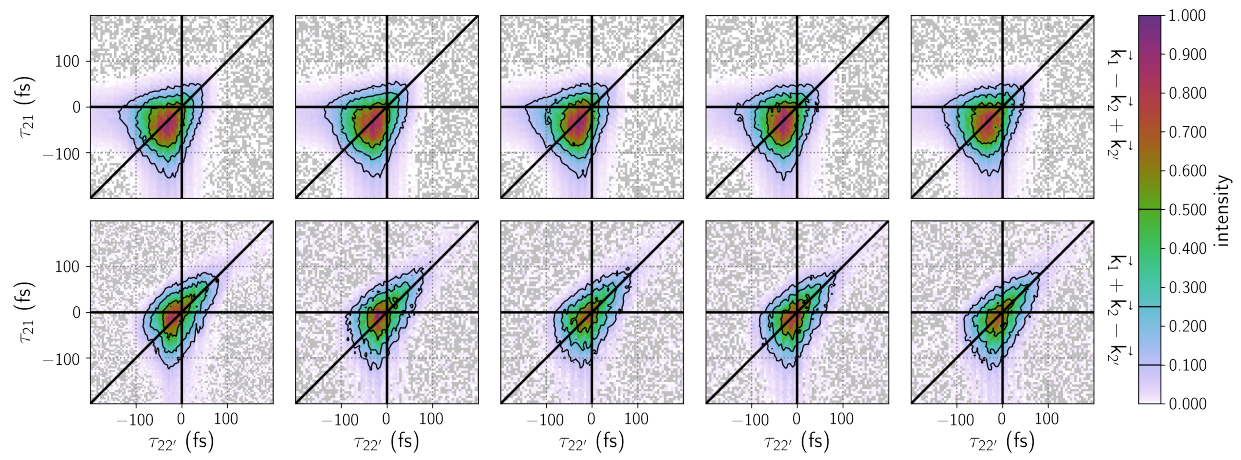


Figure 12.3: CAPTION TODO



### 12.5.1 Assignment of zero delay

The absolute position of complete temporal overlap of the excitation pulses (zero delay) is a crucial step in determining the magnitude of the peak shift and therefore the total rephasing ability of the material. The strategy for assigning zero delay relies upon the intrinsic symmetry of the two-dimensional delay space. Figure 12.4 labels the six time-orderings (TOs) of the three pulses that are possible with two delays. The TO labeling scheme follows from a convention first defined by Meyer, Wright and Thompson. [CITE] [CITE] first discussed how these TOs relate to traditional 3PE experiments. Briefly, spectral peak shifts into the rephasing TOs III and V when inhomogeneous broadening creates a photon echo in the III and V rephasing pathways colored orange in Figure 12.4. For both phase-matching conditions, there are two separate 3PE peak shift traces (represented as black arrows in Figure 12.4), yielding four different measurements of the photon echo. Since both 3PE and 3PE\* were measured using the same alignment on the same day, the zero delay position is identical for the four photon echo measurements. We focus on this signature when assigning zero delay—zero is correct only when all four peak shifts agree. Conceptually, this is the two-dimensional analogue to the traditional strategy of placing zero such that the two conjugate peak shifts (3PE and 3PE\*) agree. [CITE]

We found that the 3PEPS traces agree best when the data in Figure 12.3 is offset by 19 fs in  $\tau_{22'}$  and 4 fs in  $\tau_{21}$ . Figure 12.5 shows the 3PEPS traces after correcting for the zero delay value. The entire 3PEPS trace ( $\tau$  vs  $T$ ) is shown for regions I, III (purple and light green traces) and V, VI (yellow and light blue traces) for the [PHASE MATCHING EQUATIONS] phase matching conditions, respectively. Peak-shift magnitudes were found with Gaussian fits on the intensity level, in accordance with 3PEPS convention. [CITE] The bottom subplot of Figure 12.6 shows the agreement between the four traces for  $T > 50$  fs where pulse-overlap effects become negligible. These pulse-overlap effects cause the 3PEPS at small  $T$  even without inhomogeneous broadening. [CITE] At long  $T$ , the average static 3PEPS is 2.5 fs.

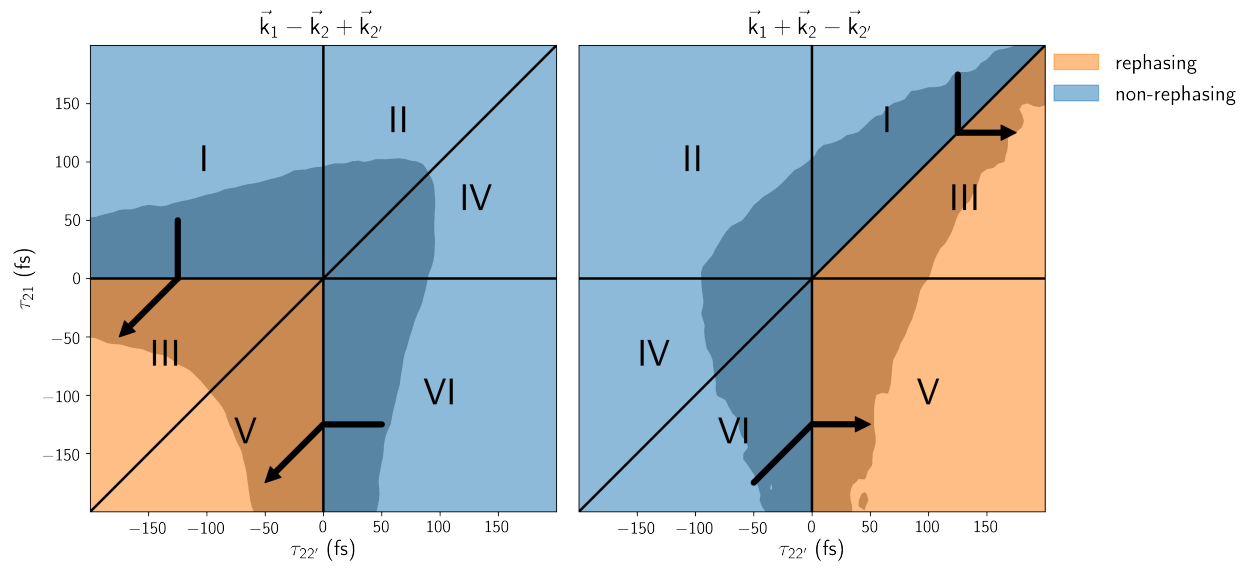


Figure 12.4: CAPTION TODO

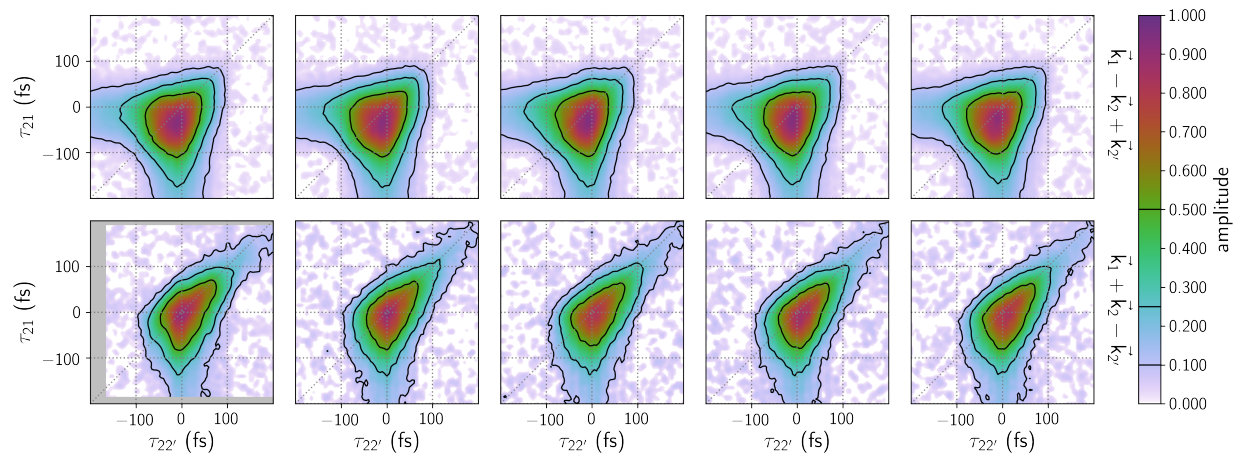


Figure 12.5: CAPTION TODO

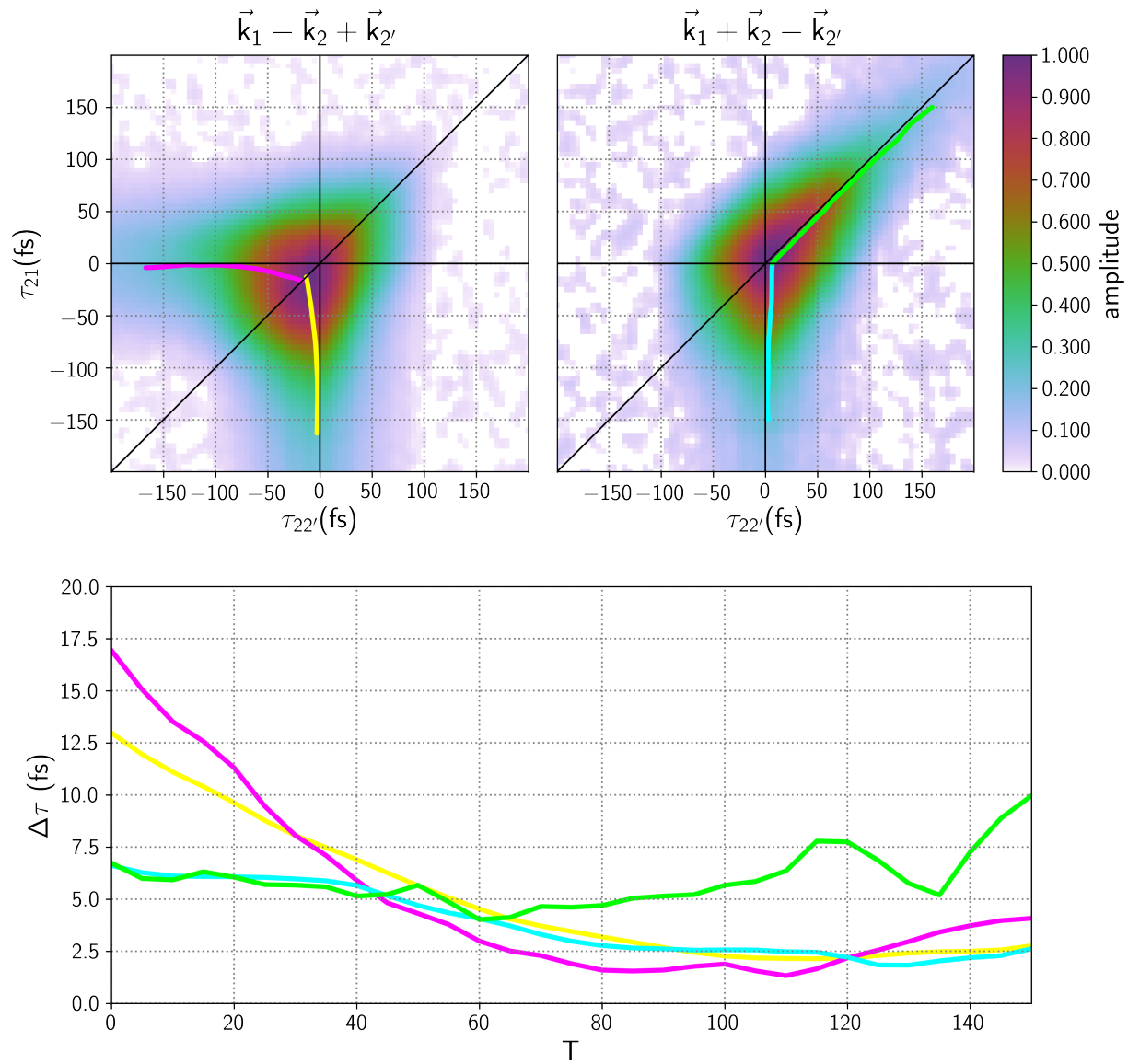


Figure 12.6: CAPTION TODO

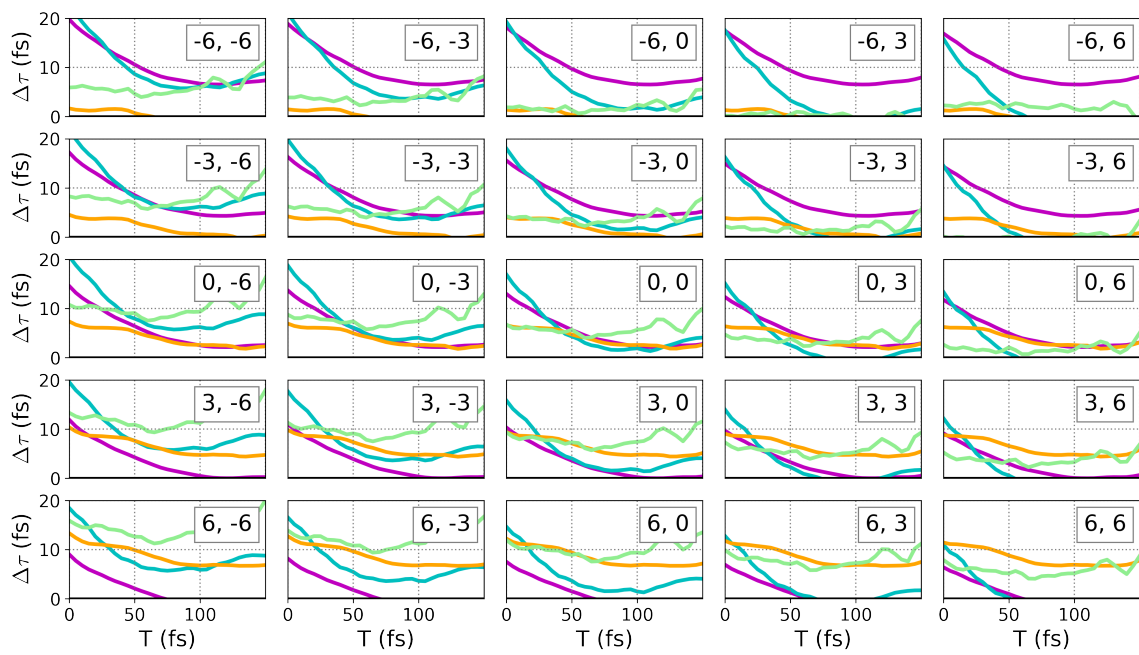


Figure 12.7: CAPTION TODO

There is a deviation of the TO I-III 3PEPS\* trace (green line) from the other traces. It is attributed to a combination of excitation pulse distortions and line shape differences between OPA1 and OPA2 (see Figure 12.1) and small errors in the zero delay correction. Figure 12.7 shows what the four 3PEPS traces would like like for different choices of zero-delay. The inset numbers in each subplot denote the offset (from chosen zero) in each delay axis.

### Numerical model

We simulated the 3PEPS response of PEDOT:PSS through numerical integration of the Liouville-von Neumann Equation. Integration was performed on a homogeneous, three-level system with coherent dynamics described by

$$\frac{1}{T_2} = \frac{1}{2T_1} + \frac{1}{T_2^*}, \quad (12.1)$$

where  $T_2$ ,  $T_1$  and  $T_2^*$  are the net dephasing, population relaxation, and pure dephasing rates, respectively. A three-level system was used because a two-level system cannot explain the population relaxation observed at long populations times,  $T$ . This slow decay may be the same as the slowly decaying optical nonlinearities in PEDOT:PSS. [CITE] Inhomogeneity was incorporated by convolving the homogeneous response with a Gaussian distribution function of width  $\Delta_{\text{inhom}}$  and allowing the resultant polarization to interfere on the amplitude level. This strategy captures rephasing peak shifts and ensemble dephasing.

It is difficult to determine the coherence dephasing and the inhomogeneous broadening using 3PE if both factors are large. To extract  $T_2^*$  and  $\Delta_{\text{inhom}}$ , we focused on two key components of the dataset, coherence duration and peak shift at large  $T$ . Since dephasing is very fast in PEDOT:PSS, we cannot directly resolve an exponential free induction decay (FID). Instead, our model focuses on the FWHM of the  $\tau$  trace to determine the coherence duration. At  $T > 50$  fs, the transient has a FWHM of  $\sim 80$  fs (intensity level). For comparison, our instrumental response is estimated to be 70-90 fs, depending on the exact value of our pulse duration  $\Delta_t$  (35-45 fs FWHM, intensity level). An experimental peak shift of 2.5 fs was extracted using the strategy described above. Taken together, it is clear that both pure dephasing and ensemble dephasing influence FWHM and peak shift so it is important to find value of

$T_2^*$  and  $\Delta_{\text{inhom}}$  that uniquely constrain the measured response.

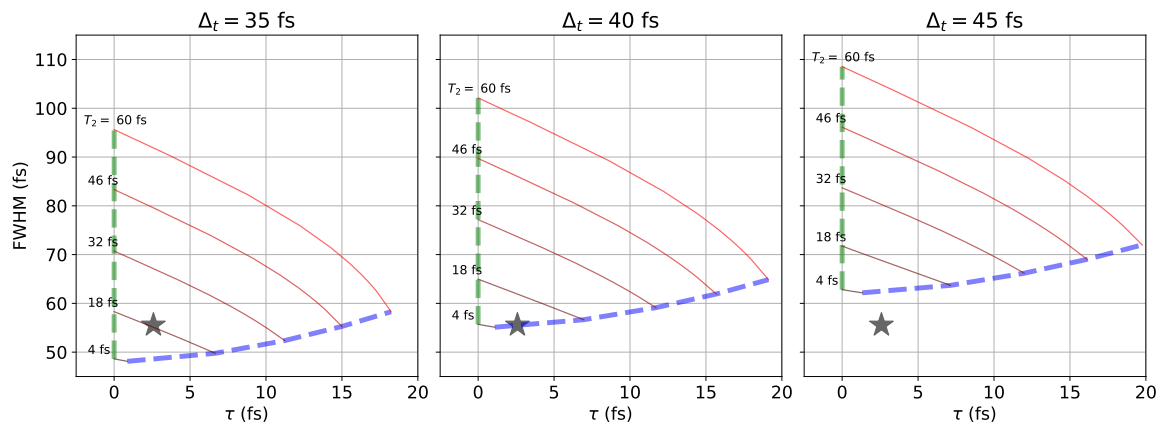


Figure 12.8: CAPTION TODO



We simulated the  $\tau$  trace for a variety of  $\Delta_{\text{inhom}}$  and  $T_2$  values. The results for  $\Delta_t = 40$  fs are summarized in Figure 12.8. The lines of constant  $T_2$  span from  $\Delta_{\text{inhom}} = 0$  (green left ends of curves) to the limit  $\Delta_{\text{inhom}} \rightarrow \infty$  (blue right ends of curves). The lines of constant  $T_2$  demonstrate that ensemble dephasing reduces the transient duration and introduces a peak shift. The influence of inhomogeneity on the observables vanishes as  $T_2 \rightarrow \infty$ .

We performed simulations analogous to those in Figure 12.8 for pulse durations longer and smaller than  $\Delta_t = 40$  fs. Longer pulse durations create solutions that do not intersect our experimental point (see right-most subplot of Figure 12.8), but shorter pulse durations do. [TABLE] summarizes the coherence dephasing time and inhomogeneous broadening values that best matches the experimental FWHM and inhomogeneous broadening value for  $\Delta_t = 35, 40$  and  $45$  fs. Clearly, there is no upper limit that can provide an upper limit for the inhomogeneous broadening.

$\Delta_t$ (fs)	$T_2$ (fs)	$\hbar T_2^{-1}$ (meV)	$\Delta_{\text{inhom}}$ (meV)
45	—	—	—
40	10	66	$\infty$

Table 12.1: CAPTION TODO

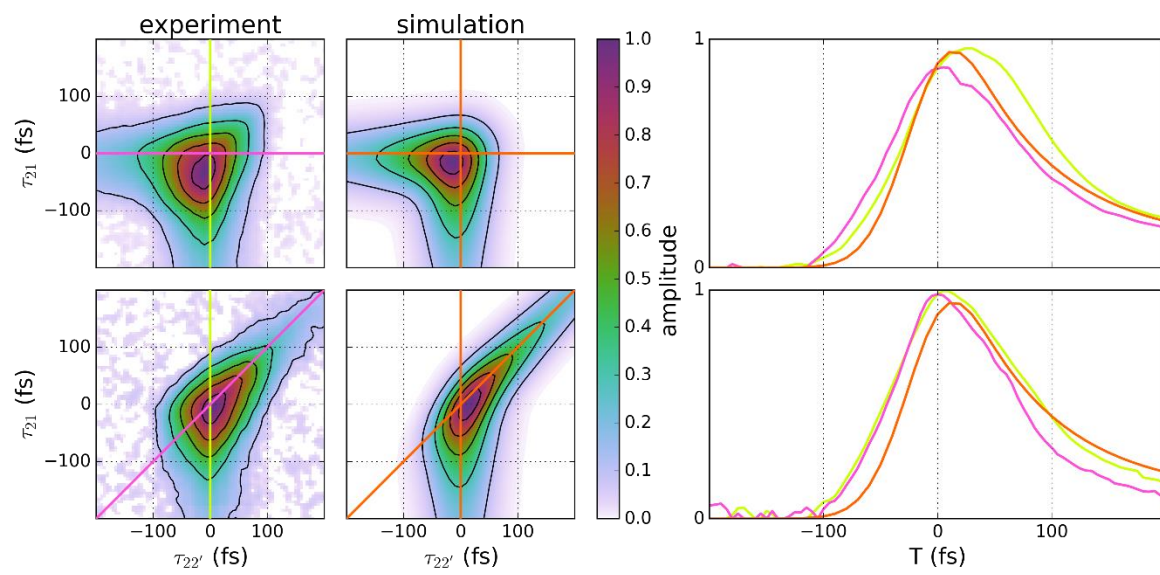


Figure 12.9: CAPTION TODO

Our model system does an excellent job of reproducing the entire 2D transient within measurement error (Figure 12.9). The most dramatic disagreement is in the upper right, where the experiment decays much slower than the simulation. Our system description does not account for signal contributions in TOs II and IV, where double quantum coherence resonances are important. In addition, excitation pulse shapes may cause such distortions. Regardless, these contributions do not affect our analysis.

Extremely fast (single fs) carrier scattering time constants have also been observed for PEDOT-base conductive films. [CITES]

## **12.6 Frequency-domain transient grating spectroscopy**

This section describes preliminary, unpublished work accomplished on PEDOT:PSS.

## Chapter 13

# Pyrite



## Chapter 14

# BiVO<sub>4</sub>

pass





## **Part IV**

# **Appendix**



# Appendix A

## Public

### A.1 Chemical systems

Chemical systems are complex! They contain many molecules ( $10^{25}$  in a cup of coffee, 1 trillion in each human cell). These molecules have multiple interaction modes, both internal (intramolecular) and external (intermolecular). The reactivity of the system taken as a whole can be dominated by very rare but very important species, *e.g.* catalysts.

Despite this complexity, scientists have gotten very good at describing chemical systems through representations of dynamic equilibrium. In such situations, several key parameters emerge:

- concentration
- timescale (rate)
- lengthscale

### A.1.1 Concentration

### A.1.2 Timescale

### A.1.3 Lengthscale

## A.2 Analytical chemistry

Traditionally, chemists have seen fit to divide themselves into four specializations: analytical, inorganic, organic, and physical. In recent years, materials chemistry and chemical biology have become specializations in their own right. This dissertation focuses on analytical chemistry.

Analytical chemists separate, identify, and quantify chemical systems. To do this, we build instruments that exploit physical properties of the chemical components:

- separation science (chromatography, electrophoresis)
- mass spectrometry
- electrochemistry
- microscopy
- spectroscopy

Spectroscopy is a family of strategies that exploit the interaction of chemical systems with light.

## A.3 Spectroscopy

Molecules respond to electric fields. Static electric fields cause charged molecules (ions) to move, as in electrophoresis and mass spectrometry. Oscillating electric fields, also known as light, can interact directly with the molecules themselves, driving transitions. However, these transitions can only be driven

with the appropriate frequency of light (resonance). Different frequencies (colors) of light interact with different kinds of transitions, revealing different features of the molecule of interest.

### A.3.1 Nonlinear spectroscopy

Spectroscopy is fantastic, but sometimes simple experiments don't reveal everything. Nonlinear spectroscopy uses multiple electric fields simultaneously, revealing even more information about the chemical system.

## A.4 Instrumentation

To accomplish nonlinear spectroscopy, specialized light sources are needed:

- gigantic electric fields
- ultrafast time resolution
- tunable frequencies

### A.4.1 LASER

These sources are made using Light Amplified by the Stimulated Emission of Radiation (LASER).

By keeping a wide range of colors in phase simultaneously, we are able to create truly ultrafast pulses of light. The work presented in this dissertation was primarily taken using a 35 fs 1 KHz system.

35 fs ( $35 \times 10^{15}$  second) pulses are incredibly short:

$$\frac{\text{pulse duration (35 fs)}}{\text{time between pulses (1 ms)}} \approx \frac{5.75 \text{ months}}{\text{age of universe (13.7 billion years)}} \quad (\text{A.1})$$

proportionally, our sample spends 6 months in the "sun" for every age of the universe in the dark.

Because all of the energy within the pulse is compressed to such a short period of time, these pulses are also incredibly powerful:

$$\frac{\text{energy per pulse (4 mJ)}}{\text{pulse duration (35 fs)}} \approx \frac{\text{US electricity generation}(5.43 \times 10^{11} \text{ W})}{5} \quad (\text{A.2})$$

this laser outputs electric fields one fifth as powerful as total US electricity generation (2016).

#### **A.4.2 OPA**

## **Appendix B**

# **Procedures**

## B.1 “Six-month” maintenance

The laser system that the Wright Group’s MR-CMDS instruments use requires regular maintenance. Each component is sensitive to lab conditions such as temperature, humidity, and vibrations. Small deviations in upstream components can cause large problems in downstream optics. Regular maintenance involves “tune-up” of upstream components so that upstream lasers function well and ideally couple into downstream lasers.

Historically, the Wright Group has engaged in reactive maintenance: a “fix it if it’s broken, don’t touch otherwise” kind of approach. This approach makes a lot of sense for instruments that are quick to fix, and have few active users.

I instituted a proactive, regular maintenance procedure (described below) that has improved the predictability of instrumental performance. Predictability is key for instruments with multiple users.

Supplies needed:

1. 5 gallons distilled water.
2. Filters.
  - (a) 2x 5 micron Liquatec SDF-25-0505
  - (b) 2x 20 micron general purpose water filter (sold in stockroom)
3. Nalco fluids.
  - (a) 4 gallons Nalco 460-PCCL104 (the pink stuff).
  - (b) 1 gallon Nalco 460-CCL2567 (the clear stuff).
4. 150x 5 mg activated charcoal packets (Newport Part # 90035762)

Procedure:

1. Turn off all lasers in lab.
2. In no particular order:
  - (a) Computers in lab.
    - i. Backup contents.
    - ii. Uninstall unnecessary software.
    - iii. Update all necessary software.
    - iv. Restart.
  - (b) Chiller maintenance.
    - i. See x
    - ii. See y
    - iii. See z
  - (c) Lab cleaning.



- i. Mop the floor, trying to get as much dust as possible. Sweeping in the laser lab is discouraged, because it knocks more dust into the air and onto the lasers.
  - ii. Take out trash.
  - iii. Empty homeless cables box.
  - iv. Empty homeless screws box.
  - v. Organize any cabling mess.
  - vi. Remove unused components (optics, electronics, cabling, etc) from laser tables and surroundings. Place into appropriate locations.
  - vii. Organize optics cabinet.
  - viii. Organize electronics bench.
3. Let lab sit overnight to allow dust to settle and the air to dehumidify.
4. Start up system again.
  - (a) TODO

## B.2 Lytron Kodiak RC006

We have one Lytron Kodiak RC006: Model Number RC006G03BB1C002, Serial Number 739383-02.

Regular chiller maintenance:

1. Gather supplies.
  - (a) 1 gallon distilled water (do not use deionized)
  - (b) 1 gallon Nalco 460-PCCL104 (the pink stuff)
2. Drain system completely.
  - (a) Turn off chiller.
  - (b) Break tubing at push-to-connect, plugging return.
  - (c) Allow chiller to run until liquid stops flowing. You will get a pressure error, ignore (silence) it.
  - (d) Use tube to mouth-syphon remaining liquid from within chiller
  - (e) Reconnect at push-to-connect
3. Fill chiller with distilled water (should require  $\approx$ 1 gallon), let run for 30 minutes.
4. Drain system again.
5. Replace filter.
6. Fill system with one gallon Nalco 460-PCCL104 (the pink stuff).
7. Turn chiller on, top-off with distilled water.
8. Record maintenance, order new supplies for next time if necessary.

In the past we have had trouble with low flow errors upon system startup. These seem to have been fixed by adding a “high” flow loop connecting the outlet and inlet of the chiller. Ideally the pressure drop across this loop is sufficient to still drive fluid through the laser.

## B.3 PolyScience 6000 Series

We own two PolyScience chillers—different models but functionally equivalent.

Grey: Serial Number 3E1161245

White and Blue: Serial Number 4K1050550

Regular chiller maintenance:

1. Gather supplies.
  - (a) Filter (sold in stockroom).
  - (b) 1 gallon Nalco 460-PCCL104 (the pink stuff).
2. Drain system completely.
  - (a) Disconnect red water line and allow chiller to pump water out.
  - (b) Push nipple of male end with flat object to release check valve.
3. Check filters.
  - (a) If air filter dirty, wash with water (let dry after washing).
  - (b) If water filter is dirty, replace.
4. Reassemble.
  - (a) Fill with Nalco 460-PCCL104 (the pink stuff).
  - (b) Turn on, top-off with distilled water.

## B.4 NesLab Merlin M33

We have one NesLab Merlin M33 Chiller, Serial Number 106227049.

This chiller serves four different lasers on the ultrafast system. The cycle goes chiller out → Millennia → Tsunami → Spitfire Ace → Spitfire Pro → chiller return.

Regular chiller maintenance

1. Gather supplies.
2. Drain system completely.
3. Clean chiller internals.
4. Disconnect tubing, plug return.
5. Remove old filter from chiller, discard, replace filter holder.
6. Drain system completely and flush with several gallons of distilled water (should require 2), until no suds are formed as new water goes through system.
7. Fill system with one gallon distilled water, circulate for at least 15 minutes, then drain completely.
8. Place new filter into chiller.
9. Reconstruct tubing to include lasers in cycle. Ensure that cycle direction is correct.
10. Fill system with one gallon Nalco 460-PCCL104 (the pink stuff).
11. Turn chiller on, and allow system to flow for a while to get air bubbles out.
12. Top off with distilled water until chiller and tubing is full.

## B.5 Calibrating the 407A

Calibrating the 407.A

You may sometimes notice that the zero position changes dramatically from sensitivity to sensitivity with the 407A. If this happens, iterate through the following until zero stays consistent:

Use the fine adjust (knob on side) to zero the 407A on the highest sensitivity

Use the front adjust (flathead screwdriver needed) to zero on the lowest sensitivity

## B.6 Millennia

### B.6.1 Startup

The Millennia has problems with ‘thermal runaway’ upon startup if a user naively sends the laser to 4.0 W in power mode (thermal runaway causes the infamous FAULT 146 system shut off: power adjust timeout error). The following procedure wakes the Millennia up gently enough to prevent thermal runaway. It assumes that the Millennia starts completely shutdown and cold.

1. Check desiccant inside Millennia, replace if pink.
2. Ensure that Millennia shutter is closed such that no light is going downstream.
3. Flip orange power switch on diode box.
4. Wait for system to warm up (~30 minutes).
  - (a) “System Warming Up” message should appear on control box.
  - (b) Warm-up is finished when percentage complete indicator reaches 100.
  - (c) The Millennia will start in SP Current mode.
5. Record diode hours (choose “Info”, scroll down).
6. Turn Millennia to 1.0 W in “power mode”, wait for equilibration.
  - (a) Equilibration occurs when diode temperature and current are stable (within 0.1) over 5 minutes.
7. Switch Millennia to “current mode”.
8. Slowly ramp current until you have more than 4 W output (probably ~70%).
9. Again, wait for diode temperature and current equilibration.
10. Switch Millennia to “power mode” at 4.0 W.
11. Ensure one last time that diode temperature and current are not changing over 5 minute timescale.
12. Measure and record actual Millennia output power, currents, temperatures.

### B.6.2 Toggling service mode

On the control board inside the laser, DIP switch #4 toggles service mode. Service mode unlocks special SP modes. These allow us to record things like Diode hours. Service mode can be buggy, so it’s best to leave the Millennia in normal Power mode during regular operation.

## B.7 Spitfire Pro

Only tune up the Spitfire if you need to, and do not treat it casually—set aside an entire day. Merely opening the spitfire box exposes the optics to dust. Treating the Spitfire with the respect it deserves will only save time in the long run.

The Spitfire contains 70 charcoal packets. These should be replaced every  $\sim 6$  months.

### B.7.1 Startup

Spitfire Pro startup procedure, from cold.

1. Ensure that the software is closed on control laptop.
2. Turn on Empower power supply (orange switch).
3. Turn on Timing and Delay Generator “TDG” (orange switch).
4. Turn on temperature control box (orange switch).
5. Turn key on Empower power supply.
6. Turn key on TDG.
7. Start Spitfire software.
  - (a) Often have many faults, most will clear immediately.
  - (b) Empower LBO temp fault may take a while to clear—normally clears after 5 minutes.
8. If Empower has been off (totally, or just at zero amps), warm up at 20 Amps for 1 hour.
  - (a) Use a *good* beam block to block entry into the Cavity during this time.

### B.7.2 Common alignment

#### Preparation

1. Check desiccant in temperature control box (blue is good, pink is bad).
2. Connect the fast oscilloscope so that you can see the pulse train.
3. If Spitfire is off, go through startup procedure.
4. If it has not been done in awhile, measure and record an Empower power curve.
5. Place the 407A after the telescope between the large square mirrors on the empty mount.
  - (a) This mount is dedicated for this purpose, and should be left in the Spitfire at all times.
6. Set Empower current such that the Empower is delivering  $\sim 20$  W to the crystal (refer to Empower power curve).

## Cavity and pump

The first goal in alignment will be to ensure that the cavity and pump are healthy without seeding (in ns-lasing mode). A well-aligned Spitfire will deliver 5 to 5.2 W to the 407A when pumped with 20 W. The idea of this procedure is to be minimally invasive, while demanding good performance from the laser. Do not move on to seeded operation until ns-lasing is healthy, but at the same time do not do more than you need to.

1. Switch to ns lasing mode.
  - (a) Block seed at output of stretcher.
    - i. Note that seed must still enter the stretcher with good enough alignment to defeat the bandwidth detector.
  - (b) Activate Pockels Cells 2 and 3—do not use Pockels Cell 1.
  - (c) Expect 20 to 30 ns (2 to 3 round trips) additional build-up time in ns operation.
    - i. Means you must change timing of Pockels Cell 3 when working in ns lasing mode.
    - ii. Operate the laser at its ideal switch out time when aligning ns lasing.
    - iii. Refer to the records to see if your switch-out time is unusual for recent performance.
2. Clean all green optics in order of light hitting them.
  - (a) You must get new spectrophotometric grade methanol for this cleaning.
3. Loop through the following until ns lasing delivers more than 5 W to the 407A.
  - (a) Check to ensure no optics are damaged, have dust on them etc.
  - (b) Clean optics. Check power after each cleaning—at the very least you don't want to lose power. When cleaning, wait at least a second before letting the light hit the optic after cleaning.
  - (c) Align pump.
    - i. Decrease the pump power to  $\sim 17$  A. This should decrease the ns lasing output to around 2 Watts, so you should be able to increase the sensitivity on the 407A if you wish.
    - ii. Find the ideal switch out (channel 3) time for this lower pump power. It will be still later than the aforementioned ns lasing switch out time. Back off the ideal ns switch out time by  $\sim 2$  round trips for optimization.
    - iii. Typically the two mirrors on either side of the cavity (immediate to the lenses) are the only pump mirrors touched during alignment. The first pump mirror may be touched in special cases but not for regular touch-up.
    - iv. Block the back reflection with the mirror mount when aligning the second pump mirror.
    - v. Align the back reflection mirror (without beam block).
    - vi. Iterate through the mirrors until you are satisfied that pump pointing is ideal.
  - (d) Align cavity.
    - i. Never touch anything except the two outermost end mirrors.
    - ii. Note that the alignment tool is poor to the cavity mode intentionally.



## Seed

Now that the cavity is good, you must couple the seed into it. If you have just aligned the oscillator you should wait at least 10 hours before attempting to align the seed.

Expect 100 to 150 mW less in seeded mode.

1. Remove stretcher cavity flange, being careful not to damage wires.
2. Align the two apertures either side of the Faraday isolator using mirrors external to Spitfire.
3. Align to two "A" mask positions in stretcher.
4. Align to three "F" mask positions on the way to cavity (this mirror system is under-constrained; consider using the final mirror of the "A" mask alignment as a tweaking mirror).
5. Let seed into cavity by turning on channel 1.
6. Optimize (mirror at D18 and periscope) to put out power before compressor—often useful to go one or two round trips less ( $\sim 210$  ns on channel 3) when aligning seed to power (output depends on seed more sensitively and you want to optimize for largest buildup reduction time).
7. Can adjust quarter waveplate to minimize post-pulsing if necessary but be very careful to not send the output back into the stretcher.
8. Ensure pulse is let out of the cavity at the optimal time (check oscilloscope and power).
9. Remove 407A.
10. Reconstruct flanges on stretcher cavity.

## Output

Now you must ensure that the cavity output is properly routed through the telescope and compressor before leaving the Spitfire.

Note that only  $\sim 80\%$  of the cavity output power transmits through the compressor due to absorbance in the grating and other losses.

1. Align to compressor positions (two "H") using backwards alignment tool. You will need to unplug the compressor stage cable—remember to plug back in.
2. If the cavity or pump was touched, consider aligning the compressor.

## Cleanup

1. Make sure you have taken all of your tools out of the laser.
2. Make sure you remembered to plug the compressor stage back in.
3. Wait at least 2 hours before moving on to downstream alignment—best to wait overnight if you

can. It's OK to make a first pass at rough alignment, but compression and pointing will probably change slightly as the laser equilibrates.

It's normal for the Spitfire output power change by 50 to 100 mW in the first days after alignment. After that initial change the Spitfire tends to be stable for weeks. During experiments it's a good idea to measure Spitfire output on a daily basis.

### **B.7.3 Stretcher alignment**

This is our current best strategy for stretcher alignment. Use caution and keep your brain in gear when working on this. Since we have not messed with the stretcher frequently this guide cannot be trusted blindly.

#### **Preparation**

1. Ensure that the Spitfire is off (no pump present in cavity, Pockels cells powered down).
2. Force upstream oscillator to go CW, adjust output color to be at center of mode-locked bandwidth.
3. Use external mirrors to align through Faraday isolator.
4. Use first two mirrors after isolator to alignment tool prior to stretcher grating.

#### **Adjustment**

1. Adjust the stretcher grating until the four dots are overlapped.
2. Use pickoff mirror after stretcher to get the beam to alignment tool.

### **B.7.4 Compressor alignment**

1. Use the first telescope mirror to align to the alignment tool before the first square mirror preceding the compressor.
2. Use the second telescope mirror to align to the alignment tool when place between the square mirrors preceding the compressor.

## B.8 TOPAS-C

### B.8.1 Common alignment

This section discusses common alignment operations that will probably need adjustment on a monthly basis to ensure ideal OPA behavior. All fs table users should feel comfortable performing these tuneups.

Tips and tricks:

1. As a rule of thumb, if you don't need light through the poweramp the light should be blocked to avoid hot spots and damage. The light should be blocked before M8.
2. Use a fluorescent card to visually get a better idea of the centering of the 800 nm beam through the apertures.
3. Align OPA1 before OPA2. For the sake of consistency, we have agreed that compression should be adjusted for OPA1 best performance. OPA2 will have to "live with" the compression that is best suited for OPA1.

### Preparation

1. Ensure that the Spitfire is working (between 3.8 and 4.0 W).
2. Ensure that the pump is not clipping on any mirrors between Spitfire and OPAs.
3. Inspect mode structure of pump for hot spots or diffraction. Clean any dust off of mirrors between Spitfire and OPAs.
4. Open OPA lid.
5. Set OPA to 1300 nm, ensure motors are homed.

### Preamp

1. Block pump into poweramp upstream of M8 using block of metal.
2. Open OPA shutter.
3. Ensure that the WL plate is not drilled—look for "sparking". This takes an experienced eye—ask if you have a hard time deciding. If drilled, rotate the WL plate.
4. Ensure that input poynting and compression are good for the preamp by iterating through the following adjustments. Stop iteration once all metrics are good without further adjustment.
  - (a) Iteratively align through A0 and A2. The orange-colored white light should go through A2.
  - (b) Ensure that your poynting changes have not introduced clipping on external mirrors.
  - (c) Ensure that white light is good.
    - i. If you are aligning OPA1, adjust compression such that WLG is maximized. Do not adjust compression to OPA2 WL.
    - ii. Adjust  $A_{WL}$  until WL is symmetric and stable.

- (d) Ensure that no OPG is present in C1.
- (e) Manually adjust D1 to maximize seed intensity.
- 5. Align seed down entire row of holes in-which L6, L7, DM2, NC2, and DM3 lie. Alignment is accomplished using M5 and M6.
  - (a) Consider blocking pump into C1 (passing only WL) to “toggle” the seed—this helps distinguish between orange WL and slightly redder seed.

## Poweramp

1. Unblock pump into poweramp.
2. Setup 407A power meter outside of OPA.
3. Adjust manual D2 until over 600 mW is achieved.
4. Put “Caution fs OPA free to coldwave” sign on laser-lab doors.
5. Remove all optics downstream of Mixer 3: filter periscopes (wavelength selectors), periscope, beam splitter, and beam dump.
6. Iterate the following until optimal power and collinearity are simultaneously reached:
  - (a) Adjust collinearity of three beams using DM2
    - i. All beams should be overlapped far away.
    - ii. Use surveyor’s telescope to observe beams.
  - (b) Maximize 407A-measured power using manual D2.
  - (c) Maximize 407A-measured power using M10.
7. Reassemble optics downstream of Mixer 3.
8. Close OPA lid.
9. Allow a minute for equilibration.
10. Measure and record power—should be over 600 mW.

## B.8.2 Full alignment

The following discussion endeavors to be as complete as possible. The goal is to have a procedure that produces a well-aligned OPA regardless of initial conditions. Experienced OPA users may find only pieces of this guide necessary to solve their particular problem.

## Preparation

1. Ensure that the spitfire is working well (between 3.8 and 4.0 W).
2. Ensure that the pump is not clipping on any mirrors between Spitfire and OPA.
3. Inspect mode structure of pump for hot spots or diffraction. Clean any dust off of mirrors between Spitfire and OPAs.
4. Open OPA lid.
5. Set OPA to 1300 nm, ensure motors are homed.

6. Block pump into poweramp upstream of M8 using block of metal.
7. Block seed between compensating crystal and M5.
8. Remove all side walls from OPA.

### Input poynting

Input poynting is adjusted to ensure good alignment through L1 and L2 into D1.

1. Remove A1/L3, VF,  $A_{WL}$ .
2. Place D2 at nominal position (45 degrees).
3. Using external mirrors, ensure that beam propagates through the alignment tool at the holes just after L2 and just before M1 (in D1).
4. Ensure that you have not introduced clipping external to the OPA.
5. Ensure that the L1/L2 telescope is outputting a collimated, undistorted beam.

### D1 alignment

1. If you haven't already, remove A1/L3, VF.
2. Ensure that you are blocking light between compensating crystal and M5.
3. Remove WLG plate, L4, TD, DM1, knife edge.
4. Set C1 to surface normal (should be 0 degrees if affix is set correctly in software.)
5. Using M1 and M2, ensure that beam propagates through the alignment tool at the holes just after M2 and just before M5.

### White light

1. Block preamp pump after M3 during this procedure.
2. Remove WL plate if it is present.
3. Replace/adjust AL/L3, adjusting focus to be at white light plate desired position.
4. Replace VF and  $A_{WL}$  if they are absent.
5. Replace the WL plate—ensure that the plate is normal to input beam by visual inspection.
6. Optimize WLG using VF,  $A_{WL}$ , and plate position.
  - (a) Begin with  $A_{WL}$  closed.
  - (b) Open  $A_{WL}$  10%.
  - (c) Adjust VF to just allow for onset of WLG.
  - (d) Adjust position of sapphire plate to maximize visible component of continuum.
  - (e) Adjust VF to attenuate WLG pump to lowest WLG threshold where central mode and first outer rings are visible.
  - (f) Adjust compression for WLG symmetry.
  - (g) Continue to open  $A_{WL}$  and adjust VS until  $A_{WL}$  is as open as possible and VF is as dark as possible (while maintaining stable WLG).

7. Replace / adjust L4.
  - (a) Remove DM1 if it is present.
  - (b) Adjust L4 so that the visible component of the WL continuum is focused on A2. This will ensure that the NIR component focuses at NC1.
  - (c) Ensure that the WL remains centered on the alignment tool / A2.
    - i. L4 may be rotated to adjust height.
  - (d) Replace DM1.

### Preamp pump

1. Remove L5, M4.
2. Adjust M3 to alignment tool holes near edge of OPA to M5 mount. Note that M3 may be rotated to change height.
3. Ensure that beam is passing through alignment tool near M3. If not, consider translating M3 or moving BS2. Before making these adjustments ensure that the beam is true into BS2 (see input poynting section above).
4. Replace L5. Ensure that beam through L5 is on-axis with alignment tool in far field.
5. Replace M4. Point pump so that it intersects with the first red ring in the WL at DM1.
6. Adjust DM1 to spatially overlap pump with WL in NC1.
7. Adjust L5 so pump focus in in C1. If OPG in C1 is seen, back-off L5 by moving towards M3 until OPG disappears.

### Seed

1. Ensure that both WL and pump are entering C1 properly.
2. Remove M5 if present.
3. Manually adjust D1 to optimize seed generation.
4. Make fine adjustments to M4 and DM1 to ensure that the seed travels along alignment tools all the way to the OPA wall. If large adjustments need to be made something upstream must be wrong.
5. Replace M5.
6. Replace knife edge, if absent.
  - (a) Ensure you are not clipping the red seed profile.
7. Remove L6 and L7 if present.
8. Use M5 and M6 to align the seed to the alignment guide through C2 and out of the OPA.
9. Replace L6 and L7.

### Poweramp

1. Ensure that pump is not clipping on BS1, M7.
2. Center pump on M8 using M7.

3. Remove L8 if present.
4. Using M8, M9, alignment tool ensure that pump travels along holes from M9 to M10.
5. Replace L8.
  - (a) Back of L8 Mount to front of M10 should be  $\sim 15$  cm.
6. Without clipping, place M11 and point M10 to minimize off-axis angle at M10 (this requires us to put the pump 1/4 inch right of center as viewed while facing M11).
7. Center pump on M12 using M11.
8. Center pump on DM2 using M12.
9. Overlap with seed in NC2 using DM2.
10. Make small adjustments to M10, DM2 to perfect collinearity and overlap.
11. Adjust manual D2 until over 600 mW is achieved.
12. Put "Caution fs OPA free to coldwave" sign on laser-lab doors.
13. Remove all optics downstream of Mixer 3: filter periscopes (wavelength selectors), periscope, beam splitter, and beam dump.
14. Iterate the following until optimal power and collinearity are simultaneously reached:
  - (a) Adjust collinearity of three beams using DM2
    - i. All beams should be overlapped far away.
    - ii. Use surveyor's telescope to observe beams.
  - (b) Maximize 407A-measured power using manual D2.
  - (c) Maximize 407A-measured power using M10.
15. Reassemble optics downstream of Mixer 3.
16. Close OPA lid.
17. Allow a minute for equilibration.
18. Measure and record power—should be over 600 mW.

## B.9 MicroHR Monochromator

Visible Grating.

Align the HeNe as perpendicular as possible to the monochromator entrance slit.

Move the grating angle until the HeNe falls on the exit slit.

Shine a flashlight through the entrance slit and observe the colour on the exit slit: if white, then you are at 0-order (0 nm), if red, then you are at 1st order (632.8 nm).

Go to 0-order, narrow the slits, and slowly adjust the angle until the HeNe is going through the exit slit.

Go to Jovin Yvon/utilities and find the motor configuration program.

In the Gratings tab, select the 1st grating (1200 line density) and hit Calibrate.

In theoretical wavelength, enter 0 nm.

In experimental wavelength, enter the wavelength you observe from the control program.

Hit set.



## Appendix C

# Hardware

In this chapter I collect some of the specific hardware contribution details that do not belong in the body of the dissertation.

### C.1 Adjustable periscopes

OPAs output horizontal or vertical polarizations according to which tuning process is used. Our experiments are opinionated about polarization, so some strategy for aligning polarization is necessary. In addition, it is useful to bring all excitation beams to the same height. To this end, I designed and constructed two adjustable periscopes. Each periscope is designed to bring OPA output to table height standard (5 inches) while either keeping or switching polarization. Both polarization configurations take the same path length, so source polarization can be switched without large changes to zero delay. All of this is done with just two (switched polarization) or three (kept polarization) reflections. A picture of these periscopes is shown in C.1.

While these periscopes are easy to align, their unique design means that it is not necessarily obvious what the correct strategy is. The following strategy will always converge:

1. use two “magic” apertures along the output beamline

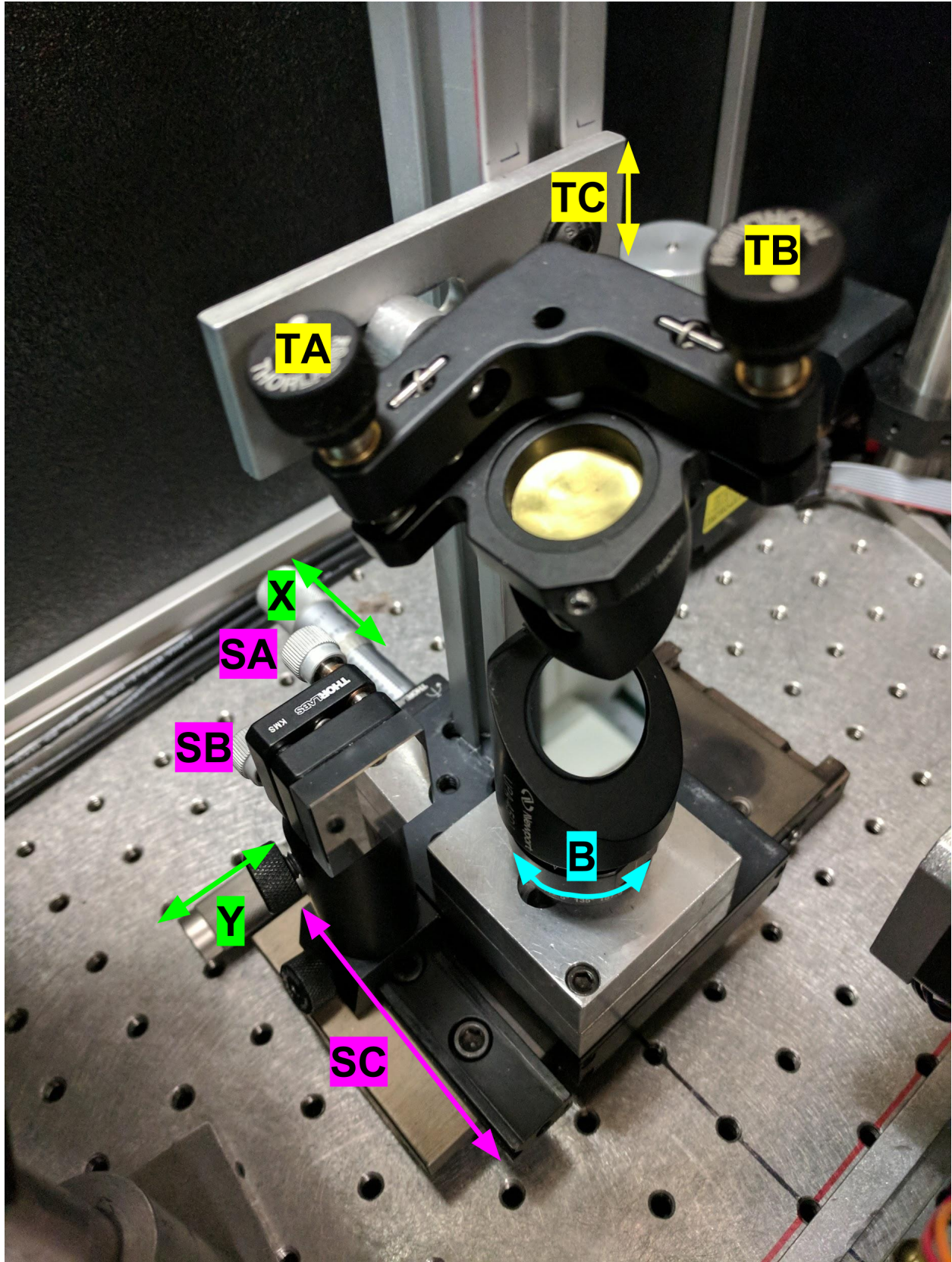


Figure C.1: CAPTION TODO

2. in flipped polarization (two mirror configuration):

- use the stage (green X, Y) to align near aperture
- use the upper mirror (yellow TA, TB) to align far aperture
- iterate above

3. in kept polarization (three mirror configuration):

- use stage X (green X) and upper mirror height (yellow TC) to align near aperture
- use lower mirror (pink SA, SB) to align far aperture
- iterate above

The kept polarization alignment is derivative of the fixed polarization alignment. One must ensure that the fixed polarization is correctly aligned at all times.

Mirror B (aqua) is magnetically mounted to switch between polarization conditions. Ensure that the lower turning mirror (pink) does not bump into mirror B (aqua) in polarization switching configuration. The lower turning mirror is on a rail (pink SC). This rail is a rough adjust for the same degree of freedom as pink SA. Adjust the rail only to ensure that the beam is roughly centered on the free aperture of the turning mirror.

The first reflection is often accomplished using a wedge, as OPA output may be strong enough to damage downstream optics. This optic can and should be replaced if more of the OPA output is desired on the table (keeping damage thresholds in mind).

### **C.1.1 Wedge polarization preference**

TODO: wedges will be more efficient at reflecting horizontal / vertical at 45 degrees

## **C.2 Automated transmissive filters**

TODO

## C.3 Electronics

TODO

## Appendix D

### Errata

In this appendix I list the errors I am currently aware of in my publications and associated work.

#### D.1 Czech 2015

The following is an errata for **CzechKyleJonathan2015a**, published in November 2015.

- Reference 13 is identical to reference 9.
- In the last paragraph of the introduction the sentence “The experimental spectra differ from the simple 2D spectrum shown in Figure 1d and those of earlier CMDS experiments with model systems” appears. This sentence cites references 6 through 10. Instead, it should cite references 15 through 20.
- In the last paragraph beginning on page 12148, the text “Automated delay stages and neutral density filters set the excitation time delays over all values of  $\tau_{21}$  with  $\tau_{22} = 0$ ” appears. For the second  $\tau$ , the subscript should read  $22'$ , not 22.
- Caption of Figure 5 reads, in part: “showing the impact of the  $\omega_1$  excitation frequency on the  $\omega_1$  spectral line shape”. This should instead read “showing the impact of the  $\omega_1$  excitation frequency on the  $\omega_2$  spectral line shape”. The subscript on the last  $\omega$  should be a 2 and not a 1.

- Figure 6  $e'+e,e'$  should read  $e'+e,e$  and vice versa.

## **Appendix E**

### **Colophon**

This chapter lays out the technical aspects of this dissertation as a software and data product, including instructions for obtaining the source and regeneration of figures and documents.







# Bibliography

- [1] Daniel Kahneman. *Thinking, Fast and Slow*. Farrar, Straus and Giroux, 2013.
- [2] Jo Erskine Hannay, Carolyn MacLeod, Janice Singer, Hans Petter Langtangen, Dietmar Pfahl, and Greg Wilson. "How do scientists develop and use scientific software?" In: *2009 ICSE Workshop on Software Engineering for Computational Science and Engineering*. Institute of Electrical and Electronics Engineers (IEEE), May 2009. DOI: [10.1109/secse.2009.5069155](https://doi.org/10.1109/secse.2009.5069155).
- [3] Judith Segal. "When Software Engineers Met Research Scientists: A Case Study". In: *Empirical Software Engineering* 10.4 (Oct. 2005), pp. 517–536. DOI: [10.1007/s10664-005-3865-y](https://doi.org/10.1007/s10664-005-3865-y).